

Molecular Physiology of the Ribbon Synapse

Dissertation

for the award of the degree

“Dr. rerum naturalium” (Dr. rer. nat.)

Division of Mathematics and Natural Sciences
of the Georg-August-Universität Göttingen

submitted by

Jakob Neef

from Göttingen

Göttingen, 2010

Members of the thesis committee:

Reviewer: Prof. Dr. Tobias Moser

InnerEarLab, Dept. of Otolaryngology, UMG

Reviewer: Prof. Dr. Martin Göpfert

Dept. of Cellular Neurobiology, Johann-Friedrich-Blumenbach-Institute
for Zoology und Anthropology

Prof. Dr. Fred Wolf

Dept. of Nonlinear Dynamics, Max-Planck-Institute for Dynamics and
Self-Organization

Date of the oral examination: June 2nd, 2010

Declaration

This thesis has been written independently and with no other sources and aids than quoted.

Jakob Neef

Göttingen, 30th of April, 2010

Contents

Introduction	1
The mammalian ear	1
The outer and middle ear.....	2
The cochlea	2
The organ of Corti.....	4
Outer hair cells.....	5
Inner hair cells	6
IHC ribbon synapses	7
Afferent innervation of the auditory system.....	8
Developmental changes in mouse IHCs	9
Voltage-gated Ca^{2+} channels (VGCC).....	10
$Ca_v\alpha_1$ subunits.....	12
$Ca_v\beta$ subunits	13
$Ca_v\alpha_2\delta$ subunits.....	13
$Ca_v\gamma$ subunits.....	14
Ca^{2+} channel inactivation	15
VGCCs in IHCs.....	16
Aim of this study	16
Materials and Methods.....	17
Animals	17
Whole-mount preparations of the organ of Corti	17
Patch clamp recordings.....	18
Data analysis.....	20
Ca^{2+} imaging.....	20
Analysis of patch-clamp and Ca^{2+} imaging data	22
Immunohistochemistry	25
Electron microscopy	27
Single IHC RT-PCR.....	27
Recording of ABRs and DPOAEs.....	28
Single unit auditory nerve fiber recordings	29
Solutions	31
Results	32
Influence of the $Ca_v\beta_2$ subunit on Ca^{2+} currents, exocytosis and development of mouse IHCs	32
$Ca_v\beta_2^{-/-}$ mice are profoundly hearing impaired and show defects in cochlear amplification.	32
$Ca_v\beta_2$ mRNA is the predominant isoform expressed in wild-type IHCs.	35
IHC Ca^{2+} currents are greatly reduced in $Ca_v\beta_2^{-/-}$ mice.....	37
The slow component of CDI is accelerated in $Ca_v\beta_2^{-/-}$ IHCs.	39
The number of Ca^{2+} channels is greatly reduced in $Ca_v\beta_2^{-/-}$ IHCs.	41
The number of ribbon synapses in $Ca_v\beta_2^{-/-}$ IHCs is unchanged.....	42
Localization of Ca^{2+} channels is normal in $Ca_v\beta_2^{-/-}$	43
Exocytosis is greatly reduced in $Ca_v\beta_2^{-/-}$ IHCs	48
Single unit recordings in $Ca_v\beta_2^{-/-}$ show residual sound encoding.....	51

IHC development is impaired in <i>Ca_vβ₂^{-/-}</i> mice.....	53
Regulation of CDI by CaBP4	59
CDI is only slightly accelerated in <i>CaBP4^{-/-}</i> mice	59
Ca ²⁺ influx and exocytosis are normal in <i>CaBP4^{-/-}</i> mice	60
Auditory systems function is not impaired in <i>CaBP4^{-/-}</i> mice.....	61
Discussion	63
Regulation of IHC Ca ²⁺ channels by Ca _v β subunits	63
Ca _v β subunits present in IHCs.....	61
Deafness phenotype of <i>Ca_vβ₂^{-/-}</i> mice.....	64
Role of Ca _v β ₂ at the IHC synapse	65
Synaptic transmission from <i>Ca_vβ₂^{-/-}</i> IHCs	68
Auditory neuron activity in <i>Ca_vβ₂^{-/-}</i>	68
Developmental defects in <i>Ca_vβ₂^{-/-}</i> IHCs.....	69
CaBPs in mouse IHCs.....	71
Conclusions.....	71
References	73
Abbreviations.....	86
Acknowledgements.....	88
Curriculum Vitae.....	90

Introduction

Sound is not only the carrier for the primary means of communication in humans but also critical for the survival of many kinds of animals, which use it not only for communication but also to locate prey, evade predators or even for navigation.

Sound consists of pressure waves which transmit oscillations through a gas, liquid, or solid medium. It carries two kinds of information: that about pitch (frequency) and that about intensity (pressure level). Many animals possess a pair of hearing organs, allowing them to detect another attribute of a sound stimulus: the direction from which it is originating. A very important feature for sound localization is thought to be the interaural time difference, the difference in arrival time of the sound stimulus between the two hearing organs. The speed of airborne sound is about 340 m/s. Therefore, depending on the distance between the hearing organs and the angle of propagation of the wave with respect to the interaural axis, time differences of a few μs need to be detected. Thus, given a constant distance between the hearing organs, the precise interaural time difference provides information to the animal about the location of the sound source. This requires an astonishing fidelity in the transmission of sound-evoked neural signaling in the nervous systems, the fundamentals of which are so far not completely understood.

The mammalian ear

Tympanic eardrums have evolved several times independently in the ancestors of modern amphibians, turtles, lepidosaurs (lizards and snakes), archosaurs (birds and crocodiles), and mammals.

In order for sound to be perceived, the changes in air pressure need to be picked up by the outer ear and transmitted to the inner ear, where they are then translated into electrical signals which are relayed to the central nervous system (for review, see Dallos et al., 1996).

The outer and middle ear

The outer ear consists of the auricle, which focuses and filters the incoming sound, and the ear canal. At the end of the ear canal, the incoming pressure waves transmit vibrations onto the tympanic membrane which conveys the sound into the middle ear. In this air-filled cavity, the auditory information is carried onwards by the three ossicles - malleus, incus, and stapes, also known as hammer, anvil, and stirrup – to the oval window of the inner ear. The function of this arrangement is to amplify the mechanical stimulus (both by the larger surface of tympanic membrane as compared to the oval window membrane and by the leverage effects of the ossicles) in order to overcome the higher impedance of the incompressible aqueous solutions in the inner ear, to which the stimulus is transferred.

The inner ear consists of two parts: the cochlea and the vestibular system.

The cochlea

The cochlea (from the Latin word for snail) is a bony structure resembling a snail's shell. It consists of a bony core around which several turns of fluid-filled compartments are coiled up. The number of turns depends on the species – in humans one can find 2.5 turns, in mice 1.75, and in guinea-pigs 4. There are three fluid-filled compartments wound up along the cochlea: the scala vestibuli, scala tympani, and scala media (Fig. 1). These compartments are filled with lymphatic solutions of different ionic compositions. The scala vestibuli and scala tympani are filled with perilymph, which contains a comparably low amount of K^+ (~5 mM). The endolymph found in the scala media has a much higher concentration of K^+ (~160 mM) due to secretion of K^+ from the stria vascularis, the outside boundary of the scala media.

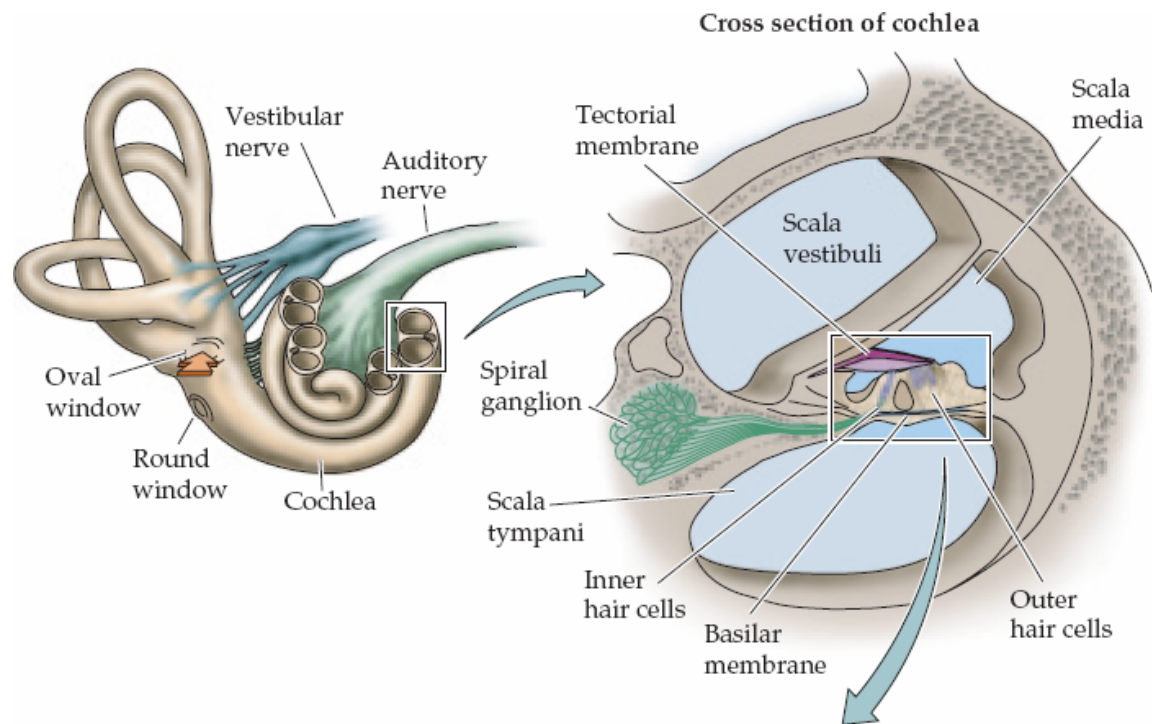


Figure 1: Cross section of the cochlea. Sound is transferred onto the fluid-filled cochlea via the oval window. The cochlea is partitioned into three compartments: the scala vestibuli, scala media, and scala tympani.

Image taken from Purves et al., 2004.

When movement of the stirrup transfers the mechanical energy of incoming sound onto the oval window, pressure is exerted onto the solution in the lower of the three compartments, the scala tympani. Since this fluid is virtually incompressible, the increase in pressure along the coiled structure leads to a displacement of solution towards the more elastic of the boundaries of the scala tympani, the basilar membrane separating it from the middle compartment, the scala media. This pressure is then passed on via Reissner's membrane onto the fluid contained in the upper compartment, the scala vestibuli, where it results in an outward bulging of the round window membrane. Through this system of pressure transfers, each pressure wave entering the cochlea via the oval window results in vertical movement of the basilar membrane and the organ of Corti situated on top of it, creating a travelling wave along the length of the cochlear turns (Fig. 2). However, since the physical properties of the basilar membrane change from base to apex of the cochlea (it gets thinner, broader and less stiff towards the apex of the

cochlea), the amount of displacement of the membrane by vibrations of different frequencies varies according to its position along the length of the organ of Corti. In this way, high frequencies result in maximal movement of the basilar membrane in the basal parts of the cochlea, while low frequencies cause strong movement in the apical parts. This results in a rough tonotopic mapping of different frequencies along the length of the organ of Corti, covering the entire hearing range of the organism. This range can be quite different between species, from 1 to 100 kHz in the mouse and from 20 Hz to 20 kHz in humans.

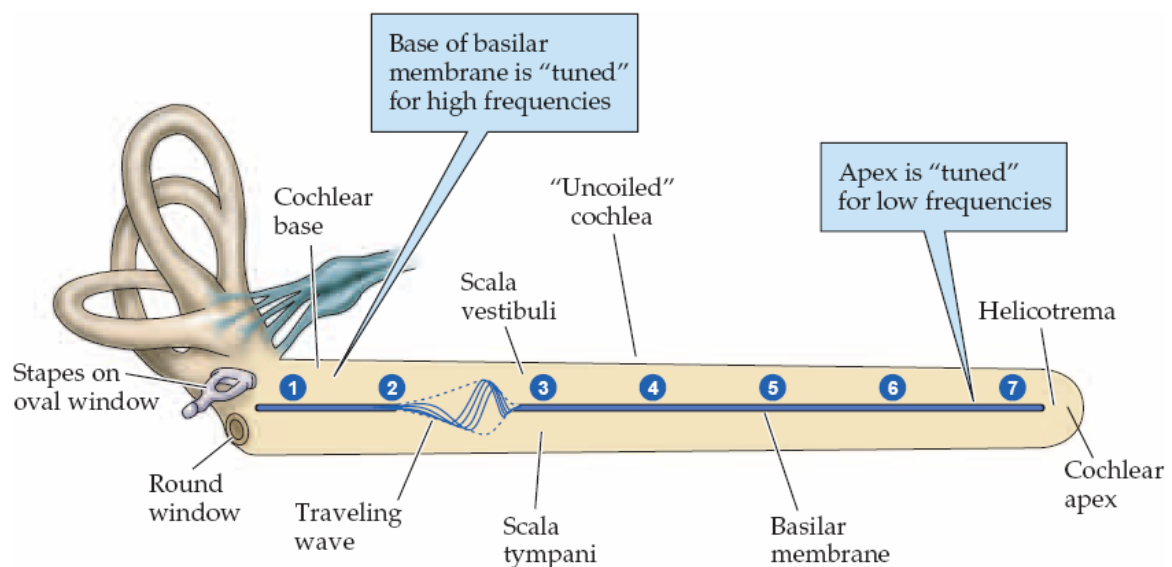


Figure 2: The traveling wave in the cochlea. The schematic shows the organ of Corti (uncoiled for clarity) with a travelling wave. The basilar membrane shows maximal displacement in positions that are dependent on the frequency of the sound, with higher frequencies leading to strong movement in the basal regions and low frequencies reaching peak displacement in the apical regions.

Image taken from Purves et al., 2004.

The organ of Corti

The organ of Corti is a highly organized structure responsible for the encoding of acoustic information into electric signals. Situated on top of the basilar membrane, it consists of one row of inner hair cells (IHCs), three rows of outer hair cells (OHCs) and several types of supporting cells such as Hensen's cells, Deiter's cells, phalangeal cells, and inner and outer pillar cells (see

Fig. 3). While the supporting cells play important roles in homeostasis and structural support of the organ of Corti, the hair cells are responsible for the transduction and amplification or transformation of sound.

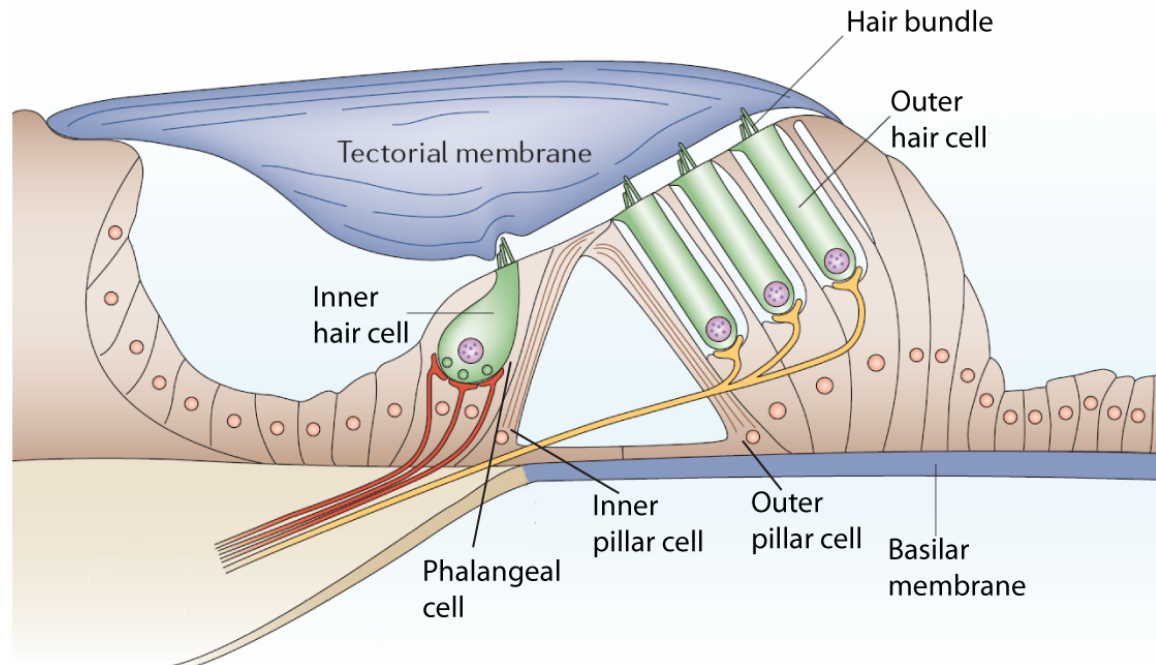


Figure 3: Cell types in the organ of Corti. On the outside of the organ of Corti lie three rows of OHCs, which contract and expand in response to sound stimuli, thus actively amplifying the mechanical energy from incoming sounds. Further inwards the tunnel of Corti can be found, a fluid-filled space flanked by the outer and inner pillar cells. Still further inside, surrounded by phalangeal cells, are the IHCs. Sound-evoked movement of the tectorial membrane results in displacement of their stereocilia, ultimately leading to secretion of neurotransmitter onto the boutons of afferent neurons contacting the IHCs at their basolateral surface.

Image modified from Fettiplace and Hackney, 2006.

Outer hair cells

OHCs act as active amplifiers by enhancing sound-evoked movement of the tectorial membrane (for review, see Ashmore, 2008; Dallos and Fakler, 2002). Similar to IHCs, OHCs possess so-called hair bundles, groups of stereocilia, which are anchored in the tectorial membrane. Vertical displacement of the

organ of Corti leads to a shearing movement, causing deflection of the stereocilia which in turn causes opening or closing of mechanosensitive channels. The increase or decrease of cation influx through these channels depolarizes or hyperpolarizes the cell, respectively. The lateral membrane of the cylindrical OHCs is densely packed with prestin, an integral membrane protein which belongs to the SLC26 family of ion transporters (Lohi et al., 2000). It undergoes voltage-dependent conformational changes, resulting in stretching or shrinking of the cell, which are conferred by interaction with Cl⁻ and bicarbonate anions in the cytoplasm (Oliver et al., 2001).

This prestin-driven electromotility has been shown to underlie the function of outer hair cells as cochlear amplifiers (Liberman et al., 2002; Zheng et al., 2000). In addition to this, there has also been some evidence that active hair-bundle motility contributes to the amplification process (Chan and Hudspeth, 2005; Kennedy et al., 2005; and for review, see Hudspeth, 2008).

Inner hair cells

The pear-shaped IHCs are the true auditory sensory cells. Their most striking gross anatomical feature are the hair bundles, groups of stereocilia arranged in two to three rows on their apical surface (for review, see Raphael and Altschuler, 2003). These stereocilia are membrane-bound cellular projections with a diameter of ~250 nm and a dense actin-filament core. Each IHC possesses 20-50 stereocilia (or more), depending on species and location along the basilar membrane (with more stereocilia in the basal part). The apical tips of stereocilia are connected to the neighboring cilia with so-called tip links (Pickles et al., 1984), filamentous structures composed mainly of cadherin 23 (Siemens et al., 2004; Sollner et al., 2004) and protocadherin 15 (for review, see Müller, 2008). These tip links are thought to be directly linked to the mechano-electrical transducer (MET) channels (Howard and Hudspeth, 1988; Assad et al., 1991) situated at the top of the stereocilia (Jaramillo and Hudspeth, 1991; Lumpkin and Hudspeth, 1995; Beurg et al., 2009). When vertical displacement of the basilar membrane causes movement of the tectorial membrane relative to the organ of Corti, the hair bundles of the

OHCs are deflected, while the resulting movement of fluid displaces the hair bundles of the IHCs. A displacement in the direction of the longest stereocilia causes increased tension in the tip links which in turn opens the MET channels, allowing influx of cations, mainly K^+ (Corey and Hudspeth, 1979), from the endolymph into the cells. This leads to a rapid depolarization of the IHC membrane. Displacement in the opposite direction causes a slackening of the tip links, resulting in closing of MET channels and a more negative membrane potential.

Depolarization of IHCs activates voltage-gated Ca^{2+} channels (VGCCs) at the cell's ribbon synapses, ultimately leading to exocytosis of glutamate into the synaptic cleft.

IHC ribbon synapses

The hallmark feature to which ribbon synapses owe their name is the synaptic ribbon, an electron dense structure of submicrometer size which can be found at the active zones of synapses of auditory and vestibular hair cells as well as photoreceptors, retinal bipolar cells, and pinealocytes (for review, see (Lenzi and Gersdorff, 2001; Fuchs et al., 2003; Sterling and Matthews, 2005). In auditory hair cells, ribbons are more round to ellipsoid structures with a diameter of 100-500 nm (for review, see Nouvian et al., 2006). A large number of synaptic vesicles are tethered to the ribbon structure by molecules of unknown identity, forming a halo around the ribbon body. The main constituent of the ribbon body is RIBEYE (Schmitz et al., 2000), a protein unique to ribbon synapses. Interestingly, one of its two domains is identical to the C-terminal binding protein 2 (CtBP2), a transcription factor ubiquitously found in most tissues. Large agglomerates of RIBEYE make up most of the ribbon, but some other components are also known (for review, see Zanazzi and Matthews, 2009). The scaffolding protein Bassoon anchors the ribbon at the active zone (Dick et al., 2003; Khimich et al., 2005). Piccolo is also present (Dick et al., 2001; Khimich et al., 2005).

While the peculiar structure of the ribbon synapse is relatively well known and some molecular components of the ribbon have been discovered, its

physiological role is less well understood. A characteristic feature of ribbon synapses is that they occur in cells where exocytosis is evoked by graded potentials and which can support high rates of sustained release. In accordance with this role, the ribbon has been suggested to work as a kind of “conveyor belt”, moving vesicles towards the active zone in an orderly fashion in response to depolarization (Bunt, 1971). Other theories suggest that the ribbon works rather as a “safety belt”, keeping vesicles in close contact to facilitate multivesicular release through compound fusion (Parsons and Sterling, 2003), as a means of stabilizing a large readily releasable pool (RRP) of vesicles at the synapse (Moser et al., 2006b; Khimich et al., 2005) or, in direct contradiction to the “conveyor belt” theory, that it might actually restrict vesicle access to the membrane, preventing depletion of the vesicle pool by strong stimuli (Jackman et al., 2009).

Afferent innervation of the auditory system

In mature IHCs, each ribbon synapse is contacted by one individual type I spiral ganglion neuron (SGN). When depolarization of the IHC leads to exocytosis, glutamate is released into the synaptic cleft between the IHC and the bouton of the postsynaptic SGN. Activation of glutamate receptors on the afferent bouton results in excitatory postsynaptic currents. When a large enough number of receptors has been activated, the resulting currents depolarize the cell, thus triggering action potentials in the SGN which are relayed via the auditory nerve to the cochlear nuclei. From here, the signal travels onwards to the contralateral superior olive, further on to the inferior colliculus, the medial geniculate body of the thalamus, and finally to the auditory cortex.

Developmental changes in mouse IHCs

Mice are born deaf and do not acquire hearing until around postnatal day 12 (p12; (Mikaelian and Ruben, 1965). In the period between birth and the onset of hearing, the electrical and morphological properties of the IHCs undergo fundamental changes.

In newborn mice, spontaneous release of ATP from supporting cells causes nearby IHCs to depolarize and fire bursts of Ca^{2+} -mediated action potentials (Tritsch et al., 2007), which result in release of glutamate from the IHC (Beutner and Moser, 2001; Glowatzki and Fuchs, 2002). This synchronized activation of groups of neighboring IHCs is thought to help formation of tonotopic maps in the brain and ceases after the age of p10.

Around this same time, IHCs begin to express large conductance voltage and Ca^{2+} activated K^+ channels (BK channels). In non-mammalian auditory hair cells BK channels are activated in response to Ca^{2+} influx, creating membrane potential resonances with kinetics which contribute to tuning of the cells to specific frequencies (for review, see Fettiplace and Fuchs, 1999). Their role in mammalian IHCs, however, is less well understood. Mammalian hair cells do not display electrical resonance, and lack of BK channels does not appear to affect frequency tuning in auditory neurons (Oliver et al., 2006). However, voltage responses of $BK^{-/}$ IHCs are delayed but increased in amplitude, and auditory neurons show deteriorated precision of spike timing.

The characteristics of the presynaptic ribbon also change during maturation: ribbons in immature IHCs are round, almost spherical in shape, and multiple ribbons may be anchored at a single active zone; however, ribbons in mature IHCs are more elongated and each active zone holds only one ribbon.

Neonatal IHCs are directly targeted by inhibitory cholinergic efferent neurons from the medial part of the superior olivary complex (Simmons et al., 1996), which activate $\alpha 9$ - $\alpha 10$ acetylcholine receptors (Glowatzki and Fuchs, 2000; Plazas et al., 2005). Ca^{2+} influx through these receptors in turn opens slowly activating small-conductance potassium channels of the SK2 type (Oliver et al., 2000), leading to a hyperpolarization of the cell which can suppress the occurrence of spontaneous Ca^{2+} action potentials. During maturation of the hair cell, the efferent nerve terminals move away from the IHC body and

project towards the first row of OHCs, where they form direct connections with the OHC. At the same time, efferent fibers from the lateral superior olivary complex project their axons towards the row of IHCs, where they form axodendritic contacts with the afferent fibers just below the IHCs (for review, see Simmons, 2002).

Voltage-gated Ca²⁺ channels (VGCC)

In the 1980s, the first Ca²⁺ channel protein was purified and shown to be a complex of several subunits (Borsotto et al., 1985; Flockerzi et al., 1986; Takahashi et al., 1987). The pore-forming subunit of VGCCs was named Ca_vα₁, auxiliary subunits were named Ca_vβ, Ca_vα₂, Ca_vδ, and Ca_vγ. So far, ten different genes for Ca_vα₁, four for Ca_vβ, eight for Ca_vγ subunits, and four for the disulfide-linked Ca_vα₂δ complex were identified (for review, see Hofmann et al., 1999).

VGCCs are classified into five different types depending on their current properties and sensitivity to certain drugs (for review, see Tsien et al., 1995): L-type Ca²⁺ channels exhibit long-lasting, large currents. They are high-voltage activated (HVA) and can be blocked by dihydropyridines, phenylalkylamines and benzothiazepines. N-, and P/Q-type channels also activate at high voltages but have a lower conductance than L-type and can be blocked by specific polypeptide poisons derived from snails or spiders: N-type channels are sensitive to ω-conotoxin GVIA (Nowycky et al., 1985) and P/Q-type are sensitive to ω-Aga IVA toxin (Llinás et al., 1989). R-type channels also activate at high voltages (Niidome et al., 1992) but are resistant to toxins (Williams et al., 1994), and T-type channels are a class of low-voltage activated (LVA) channels exhibiting only small and quickly inactivating currents (Carbone and Lux, 1984; Nilius et al., 1985).

Channel name	Type	α unit	Localization	Cellular Functions
Ca _v 1.1	L	α_{1S}	Skeletal muscle; transverse tubules	Excitation-contraction coupling
Ca _v 1.2	L	α_{1C}	Cardiac myocytes; smooth muscle myocytes; endocrine cells; neuronal cell bodies; proximal dendrites	Excitation-contraction coupling; hormone release; regulation of transcription; synaptic integration
Ca _v 1.3	L	α_{1D}	Endocrine cells; neuronal cell bodies and dendrites; cardiac atrial myocytes and pacemaker cells; cochlear hair cells	Hormone release; regulation of transcription; synaptic regulation; cardiac pacemaking; hearing; neurotransmitter release from sensory cells
Ca _v 1.4	L	α_{1F}	Retinal rod and bipolar cells; spinal cord; adrenal gland; mast cells	Neurotransmitter release from photoreceptors
Ca _v 2.1	P/Q	α_{1A}	Nerve terminals and dendrites; neuroendocrine cells	Neurotransmitter release; dendritic Ca ²⁺ transients; hormone release
Ca _v 2.2	N	α_{1B}	Nerve terminals and dendrites; neuroendocrine cells	Neurotransmitter release; dendritic Ca ²⁺ transients; hormone release
Ca _v 2.3	R	α_{1E}	Neuronal cell bodies and dendrites	Repetitive firing; dendritic calcium transients
Ca _v 3.1	T	α_{1G}	Neuronal cell bodies and dendrites; cardiac and smooth muscle myocytes	Pacemaking; repetitive firing
Ca _v 3.2	T	α_{1H}	Neuronal cell bodies and dendrites; cardiac and smooth muscle myocytes	Pacemaking; repetitive firing
Ca _v 3.3	T	α_{1I}	Neuronal cell bodies and dendrites	Pacemaking; repetitive firing

Table 1: Different types of VGCCs.

Modified from Catterall et al., 2005.

These channels can be further classified according to their α_1 subunit. A newer nomenclature has been suggested by Ertel et al., 2000, which groups the channels by gene families and Ca_v α_1 subunit (see table 1). This nomenclature will be used throughout this manuscript.

The pharmacological and electrophysiological diversity of different Ca²⁺ channels arises primarily from different types of Ca_v α_1 subunits, but the channels are modulated by the auxiliary Ca_v β , Ca_v γ , and Ca_v $\alpha_2\delta$ subunits.

Ca_vα₁ subunits

Initially discovered in skeletal muscle (Tanabe et al., 1987), the pore-forming Ca_vα₁ subunits are large multidomain proteins from the same multigene family as voltage-gated potassium and sodium channels. Each of their four homologous domains contains six transmembrane segments and a pore region between segments S5 and S6. The S4 segment contains several positively charged residues and is thought to act as the voltage sensor of the channel, similar to what has been shown for the S4 subunit of voltage-gated potassium channels (Logothetis et al., 1992; Glauner et al., 1999). Furthermore, interaction sites with the other subunits as well as with other molecules can be found on the Ca_vα₁ subunit.

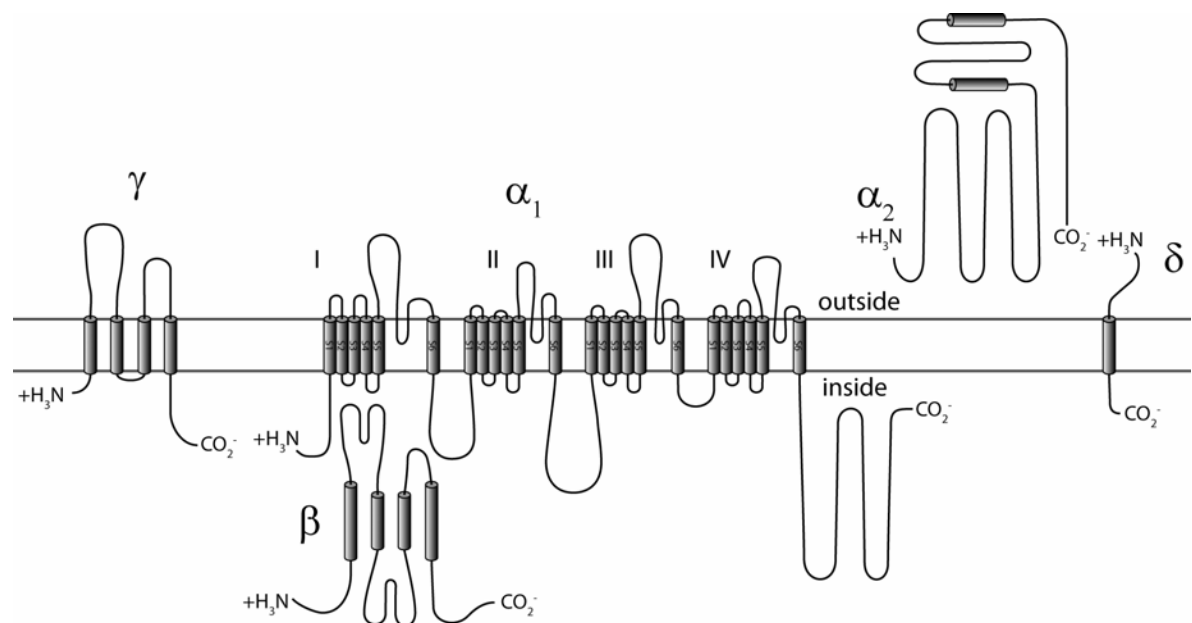


Figure 4: Subunit composition and structure of VGCCs. The Ca_vα₁ subunit is the pore-forming component of VGCCs, which also contains the voltage sensor. The Ca_vα₁ subunit is composed of four domains, each of which contains six transmembrane segments. The voltage sensor is thought to be located in segment S4. The Ca_vβ subunit binds to the Ca_vα₁ subunit via the α-interaction domain. Ca_vα₂δ is composed of two parts, the membrane-bound Ca_vδ and the extracellular Ca_vα₂.

Modified from Catterall et al., 2005.

Ca_vβ subunits

Ca_vβ subunits are entirely intracellular proteins coexpressed with all VGCCs. They bind to the intracellular loop between domains I and II of the Ca_vα₁ subunit (Pragnell et al., 1994), where the α-interaction domain (AID) of Ca_vα₁ contacts Ca_vβ's α-binding pocket (Van Petegem et al., 2004; Van Petegem et al., 2008). LVA channels of the Ca_v3 family do not appear to be modulated by β subunits (Lambert et al., 1997; Leuranguer et al., 1998; Wyatt et al., 1998) and the sequence of their AID is only poorly conserved (Arias et al., 2005).

Diverse modulatory effects have been attributed to Ca_vβ subunits: enhancement of expression of the Ca_vα₁ subunit at the plasma membrane (probably by masking an endoplasmic reticulum retention signal at the AID; Bichet et al., 2000); increased open probability (Neely et al., 1993); hyperpolarization of the voltage-dependence of activation (Jones et al., 1998); changes of voltage-dependent inactivation (VDI; Meir and Dolphin, 2002); and an antagonizing effect on regulation of the Ca²⁺ channel by G-proteins (Cantí et al., 2000).

Furthermore, Ca_vβ subunits belong to the family of membrane-associated guanylate kinase proteins (MAGUK; Hanlon et al., 1999), which organize intracellular signaling pathways with multiple protein-protein interaction domains. Two such domains can be found in Ca_vβ: the guanylate kinase domain (GK, which binds the AID of Ca_vα), and the Src homology 3 (SH3) domain. These domains are conserved across all Cavβ isoforms. Also, interactions with proteins such as the small G-protein kir/Gem (Beguin et al., 2001) or the endocytic protein dynamin (Gonzalez-Gutierrez et al., 2007) have been shown.

Ca_vα₂δ subunits

The Ca_vα₂δ subunit consists of two parts, Ca_vα₂ and Ca_vδ. Both are translated from the same mRNA and the resulting protein is post-translationally cleaved. The Ca_vδ subunit is anchored in the plasma

membrane with a single transmembrane segment and is tied to the extracellular $\text{Ca}_V\alpha_2$ subunit by a disulfide bond.

After first being discovered in association with the $\text{Ca}_V\alpha_S$ subunit (Takahashi et al., 1987), the $\text{Ca}_V\alpha_2\delta$ was later shown in combination with other $\text{Ca}_V\alpha$ subunits such as $\text{Ca}_V\alpha_{1B}$ (Witcher et al., 1993), $\text{Ca}_V\alpha_{1A}$ (Liu et al., 1996) and $\text{Ca}_V\alpha_{1C}$ (Liu et al., 1996). It is not known, however, whether all HVA channels are expressed in combination with a $\text{Ca}_V\alpha_2\delta$.

Coexpression of $\text{Ca}_V\alpha_2\delta$ with several $\text{Ca}_V\alpha$ subunits resulted in an increase in measured Ca^{2+} currents as well as faster inactivation kinetics and a shift of the voltage-dependence of activation to more negative potentials (Felix et al., 1997). The increase in Ca^{2+} current is thought to be mediated by an increase in the number of functional channels, since single-channel conductance does not appear to be affected by $\text{Ca}_V\alpha_2\delta$ (Barclay et al., 2001). Therefore, similar to $\text{Ca}_V\beta$, $\text{Ca}_V\alpha_2\delta$ seems to enhance trafficking of $\text{Ca}_V\alpha$ to the plasma membrane (Cantí et al., 2005).

$\text{Ca}_V\gamma$ subunits

Along with the other subunits, the small $\text{Ca}_V\gamma_1$ subunit was initially discovered in skeletal muscle (Sharp and Campbell, 1989; Jay et al., 1990). In the following years, seven more $\text{Ca}_V\gamma$ types were discovered (for review, see Black, 2003). These proteins are thought to possess four transmembrane domains (Jay et al., 1990; Green et al., 2001) but their function has not yet been as thoroughly researched as that of $\text{Ca}_V\beta$ and $\text{Ca}_V\alpha_2\delta$. According to experimental data and bioinformatic analyses they can be clustered into three groups: $\text{Ca}_V\gamma_{1, 6}$, $\text{Ca}_V\gamma_{5, 7}$, and $\text{Ca}_V\gamma_{2, 3, 4, 8}$. $\text{Ca}_V\gamma_1$ and 6 have been shown to regulate Ca^{2+} channel activity by suppressing whole-cell Ca^{2+} currents and speeding up inactivation of the channel while leaving the single-channel conductance unchanged (Freise et al., 2000; Ahern et al., 2001; Hansen et al., 2004). In contrast, $\text{Ca}_V\gamma_{2, 3, 4, 8}$ play a role in the regulation of AMPA receptor trafficking, while leaving Ca^{2+} currents essentially unchanged (for

review, see Osten and Stern-Bach, 2006). The roles of $\text{Ca}_V\gamma_5$ and γ_7 are not known so far.

Ca^{2+} channel inactivation

Calcium channels show two types of inactivation: voltage-dependent inactivation (VDI) and Ca^{2+} -dependent inactivation (CDI; Brehm and Eckert, 1978). The two types of inactivation can be distinguished by substituting Ba^{2+} for Ca^{2+} as a charge carrier. The inactivation of Ba^{2+} current (I_{Ba}) is generally regarded as VDI, while the additional inactivation observed in the Ca^{2+} current (I_{Ca}) is correspondingly called CDI. However, it should be noted that, at least in L-type channels, inactivation of Ba^{2+} currents still has a minor Ba^{2+} -dependent component (Ferreira et al., 1997).

CDI is caused by Ca^{2+} -bound calmodulin (CaM) binding to the IQ-motif of the $\text{Ca}_V\alpha_1$ subunit (Peterson et al., 1999; Qin et al., 1999; Zühlke et al., 1999). CaM preassociates with L-, P/Q-, and R-type Ca^{2+} channels even in the absence of Ca^{2+} (Erickson et al., 2001; Pitt et al., 2001) and has two distinct Ca^{2+} binding regions at the N-terminal and C-terminal lobe (DeMaria et al., 2001; Yang et al., 2006). Interestingly, the two lobes react differently to distinct Ca^{2+} signals – the C-terminal lobe senses local, high Ca^{2+} concentrations arising in the Ca^{2+} microdomain at the mouth of the channel (Liang et al., 2003) and the N-terminal lobe senses global increases in Ca^{2+} concentration (Cens et al., 2006).

CDI can be regulated in a variety of ways. The diverse types of $\text{Ca}_V\alpha_1$ subunits differ in the degree of CDI observed in their currents. Additionally, it can also be influenced by alternative splicing of the $\text{Ca}_V\alpha_1$ subunit (Shen et al., 2006) or by the type of $\text{Ca}_V\beta$ subunit coexpressed with the channel (Lee et al., 2000; Cui et al., 2007). Another mechanism for the modulation of CDI is the expression of Ca^{2+} binding proteins (CaBPs), a family of proteins closely related to Calmodulin. They can displace Calmodulin from the IQ-motif of the $\text{Ca}_V\alpha_1$ subunit, thereby slightly modifying the channels properties and preventing CDI (Lee et al., 2002; Zhou et al., 2004; Haeseleer et al., 2004).

VGCCs in IHCs

At conventional synapses exocytosis is primarily caused by Ca^{2+} influx through P/Q-, N-, and/or R-type channels; however the Ca^{2+} -channel found in IHCs is predominantly the L-type $\text{Ca}_v1.3$ isoform (Platzner et al., 2000; Brandt et al., 2003; Dou et al., 2004). The features typical of L-type channels (sensitivity to 1,4-Dihydropyridines, a class of drugs which can have either inhibitory (Isradipine, Nifedipine) or augmenting effects (BayK8644) on the channel) can therefore also be observed in IHC Ca^{2+} -currents. However, the strong CDI of $\text{Ca}_v1.3$ Ca^{2+} currents observed in the sinoatrium and pancreas, or when expressing the channel in heterologous expression systems is not observed in mature IHCs.

In IHCs, as in other ribbon-containing cells, $\text{Ca}_v1.3$ channels assemble in clusters at the ribbon synapse (Roberts et al., 1990; Zenisek et al., 2003; Brandt et al., 2005), with only a low number of extrasynaptic channels (Brandt et al., 2005).

The molecular link responsible for anchoring the channel at the active zone is unknown. A promising candidate is the rab3-interacting molecule (RIM), which has been shown to interact with both the synaptic vesicle protein rab3 (Wang et al., 1997), as well as with $\text{Ca}_v\beta$ subunits (Kiyonaka et al., 2007). In this case, RIM might keep synaptic vesicles and Ca^{2+} channels very close to each other. This is especially interesting, since in IHCs, Ca^{2+} -evoked exocytosis is under control of a “nanodomain” regime (Brandt et al., 2005), where exocytosis of an individual vesicle is triggered by Ca^{2+} influx through one or few channels located in very close proximity of the synaptic vesicle.

Aim of this study

The aim of this study was to gain a deeper insight into the molecular regulation of Ca^{2+} channels at the IHC ribbon synapse. We have focused on the potential regulation of CDI by CaBP4 by examining a *CaBP4* knockout mouse and on the role of the $\text{Ca}_v\beta_2$ VGCC subunit on Ca^{2+} currents and cochlear development by examining a *Ca_v\beta_2* knockout mouse.

Materials and Methods

Animals

CaBP4^{-/-} mice were generated by Haeseleer et al. (Haeseleer et al., 2004) by replacing exon 1 and part of exon 2 of the *CaBP4* gene with a neo-cassette. *Ca_vβ₂*^{-/-} mice were generated by Ball et al. (Ball et al., 2002) by replacing exons 4 through 13 of the *Ca_vβ₂* gene with a neo-cassette. To counter embryonic lethality of the knockout, they created a transgenic mouse line expressing rat *Ca_vβ₂* under control of a cardiac specific promoter, the α -myosin heavy chain, hereafter referred to as *Ca_vβ₂*^{-/+}. C57BL/6 mice were used for controls. Mice were used between postnatal day 16 (p16) and p21 for single-cell reverse transcription polymerase chain reaction (RT-PCR) and p21 to p28 for hair cell physiology, immunohistochemistry, auditory evoked brainstem responses (ABRs) and distortion product otoacoustic emissions (DPOAEs). Single unit recordings were acquired from mice aged p40 to p70. Both mouse lines were kept in homozygous breeding. All experiments complied with national animal care guidelines and were approved by the University of Göttingen Board for Animal Welfare and the Animal Welfare Office of the State of Lower Saxony.

Whole-mount preparations of the organ of Corti

Mice were anesthetized with CO₂ and killed by decapitation. After removing the skin, the skull was sagittally cut in half and transferred into a Petri dish containing ice-cold HEPES-buffered Hanks' balanced salt solution (HEPES-HBSS, see *Solutions* below for formulae). The brain was removed and the cochlea together with the rest of the bony labyrinth was gently twisted out of the skull with a pair of fine forceps. After carefully opening up the bony walls of the cochlea, the apical turn of the organ of Corti was removed from the modiolus and transferred to the next step with a fire-polished Pasteur's pipette.

Patch clamp recordings

After isolating the organ of Corti as described above, the whole-mount preparation was transferred to a recording chamber where it was fixed at the bottom of the chamber with a grid of nylon threads, with the basilar membrane down and the tectorial membrane up. During recordings, it was constantly perfused with modified Ringer's solution at a rate of at least 1 ml/min. To allow access to the IHCs, the tectorial membrane was removed with a cleaning pipette with a large opening (\varnothing of $\sim 20\text{-}40\ \mu\text{m}$). To obtain a clean, patchable membrane at the inner hair cell, the surrounding cells needed to be cleaned off beforehand. The outer hair cells were removed with a cleaning pipette (opening \varnothing of $\sim 3\text{-}5\ \mu\text{m}$), followed by the outer and inner pillar cells. Before patching IHCs, individual phalangeal cells were carefully removed with patch pipettes.

Pipettes were pulled from GB150-8P borosilicate glass capillaries (Science Products, Hofheim, Germany) with a Sutter P-2000 laser pipette puller (Sutter Instrument Company, Novato, USA) with the program shown in table 2. Using a custom-made microforge, they were subsequently coated with Sylgard (Dow Corning, Wiesbaden, Germany), a hydrophobic silicone compound, to lower the pipette's capacitance. After fire-polishing the tip to enhance sealing with the IHC plasma membrane, pipettes showed a resistance of 3.5 to 4.5 M Ω when filled with Cs-based intracellular solution (see *Solutions*).

Line	Heat	Filament	Velocity	Delay	Pull
1	450	4	30	150	20
2	420	4	35	200	
3	410	4	42	200	
4	390	4	62	180	15
5	385	4	67	180	30

Table 2: Puller program for patch pipettes.

The patch-clamp setups were shielded by Faraday cages and assembled on hydraulic air tables for vibration isolation (TMC, Peabody, USA). Experiments were conducted with Olympus BX50WI microscopes (Olympus, Hamburg, Germany) equipped with Olympus 60x water immersion objectives (0.9 NA). Ringer bath level and pipette pressure were controlled by MPCU-3 pumps (Lorenz Messgeätebau, Kathlenburg-Lindau, Germany). The preparations were visualized by video camera (KamPro02IR, EHD imaging, Damme, Germany or SensiCam, PCO, Kelheim, Germany). Patch pipettes were approached towards the preparation with a piezoelectric micromanipulator (Tritor, piezosystem jena, Jena, Germany) or step motor micromanipulator (SM-5, Luigs & Neumann, Ratingen, Germany). Patch-clamp recordings were performed with EPC-9 amplifiers (HEKA, Lambrecht/Pfalz, Germany) controlled by Pulse software (HEKA).

Ca²⁺ hotspots were recorded at an upright confocal microscope (Olympus Fluoview 300 confocal scanner with a R3896 photomultiplier tube by Hamamatsu (Herrsching am Ammersee, Germany) as detector mounted to an Olympus BX50WI microscope) at 60x magnification (0.9 NA, 60x water immersion objective, Olympus). As light sources, a 50 mW, 488 nm solid state laser (Cyan, Newport Spectra-Physics, Santa Clara, USA) and a 1.5 mW, 543 nm He-Ne laser (LGK 7786 P150, Lasos, Jena, Germany) were used. Acquisition was performed in Olympus Fluoview software under control of the programmable acquisition protocol processor.

Patch-clamp recordings were carried out essentially as described by Sakmann and Neher, 2009. Briefly, recording pipettes were filled with intracellular solution and advanced towards the IHC under constant positive pressure of ~2.5 cm H₂O to prevent contamination of the pipette with dirt from the extracellular solution. After making contact with the IHC, a gigaseal was formed by application of slightly negative pressure to the patch pipette. Artifacts caused by charging of the capacitance of the pipette and the headstage were subtracted using Pulse's built-in C_{fast} cancellation function. Electrical access to the cell's interior was gained by one of two possible ways. When requiring introduction of a certain agent into the cell ("hotspot" recordings or recordings with 5 mM EGTA in the intracellular solution) or low series resistance (R_S; fluctuation analysis or recordings of K⁺ currents), the

cell membrane was ruptured by a series of short, negative pressure pulses to achieve the whole-cell configuration. In all other cases, the cell membrane was perforated by introduction of amphotericin B (an antibiotic forming membrane pores permeable to monovalent ions) into the intracellular solution to achieve the perforated-patch configuration. Here the patch pipettes were dipped into amphotericin-free solution for ~1 minute in order to keep the solution in the tip of the pipette free of amphotericin to prevent contamination of the cell membranes during the approach towards the cell and facilitate sealing. After formation of the giga-seal, amphotericin would diffuse towards the tip and perforate the patch of membrane in the pipette tip within 5-15 minutes.

In both configurations, Pulse's C_{slow} cancellation function was used to cancel out transient currents caused by charging of the cell's membrane. In the course of the experiment, passive C_{slow} and C_{fast} cancellation were frequently adjusted to account for changes in cell size, pipette immersion in the bath solution, and R_S . When recording K^+ currents, Pulse's active R_S compensation feature was used to compensate 70% of the R_S .

Cells were kept at a holding potential of -74 mV (recording of K^+ currents) or -84 mV (everything else).

Data analysis

All data analysis except for parts of the analysis of single unit recordings was performed with Igor Pro software (Wavemetrics, Lake Oswego, USA). Means are expressed \pm standard error of the mean (SEM) and compared using Student's unpaired t-test unless otherwise indicated, with * indicating $p < 0.05$, ** $p < 0.01$, and *** $p < 0.001$.

Ca²⁺ imaging

Ca^{2+} microdomain overview images were acquired essentially as described by Frank et al., 2009 with some slight modifications. Essentially, 6 sets of 96×96 pixel images were acquired, each set containing 2 images taken before, 2 during and 2 after a 390 ms depolarization pulse to -14 mV, with each

image taken during a period of ~180 ms. A background image was calculated as the average of all 12 acquisitions taken before depolarization and subtracted from the individual images. The images were then averaged between sets to provide views before, during and after stimulation. Overview images during stimulation were again averages of the two images acquired during depolarization. Only hotspots appearing exclusively in the two “during depolarization” images were analyzed. Laser power during acquisition was 0.5%.

To examine the spatial properties of individual hotspots, line profiles of overview images were fitted with a Gaussian function

$$f(x) = y_0 + A \times e^{-\frac{(x-x_0)^2}{width}} \quad (\text{eq. 1})$$

where y_0 is the base fluorescence, A is the amplitude, x_0 is the center of the Gaussian distribution and $width$ is its width. The amplitude of the hotspot was taken directly from this, while the full width at half maximum (FWHM) was calculated as

$$FWHM = width \times 2 \times \sqrt{\ln 2} \quad (\text{eq. 2})$$

For measuring Ca^{2+} microdomain kinetics, the laser was kept in one fixed position over the sand the resulting signal was acquired at a high sampling rate (500 kHz). In order to reduce noise, the signal was temporally averaged to yield an effective rate of 2 kHz. The laser power was reduced to 0.05% of maximum intensity. The resulting fluorescence signal was then fitted with a single exponential function

$$f(t) = y_0 + A_1 \times e^{\frac{-(t-t_0)}{\tau_1}} \quad (\text{eq. 3})$$

or, where appropriate, with a double exponential function

$$f(t) = y_0 + A_1 \times e^{\frac{-(x-x_0)}{\tau_1}} + A_2 \times e^{\frac{-(x-x_0)}{\tau_2}} \quad (\text{eq. 4})$$

where y_0 is the baseline fluorescence, A_1 is the amplitude of the first exponential, τ_1 is its time constant, and A_2 and τ_2 are the second exponential's amplitude and time constant. For later analysis, the time constants of single exponential fits were pooled with the fast time constants of double exponential fits.

Analysis of patch-clamp and Ca²⁺ imaging data

CDI in *CaBP4^{-/-}* mice was calculated by subtracting the residual normalized (I/I_{peak}) Ba²⁺ current 300 ms after the onset of depolarization from the residual normalized Ca²⁺ current, thus effectively removing the contribution of voltage-dependent inactivation to the observed decrease in current. In *Ca_vβ₂^{-/-}* mice, the changed kinetics did not allow this type of quantification, since the increase in the slow component of inactivation was cancelled out by the decrease in the fast component. Therefore, the slow component of inactivation was approximated by fitting a linear function to the last 250 ms of 500 ms depolarization-evoked currents, taking the slope as a measure of inactivation. The fast component was then taken to be the residual current after subtraction of the linear fit.

Steady-state current-voltage relationships (IVs) for Ca²⁺ and Ba²⁺ currents were calculated by plotting the average current 8-10 ms after the onset of a 10 ms depolarization to various potentials ranging from -84 to 71 mV against the depolarization potential. The depolarization potential was corrected for the voltage drop across the access resistance to the cell (series resistance, R_S) according to

$$V_{\text{corr}} = V_{\text{cmd}} - R_S \times I_{\text{steady-state}} \quad (\text{eq. 5})$$

where V_{corr} is the corrected potential, V_{cmd} is the command potential set in Pulse, R_s is the series resistance and $I_{steady-state}$ is the steady-state current of the IV.

Fractional activation curves for these currents were created by calculating the conductance of the cell as

$$G = \frac{I}{V - V_{rev}} \quad (\text{eq. 6})$$

and plotting it against the potential to which the cell was clamped. Here G is the conductance, I the Ca^{2+} or Ba^{2+} current, V the potential to which the cell was clamped and V_{rev} the current's reversal potential, which was obtained by fitting a line to the linear part of the steady-state IV-curve in the range from -4 to 16 mV (for Ca^{2+} currents) or -14 to 6 mV (for Ba^{2+} currents) and extrapolating to the potential of zero current. Analysis of these curves was performed by fitting a Boltzmann equation

$$\frac{G}{G_{max}}(V) = \frac{1}{1 + e^{\frac{V_{1/2} - V}{s}}} \quad (\text{eq. 7})$$

where G is the whole-cell conductance, G_{max} is the maximal G , V is the potential to which the cell was clamped, $V_{1/2}$ is the potential of half-maximal activation ($G / G_{max} = 0.5$) and s is the slope of activation.

Kinetics of activation were obtained by fitting a power-exponential function

$$I(t) = I_0 + \Delta I \times (1 - e^{-\frac{t}{\tau}})^2 \quad (\text{eq. 8})$$

to the current during the first 5 ms after the onset of depolarization. Here, I is the current, I_0 is the current at $t = 0$ ms, ΔI is the steady state current amplitude and τ is the time constant of activation. All currents were leak-corrected using a p/10 protocol.

For nonstationary fluctuation analysis of Ca²⁺ currents, current ensembles of 520 individual depolarizations (see Fig. 9A for the voltage protocol used) were acquired in the presence of BayK8644 to maximize currents. The variance of the tail currents recorded at -64 mV was estimated as the average of squared differences between pairs of consecutive responses, as described previously (Roberts et al., 1990; Brandt et al., 2005), to minimize the effects of Ca²⁺ current rundown. The variance was plotted against the mean current and fitted with a parabolic function

$$\text{var}(I_{mean}) = i \times I_{mean} - \frac{I_{mean}^2}{N} + \text{offset} \quad (\text{eq. 9})$$

where *var* is variance, I_{mean} is the mean current, i is the single channel current, N is the total number of Ca²⁺ channels and *offset* is the base variance. Data were only taken into account starting 700 μs after repolarization to avoid variance artifacts caused by residual capacitive transients. The maximum open probability (P_o) was then obtained from

$$P_o = \frac{I_{mean,max}}{N \times i} \quad (\text{eq. 10})$$

where $I_{mean,max}$ is the peak mean current. All currents from one ensemble were leak corrected with the same leak current averaged from two p/10 pulses, one recorded before and one after acquisition of the ensemble.

For measurements of membrane capacitance (C_m), IHCs were stimulated by depolarizations of different durations to -14 mV with interstimulus intervals of 30 to 60 s. Membrane capacitance increments (ΔC_m) were measured with the Lindau-Neher technique (Lindau and Neher, 1988) implemented in the LockIn module of the Pulse software (sine+dc), as described by Moser and Beutner, 2000. A 1kHz sinusoid with a peak-to-peak amplitude of 70 mV was applied around the holding potential of -84 mV. ΔC_m was calculated as the difference between the average C_m after the end of depolarization and that before. Segments of 400 ms were averaged to acquire the mean values, skipping the

first 40 ms after depolarization. Currents were leak corrected with a p/4 protocol. When calculating ΔC_m ratios, the errors were propagated according to

$$\sigma_R = \frac{\sqrt{\frac{\sigma_A^2}{A^2} + \frac{\sigma_B^2}{B^2}}}{R} \quad \text{eq. 11}$$

where R is the ratio A/B , σ_R is the propagated error of R , and σ_A and σ_B are the errors of A and B .

Due to the large whole-cell conductance when recording K^+ currents, even the residual (non-compensated) R_S would cause a considerable voltage error. This error was accounted for by correcting the command potential according to eq. 5. For the calculation of the average IV, the corrected data was binned in 10 mV bins.

Fractional activation curves were obtained by acquiring the tail currents 0.2 - 0.3 ms after the end of depolarization and normalizing to the maximum tail current. The data were fitted with a Boltzmann curve (eq. 7).

Kinetics of activation were acquired by fitting a double exponential function (eq. 4) to the first 20 ms of 100 ms depolarizing pulses to various potentials.

Immunohistochemistry

After preparing the organ of Corti as described above, the whole-mount preparation was fixed in methanol for 20 minutes at -20°C (for anti- $\text{Ca}_v\alpha_{1D}$ stains) or in 4% formaldehyde diluted in 120 mM phosphate buffered solution (PBS; 140 mM NaCl, 2.7 mM KCl, 8 mM Na_2HPO_4 , and 1.5 mM KH_2PO_4 .) for one hour on ice (for all other stains). After washing three times for 10 minutes in PBS, unspecific binding sites were blocked by incubating the prep in goat serum diluted buffer (GSDB; 16% normal goat serum, 450 mM NaCl, 0.3% Triton X-100, 20 mM phosphate buffer) for one hour at room temperature.

Afterwards, the sample was incubated with the primary antibodies diluted in GSDB (see table 3 for the dilutions of the individual antibodies) at 4°C overnight. The preparation was then washed three times in wash buffer

(450 mM NaCl, 0.3% Triton X-100, 20 mM phosphate buffer) and incubated in the secondary antibody solution (Alexa 488-conjugated goat-anti-rabbit and Alexa 568-conjugated goat-anti-mouse diluted in GSDB at 1:200 each) for one hour at room temperature. After washing again three times for 10 minutes in wash buffer and once for 5 minutes in 5mM PB, the preparation was mounted on a glass slide using DAKO fluorescent mounting medium (Dako, Glostrup, Denmark).

Antibody	Dilution	Source	Provider
anti-CtBP2	1:150	Mouse	BD Biosciences, San Jose, USA
anti-GluR 2/3	1:200	Rabbit	Chemicon, Billerica, USA
anti-Ca _v 1.3	1:75	Rabbit	Alomone, Jerusalem, Israel
anti-Parvalbumin 235	1:500	Mouse	Swant, Bellinzona, Switzerland
anti-BK	1:200	Rabbit	Alomone, Jerusalem, Israel
anti-Synaptophysin	1:200	Mouse	Synaptic Systems, Göttingen, Germany
anti-SK2	1:200	Rabbit	Sigma-Aldrich, München, Germany
AlexaFluor488 anti-rabbit	1:200	Goat	Invitrogen, Karlsruhe, Germany
AlexaFluor568 anti-mouse	1:200	Goat	Invitrogen, Karlsruhe, Germany

Table 3: Antibodies and dilutions used in immunohistochemistry

Samples were imaged on a Leica SP5 confocal microscope (Leica Mikrosysteme, Wetzlar, Germany) equipped with a 63 x, 1.4 NA lens. Illumination was provided by a 488 nm argon laser and a 561 nm helium-neon laser. Laser power and photomultiplier gain were adjusted to maximize the range of intensity acquisition unless indicated otherwise. The vertical step size for Z-stack recordings was 0.5 µm.

Images were processed in NIH ImageJ and assembled for display in Adobe Illustrator (Adobe Systems Inc., San Jose, USA).

Electron microscopy

Immediately following preparation, the organ of Corti whole-mounts were fixed in HEPES-HBSS containing 2.5% glutaraldehyde for 20 minutes at room temperature. The later steps were performed by Dietmar Riedel and Gudrun Heim. The samples were fixed overnight at 4°C in 100 mM cacodylate buffer containing 2.5% glutaraldehyde. After an additional fixation in 0.1% OsO₄, the samples were stained with 1% uranyl acetate, then dehydrated in a series of ethanol dilutions and finally in propylene oxide. They were then embedded in Agar 100 (Science Services, München, Germany). Thin sections (80 nm) were counterstained with lead citrate and examined using a PhilipsCM120 BioTwin transmission electron microscope (Philips). Pictures were taken with a TemCam F224A camera (TVIPS) at 20,000- fold magnification.

Single IHC RT-PCR

IHCs from the apical coils of freshly dissected organs of Corti were harvested after removing supporting cells at a high bath perfusion rate (HEPES-HBSS at 3 ml/min). The cytosol including the nucleus of each individual IHC were aspirated into a patch pipette and the pipette content was transferred into first strand cDNA synthesis mix containing (after the dilution by the pipette contents): 50 mM Tris-HCl, pH 8.3, 75 mM KCl, 5 mM MgCl₂, 5 mM DTT, 100 units of SuperScript™ II Reverse Transcriptase (Invitrogen) and 40 units RNaseOUT™ ribonuclease inhibitor (Invitrogen). Reverse transcription was performed by Anna Bulankina with oligo(dT)primers according to the manufacturer's instructions. Aspirated bath solution was used as a negative control. Each cDNA mix was used as a template for two subsequent PCR reactions with nested primers specific for Ca_vβ₁₋₄ as done previously (Knirsch, 2007) and otoferlin cDNA. Primer sequences are listed in table 4.

	Forward primer 5'-3'	Reverse primer 5'-3'
Cαvβ₁	GCCCAAGGACTTCCTACAC ATCAAGG	GGAACGCGTGTTGGAGCGC TCAATG
Cαvβ₁ nested	CTGGTGAAGGAAGGCTGCG AG	GTGTTTGCTGGGGTTGTTG AGGAC
Cαvβ₂	CTTGCCGACTATCTGGAGG CATACTG	CAGCTACCCAAACAGCTTT TGAATTGTTTCAGG
Cαvβ₂ nested	CACCCTCCCAGCGGTAACC C	GCTATTGGAGCAACAGCAA TACAAAATAGAC
Cαvβ₃	CTGTGGCATTGCTGTGAG GACCAATG	CAAAGACGATGATGGGAG CCAGTGAG
Cαvβ₃ nested	TGGGGTTCTGGATGAGGAG TGC	TGCTGGGTGGTTGATGGTG TCAG
Cαvβ₄	GTGCCCTGGACGAAGATGT GCCC	GTTGCTGTGTCTCATTCGCT GACTCTG
Cαvβ₄ nested	GACTGGTAAAAGAGGGCT GTGAGATTG	GATTGCTGTGGGATATGGT GAGAGG
otoferlin	GCAGAAGAGCAGCTATGA GC	TCTCCACAGCTAGTCCCAA C
otoferlin nested	AGACTTGTTCCCCCACTC	TTCATTCAAGTCCTGGTGC TC

Table 4: Primer sequences used for single-cell RT-PCR

Recording of ABRs and DPOAEs

Recordings of ABR and DPOAE were performed by Christian Rüdiger. Animals were anesthetized intraperitoneally with a combination of ketamine (125 mg/kg) and xylazine (2.5 mg/kg), and the heart rate was constantly monitored to control the depth of anesthesia. The core temperature was maintained constant at 37°C using a rectal temperature-controlled heat blanket (Hugo Sachs Elektronik–Harvard Apparatus, March-Hugstetten, Germany). For stimulus generation, presentation, and data acquisition, the

TDT II or III Systems (Tucker Davis Technologies, Alachua, USA) run by BioSig32 software (Tucker Davis Technologies) were used. Sound pressure levels (SPL) are provided in decibels SPL root mean square (RMS) (tonal stimuli) or decibels SPL peak equivalent (clicks) and were calibrated using a 1/4 inch Brüel and Kjær microphone (model 4939). Tone bursts (4/8/12/16/24/32 kHz, 10 ms plateau, 1 ms \cos^2 rise/fall) or clicks of 0.03 ms were presented at 20 Hz in the free field ipsilaterally using a JBL 2402 speaker. The difference potential between vertex and mastoid subdermal needles was amplified (50,000 times), filtered (low pass, 4 kHz; high pass, 100 Hz) and sampled at a rate of 50 kHz for 20 ms, 2×2000 times to obtain two mean ABRs for each sound intensity. Hearing threshold was determined with 10 dB precision as the lowest stimulus intensity that evoked a reproducible response waveform in both traces by visual inspection. For DPOAEs, a 24-bit sound card and the ED1/EC1 speaker system (Tucker David Technologies) were used to generate two primary tones f1 and f2 (f2/f1 ratio: 1.2). Primary tones were coupled into the ear canal by a custom-made probe containing an MKE 2 microphone (Sennheiser, Barleben bei Magdeburg, Germany) and adjusted to an intensity of 60 dB sound pressure level at the position of the ear drum as mimicked in a mouse ear coupler. The microphone signal was amplified (DMP3; M-audio, Hallbergmoos, Germany) and analyzed by fast Fourier transformation.

Single unit auditory nerve fiber recordings

Auditory nerve fiber recordings were performed by Anna Gehrt under supervision of Nicola Strenzke essentially as described by (Taberner and Liberman, 2005) and (Strenzke et al., 2009), using the TDT System 3 and an ELC-03XS amplifier (NPI Electronics, Tamm Germany) controlled by Matlab software (MathWorks, Natick, USA) and using free-field stimulation with a JBL 2402 (JBL Professional, Northridge, USA) speaker. Mice aged 6–10 weeks were anesthetized with urethane (1.3 mg/kg, intraperitoneally) and xylazine (5 mg/kg intraperitoneally), tracheotomized, and placed in a stereotactic apparatus. After partial removal of the left occipital bone and cerebellum, the

auditory nerve was approached through the cochlear nucleus with a glass micropipette filled with 3 M NaCl and 2% methylene blue using an Inchworm manipulator (EXFO Burleigh, Mississauga, Canada). During audiovisual detection of single-unit spiking activity, auditory nerve fibers were identified by their stereotactic position, irregular firing pattern, and their primary-like poststimulus time histogram (PSTH). Characteristic frequency (CF) and threshold (defined by a significant rate increase of 20 spikes/s within 20 ms from the start of a 15 ms tone pip, Wald's probability ratio test) were obtained with a 1/32 octave and 2 dB precision, and additional characterization was performed at CF. In fibers with poor frequency tuning, individual best frequencies were chosen manually or by systematic scanning of the receptive field. For subsequent offline spike detection using custom-written Matlab routines, recorded traces were matched to a spike template that was generated for each unit based on a manually set spike threshold value. The success of this procedure was confirmed by manual inspection of sorted waveforms.

For recording of PSTHs, $Ca_v\beta_2^{-/-}$ mice were presented with tone bursts of 130 dB SPL, the maximum intensity possible with the speaker used in these experiments, at a manually chosen best frequency. This resulted in recordings that were on average about 10 dB above the units' thresholds. Wild-type (WT) mice were presented with tone bursts at the unit's determined characteristic frequency 30 dB above threshold. Unequal absolute sound intensities were chosen for wild-type and $Ca_v\beta_2^{-/-}$ since saturation of the spike rate-sound pressure level functions of most wild-type auditory nerve fibers is expected for sound pressure levels of 20 dB greater than threshold (Taberner and Liberman, 2005) and noise damage was feared for the stimuli exceeding 100 dB SPL.

Solutions

HEPES-buffered Hanks' balanced salt solution contained (in mM):

NaCl 141.7, HEPES 10, KCl 5.36, MgCl₂ 1, MgSO₄ 0.5, glucose 2 mg/ml, L-glutamine 0.5 mg/ml. pH was adjusted to 7.2 with NaOH.

Modified Ringer's solution contained (in mM):

NaCl 107, tetraethylammonium chloride (TEA-Cl) 35, HEPES 10, 4-aminopyridine (4-AP) 5, KCl 2.8, CaCl₂ 2, MgCl₂ 1, CsCl₂ 1, glucose 2 mg/ml. pH was adjusted to 7.2 with HCl. For higher concentrations of Ca²⁺, NaCl was replaced by equimolar amounts of CaCl₂ (resulting in Ca²⁺ concentrations of 2, 5 and 10 mM). For recordings of Ba²⁺ currents, CaCl₂ was replaced by BaCl₂. For fluctuation analysis, the solution contained an additional 5 μM BayK8644. For recordings in *Ca_vβ₂^{-/-}* mice, 100 μM apamin was added to block slowly activating K⁺-currents.

Modified Ringer's solution for recording of K⁺-currents contained (in mM):

NaCl 144, HEPES 10, KCl 5.8, CaCl₂ 2, MgCl₂ 0.9, glucose 2 mg/ml. pH was adjusted to 7.2 with NaOH.

Intracellular recording solution for recording of Ca²⁺ or Ba²⁺ currents, and exocytosis contained (in mM):

Cs-gluconate 130, TEA-Cl 10, 4-AP 10, HEPES 10, MgCl₂ 1. pH was adjusted to 7.2 with HCl. For perforated patch recordings, the solution contained an additional 250 μg/ml of amphotericin B and 0.6 % DMSO. For ruptured patch recordings, the solution contained an additional 2 mM Mg-ATP and 0.3 mM Na-GTP. For hotspot recordings the solution also contained 2 mM EGTA and 400 μM Fluo-5N.

Intracellular solution for recording of K⁺-currents contained (in mM):

KCl 150, HEPES 10, MgCl₂ 1, Mg-ATP 2, Na-GTP 0.3. pH was adjusted to 7.2 with KOH.

The osmolarity of all extracellular solutions was ~300 mOsm; that of intracellular solutions was ~290 mOsm. All chemicals were obtained from Sigma-Aldrich, except for amphotericin B (Calbiochem). Cs-gluconate was prepared from CsOH and D-gluconic acid.

Results

Influence of the $Ca_v\beta_2$ subunit on Ca^{2+} currents, exocytosis and development of mouse IHCs

$Ca_v\beta$ subunits are important modulators of voltage-gated Ca^{2+} channels. To research the effects of $Ca_v\beta$ subunits on Ca^{2+} channels in IHCs, we examined a knockout mouse line lacking $Ca_v\beta_2$ in all but cardiac tissue (Ball et al., 2002).

$Ca_v\beta_2^{-/-}$ mice are profoundly hearing impaired and show defects in cochlear amplification.

Hearing capabilities of $Ca_v\beta_2^{-/-}$ mice were first examined by ABRs and DPOAEs in 3-4 week old mice. No responses could be observed in ABRs of $Ca_v\beta_2^{-/-}$ mice using tone burst stimuli reaching up to 90 dB, the maximum attainable sound intensity with the setup used here. Strong click stimuli (90 dB or above) evoked reproducible responses (Fig. 5A, B), showing that $Ca_v\beta_2^{-/-}$ mice had residual auditory sensitivity, unlike $Ca_v\alpha_{1D}^{-/-}$ mice, which are completely deaf (Fig. 5A, B; see also Platzner et al., 2000).

DPOAE, caused by nonlinear amplification by OHCs, were detected in all tested wild-type mice (p21 to p28, Fig. 5C, D). In $Ca_v\beta_2^{-/-}$ mice, only 2 out of 10 tested animals showed a greatly decreased response (p20 to p31, Fig. 5C, D). However, OHCs are present throughout the organ of Corti and appear intact by visual inspection. All three rows of OHCs are visible from the apical part of the organ of Corti (see Fig. 5E, F for transmission light micrographs of 3-4 week old acute explants) down to the basal part (see Fig. 5G for phalloidin-stained OHCs in an 8-week-old formaldehyde-fixed organ of Corti).

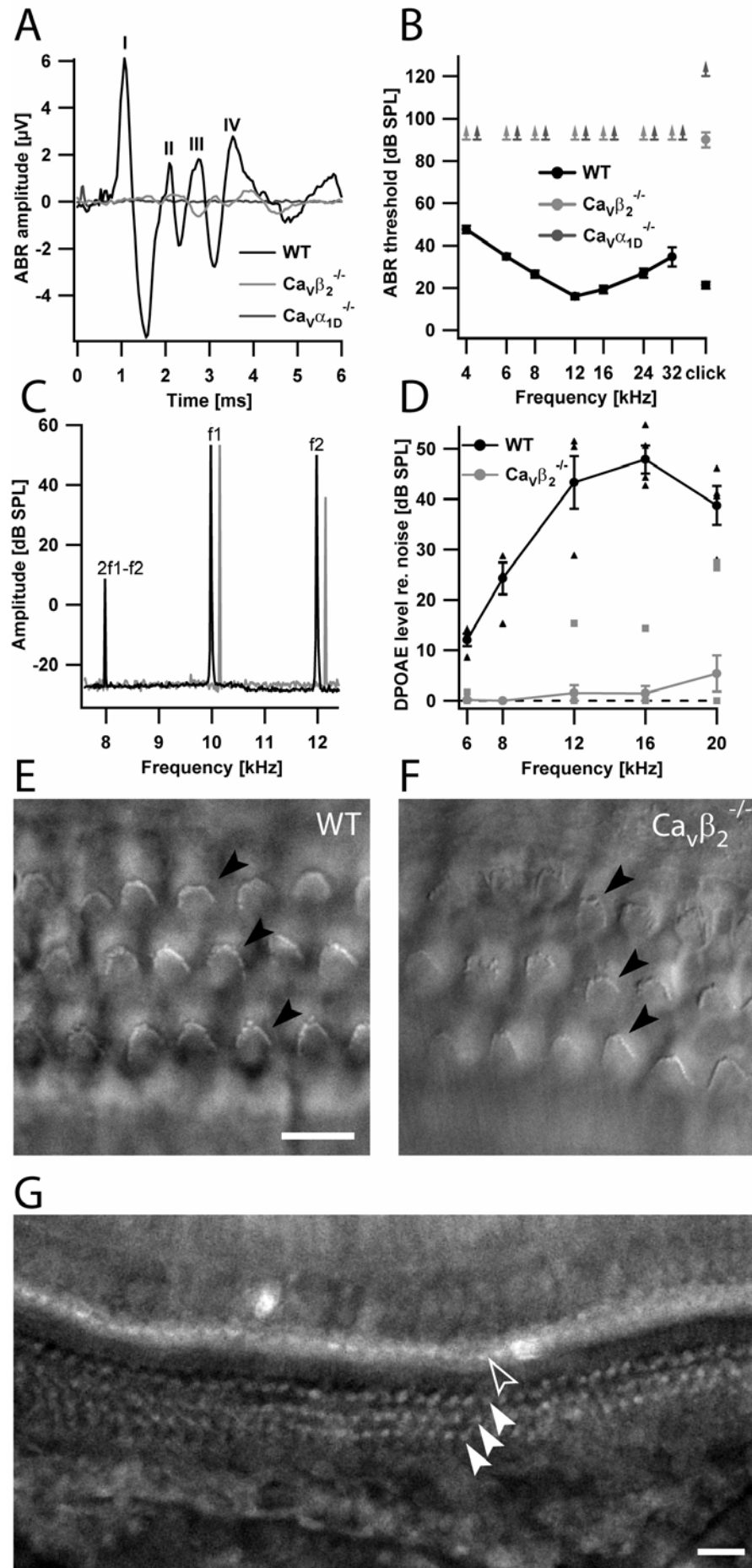


Figure 5: Auditory systems physiology and OHCs in $Ca_v\beta_2^{-/-}$ and wild-type mice.

A, Grand average of ABR waves elicited by suprathreshold click stimuli (100 dB peak equivalent) in wild-type (black, n = 9) and $Ca_v\beta_2^{-/-}$ (light grey, n = 5) mice. For comparison, the average ABR wave of $Ca_v\alpha_{1D}^{-/-}$ mice (dark grey, n = 2) is shown, which lack a detectable response to 100 dB clicks. Roman numerals indicate the individual ABR peaks arising from the neurons of the ascending auditory pathway. ABRs were recorded by Christian Rüdiger.

B, Hearing thresholds obtained by ABR recordings. The average threshold of $Ca_v\beta_2^{-/-}$ (light grey, n = 5 mice) amounts to 90 dB for clicks and exceeds 90 dB (SPL RMS, the highest sound pressure level tested) for 4-32 kHz tone bursts. For comparison the mean audiograms of wild-type (black, n = 9) and $Ca_v\alpha_{1D}^{-/-}$ (dark grey, n = 2, no detectable responses to clicks even at 120 dB SPL) mice are shown.

C, Representative power spectrum of the microphone signal showing primary tones (f1 and f2, 60 dB SPL) and DPOAE at 2f1-f2 in the wild-type mouse (black). The trace of the $Ca_v\beta_2^{-/-}$ mouse (grey) is laterally offset by 150 Hz for better readability and shows no detectable DPOAE signal. DPOAEs were recorded by Christian Rüdiger.

D, Grand averages of DPOAE levels (relative to the noise floor): sizable DPOAE across all tested frequencies in wild-type mice (black, n = 4), absent DPOAEs in the lower frequency range, and considerably weaker if present at all in the higher frequency range in $Ca_v\beta_2^{-/-}$ mice (grey, n = 10). The markers represent data points of measurements from individual mice.

E, F, Representative contrast enhanced transmission images of the apical organ of Corti of wild-type (E) and $Ca_v\beta_2^{-/-}$ (F) mice. Three rows of intact OHCs with V-shaped hair bundles are present in both wild-type and $Ca_v\beta_2^{-/-}$ mice at 4 weeks of age (arrowheads). Scale bar is 10 μ m.

Figure 5 (continued)

G, Phalloidin-stained explant of the basal turns of a 4-week-old $Ca_v\beta_2^{-/-}$ organ of Corti. The hair bundles on top of the single row of IHCs (open arrowhead) and the three rows of OHCs (closed arrowheads) are visible. Sample was prepared and stained by Nicola Strenzke. Scale bar is 20 μm .

$Ca_v\beta_2$ mRNA is the predominant isoform expressed in wild-type IHCs.

To ascertain which $Ca_v\beta$ subunits are present in IHCs, we tested the expression of all four known $Ca_v\beta$ variants on the mRNA level by RT-PCR. After isolating mRNA from samples of the entire bony cochlea, we subjected it to reverse transcription and performed a multiplex PCR for preamplification of all isoforms of $Ca_v\beta$ followed by an isoform-specific nested PCR. We found expression of all four isoforms of $Ca_v\beta$ in the cochlea (Fig. 6A).

To further investigate at the level of individual cells, we harvested single IHCs and isolated mRNA from these. *Otoferlin*, a hair cell specific marker (Roux et al., 2006), was used as positive control (Fig. 6B). In two separate assays analyzing 8 cells each, $Ca_v\beta_2$ mRNA was found in 14 of 16 wild-type IHCs but in none of the 16 $Ca_v\beta_2^{-/-}$ IHCs. In few wild-type and $Ca_v\beta_2^{-/-}$ IHCs we also detected mRNA for $Ca_v\beta_1$ (wild-type: 1 out of 16; $Ca_v\beta_2^{-/-}$: 2 out of 16) and $Ca_v\beta_3$ (wild-type: 4 out of 16, $Ca_v\beta_2^{-/-}$: 0 out of 16) but not for $Ca_v\beta_4$. While the single-cell PCR data does not allow quantification of mRNA levels, the reliable detection of $Ca_v\beta_2$ mRNA compared to the scarce identification of other $Ca_v\beta$ mRNAs indicates that $Ca_v\beta_2$ mRNA is the most abundant $Ca_v\beta$ transcript in IHCs.

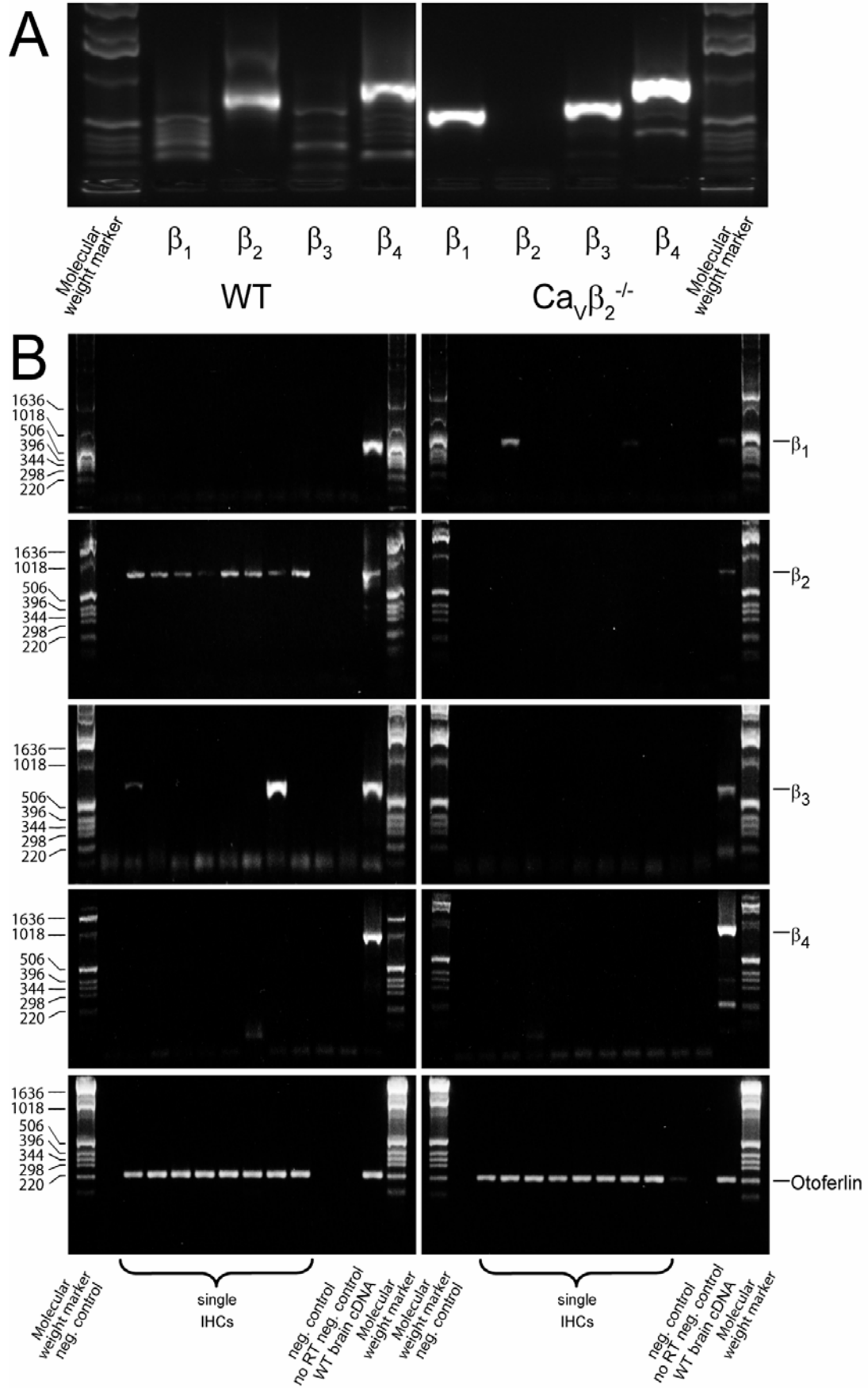


Figure 6 (overleaf): RT-PCR and single-cell RT-PCR detection of $Ca_v\beta$ subunits in the organ of Corti and individual IHCs of $Ca_v\beta_2^{-/-}$ and wild-type mice.

A, Detection of $Ca_v\beta_{1-4}$ mRNA by RT-PCR in the entire cochlea of wild-type (left) and $Ca_v\beta_2^{-/-}$ (right) mice. Expected sizes of the PCR products are 552 bp, 703 bp, 621 bp, 872 bp and 217 bp for $Ca_v\beta_1$, $Ca_v\beta_2$, $Ca_v\beta_3$, $Ca_v\beta_4$ and *otoferlin*, respectively. RT-PCR was conducted by Anna Bulankina.

B, Detection of $Ca_v\beta_{1-4}$ and *otoferlin* (positive control) mRNA (from top to bottom) by RT-PCR in 8 single wild-type (left panels) and $Ca_v\beta_2^{-/-}$ IHCs (right panels). Expected PCR product sizes are as above. The RT-PCR was also tested by applying wild-type brain cDNA (positive control), as well as reactions without reverse transcriptase (no RT neg. control) and reactions in which only bath solution close to the cells was aspirated (neg. control). RT-PCR was conducted by Anna Bulankina.

IHC Ca^{2+} currents are greatly reduced in $Ca_v\beta_2^{-/-}$ mice.

IHCs of 3-4 week old $Ca_v\beta_2^{-/-}$ mice were examined by performing perforated-patch recordings in extracellular solution containing 2, 5 or 10 mM Ca^{2+} . We found that Ca^{2+} currents were drastically reduced at all potentials tested (by approximately 70%, Fig. 7A, 4A). As in wild-type mice, the remaining Ca^{2+} current of $Ca_v\beta_2^{-/-}$ IHCs still appeared to be mediated by L-type channels, since it was augmented by the dihydropyridine agonist BayK8644 by an amount similar to that observed in wild-type IHCs (~70% higher Ca^{2+} currents in the presence of BayK8644 in $Ca_v\beta_2^{-/-}$ vs. ~60% higher currents in wild-type, Fig. 7C, D). Voltage-dependence of activation showed a slight but significant shift of half-maximal activation towards more negative potentials when using Ca^{2+} as charge carrier (wild-type IHCs $V_{1/2} = -18.0 \pm 1.0$ mV, $Ca_v\beta_2^{-/-}$ IHCs $V_{1/2} = -23.8 \pm 1.7$ mV; $p < 0.05$ using the Wilcoxon rank test; Fig. 7E), which, however, could not be observed when substituting Ba^{2+} for Ca^{2+} (wild-type

IHCs $V_{1/2} = -34.6 \pm 3.0$ mV, $Ca_v\beta_2^{-/-}$ IHCs $V_{1/2} = -35.0 \pm 4.2$ mV; $p = 0.8579$ using the Wilcoxon rank test; Fig. 7F). The kinetics of activation were essentially unchanged (Fig. 7G, H), except for a slight shift towards more negative potentials.

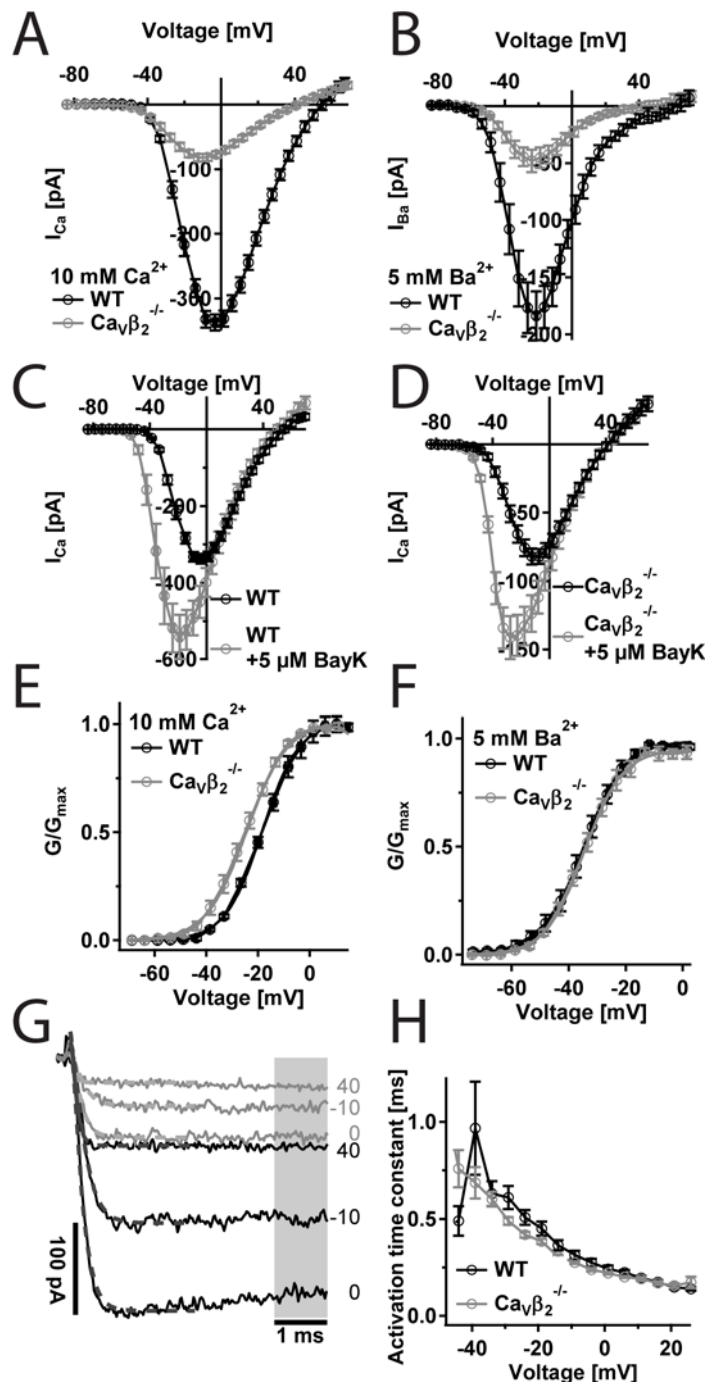


Figure 7: Ca^{2+} and Ba^{2+} currents in $Ca_v\beta_2^{-/-}$ and wild-type IHCs.

A, Current-voltage (IV) relationship for wild-type (black, $n = 8$) and $Ca_v\beta_2^{-/-}$ (grey, $n = 8$) IHCs in 10 mM $[Ca^{2+}]_e$. Ca^{2+} currents were measured 8 ms after the onset of a 10 ms depolarization to the indicated potentials.

B, IV relationship, measured as in A, with 5 mM $[Ba^{2+}]_e$ replacing Ca^{2+} .

C, IV relationship of wild-type IHCs in 10 mM $[Ca^{2+}]_e$ measured in the presence (grey, $n = 8$) and absence (black, $n = 8$) of 5 μ M BayK8644. The peak Ca^{2+} current is increased by $\sim 60\%$.

D, IV relationship as in C of $Ca_v\beta_2^{-/-}$ IHCs in the presence (grey, $n = 8$) and absence (black, $n = 8$) of 5 μ M BayK8644. The peak Ca^{2+} current is increased by $\sim 70\%$.

Figure 7 (continued)

E, Activation curves for Ca^{2+} currents in wild-type (black) and $\text{Ca}_v\beta_2^{-/-}$ (grey), acquired from the same data used in A. G/G_{max} curves were calculated according to eq. 6 and fitted with a Boltzmann equation (eq. 7) in order to obtain $V_{1/2}$ and the slope of activation.

F, Activation curves for Ba^{2+} currents calculated as in E from the same data used in B.

G, Sample Ca^{2+} currents recorded by depolarizations to the indicated potentials (in mV) in 10 mM $[\text{Ca}^{2+}]_e$ from wild-type (black) and $\text{Ca}_v\beta_2^{-/-}$ IHCs (grey). The dashed lines indicate the power exponential fits used to measure the activation time constant shown in H, and the shaded area indicates the period from which the current was averaged for plotting the IV relationships in A, B, C, and D.

H, Activation time constants of Ca^{2+} currents evoked by depolarization to various potentials in wild-type (black, $n = 8$) and $\text{Ca}_v\beta_2^{-/-}$ (grey, $n = 8$) IHCs were approximated by fitting a power exponential function (eq. 8) to the first 5 ms of the current.

The slow component of CDI is accelerated in $\text{Ca}_v\beta_2^{-/-}$ IHCs.

By replacing external Ca^{2+} with Ba^{2+} we could distinguish voltage-dependent inactivation from CDI. Voltage-dependent inactivation appeared mostly unaltered in $\text{Ca}_v\beta_2^{-/-}$ IHCs (mean slope of $0.167 \pm 0.026 \text{ s}^{-1}$ for wild-type and $0.218 \pm 0.054 \text{ s}^{-1}$ for $\text{Ca}_v\beta_2^{-/-}$; $p = 0.413$ using the Wilcoxon rank test; Fig. 8C, E). However, VDI in $\text{Ca}_v\beta_2^{-/-}$ IHCs appeared slightly more linear than in wild-type. CDI in $\text{Ca}_v\beta_2$ -deficient IHCs, on the other hand, was clearly altered: it lacked the fast component and displayed an accelerated linear slow component (Fig. 8A, B). Approximation of the slow component by fitting of a linear function to the last 250 ms of the normalized current (Fig. 8D, E) resulted in an average slope of $0.275 \pm 0.042 \text{ s}^{-1}$ for wild-type and a

significantly higher slope of $0.663 \pm 0.047 \text{ s}^{-1}$ for $\text{Ca}_v\beta_2^{-/-}$ IHCs ($p < 0.001$ using the Wilcoxon rank test).

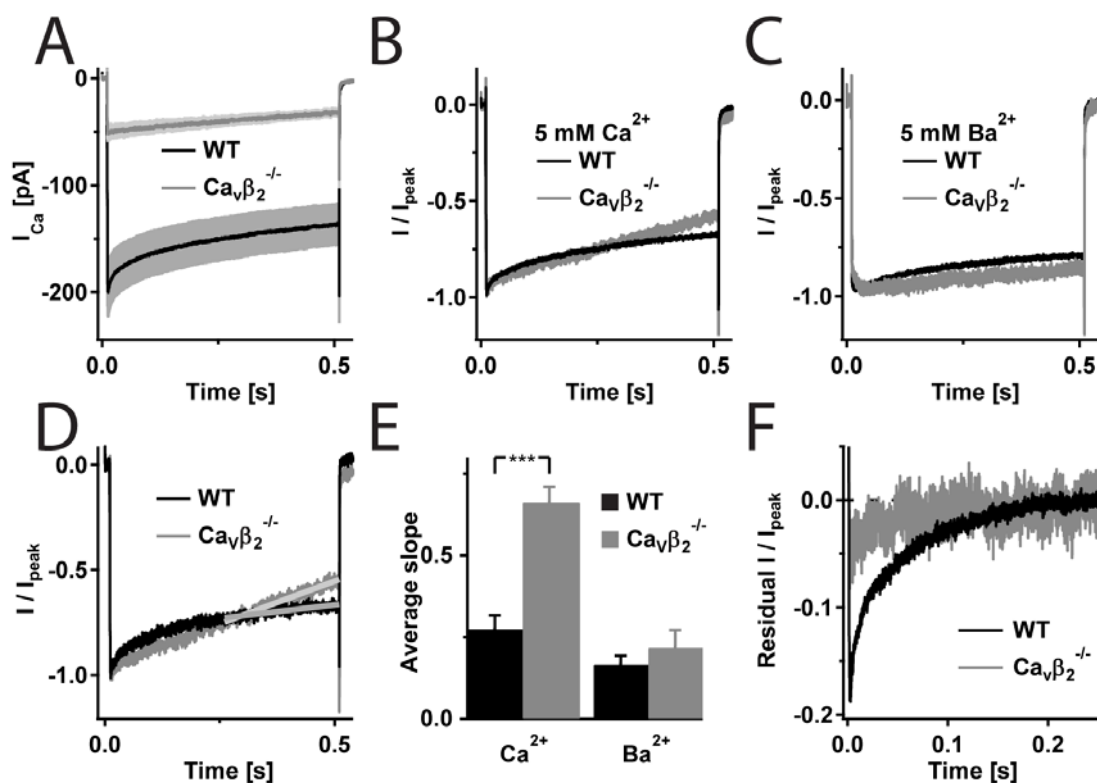


Figure 8: CDI and VDI in $\text{Ca}_v\beta_2^{-/-}$ and WT IHCs.

A, Average Ca^{2+} currents evoked by 500 ms depolarizations to -14 mV in wild-type (black, $n = 11$) and $\text{Ca}_v\beta_2^{-/-}$ (grey, $n = 7$) IHCs in $5 \text{ mM } [\text{Ca}^{2+}]_e$. Shaded areas indicate the SEM of the average traces.

B, Average I_{Ca} as in A, but normalized to peak current. Note that Ca^{2+} current inactivation is accelerated in $\text{Ca}_v\beta_2^{-/-}$ but lacks a fast component.

C, Average normalized currents as in B but recorded in $5 \text{ mM } [\text{Ba}^{2+}]_e$ from wild-type (black, $n = 11$) and $\text{Ca}_v\beta_2^{-/-}$ (grey, $n = 7$) IHCs.

D, Representative normalized Ca^{2+} currents from a wild-type (black) and a $\text{Ca}_v\beta_2^{-/-}$ (grey) IHC. Light grey lines indicate the linear fits used to approximate the slow component of inactivation.

Figure 8 (continued)

E, Average slope of line fits used to approximate the slow component of inactivation as shown in D. The difference between the slopes of Ca^{2+} currents in wild-type and $\text{Ca}_v\beta_2^{-/-}$ is significant at $p < 0.001$ using the Wilcoxon rank test.

F, Representative residual currents obtained by subtracting the line fits shown in D from the normalized current traces.

The number of Ca^{2+} channels is greatly reduced in $\text{Ca}_v\beta_2^{-/-}$ IHCs.

To find out whether the reason underlying the reduction in Ca^{2+} current amplitude was a reduction in the overall number of Ca^{2+} channels or a reduction in single-channel conductance or open probability, we performed non-stationary fluctuation analysis on depolarization-evoked Ca^{2+} tail currents in the presence of BayK8644 (see Fig. 9A for voltage protocol and representative mean current and variance traces). As before, Ca^{2+} currents were reduced by ~70% and variance showed a similar reduction (Fig. 9B). Analysis of the acquired data indicated a ~60% decrease in the number of functional channels (1298 ± 100 in wild-type vs. 596 ± 98 in $\text{Ca}_v\beta_2^{-/-}$; $p < 0.001$ using the Wilcoxon rank test; Fig. 9C), while there was only a slight and non-significant reduction in single-channel current (0.59 ± 0.06 pA in wild-type vs. 0.48 ± 0.03 pA in $\text{Ca}_v\beta_2^{-/-}$; $p = 0.128$ using the Wilcoxon rank test) and maximum open probability (0.82 ± 0.06 in wild-type vs. 0.69 ± 0.09 in $\text{Ca}_v\beta_2^{-/-}$; $p = 0.233$ using the Wilcoxon rank test).

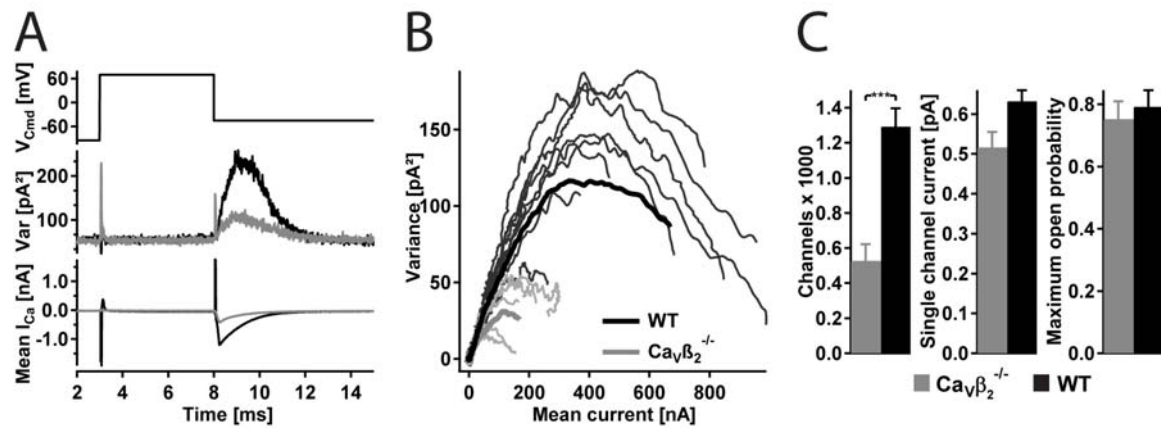


Figure 9: Nonstationary fluctuation analysis of Ca^{2+} currents in $\text{Ca}_v\beta_2^{-/-}$ and wild-type IHCs.

A, Voltage-clamp protocol (top), variance (middle) and mean Ca^{2+} current (bottom) calculated from a representative p/n corrected ensemble of 520 sweeps used to determine one of the wild-type variance-mean plots in B.

B, Ca^{2+} current variance versus mean for 8 wild-type (black) and 6 $\text{Ca}_v\beta_2^{-/-}$ (grey) IHCs. Thin lines represent individual measurements, bold lines indicate the average.

C, Averages of the number of Ca^{2+} channels (left), the single channel currents (middle) and the maximum open probability (right) from wild-type (black, n = 8) and $\text{Ca}_v\beta_2^{-/-}$ (grey, n = 6) IHCs obtained by nonstationary fluctuation analysis of the data shown in B according to equations 9 and 10. The difference in channel number is significant at $p < 0.001$ using the Wilcoxon rank test.

The number of ribbon synapses in $\text{Ca}_v\beta_2^{-/-}$ IHCs is unchanged.

We calculated the average number of ribbon synapses per IHC in the apical turn of the organ of Corti from IHCs immunostained for CtBP2 (staining the nucleus and the presynaptic ribbon) and GluR2/3 (staining the postsynaptic glutamate receptors). By counting colocalized spots immunopositive for both antigens (Fig. 10) and dividing by the number of nuclei in one stack of

confocal sections, we arrived at an average of 11.5 ± 0.3 synapses per IHC in wild-type ($n = 40$ IHCs; 5 mice) and 11.3 ± 0.3 in $Ca_V\beta_2^{-/-}$ ($n = 37$ IHCs; 3 mice), concluding that the number of ribbon synapses is unaltered in $Ca_V\beta_2^{-/-}$ IHCs.

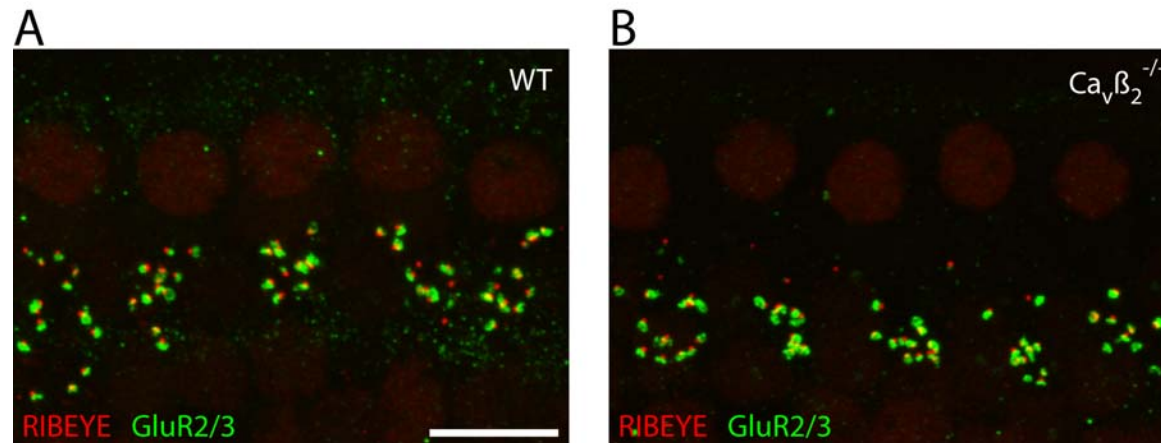


Figure 10: Ribbon synapses in the $Ca_V\beta_2^{-/-}$ and wild-type organ of Corti.

A and B, Representative projections of confocal sections of IHCs following immunolabeling of ribbons (anti-CtBP2, red) and GluR2/3 receptors (anti-GluR2/3), green obtained from wild-type (A) and $Ca_V\beta_2^{-/-}$ (B) mice. Synapses are visible as juxtaposed pairs of red and green fluorescent dots and the number of imaged cells is obtained by counting the CtBP2-stained nuclei of IHCs. Scale bar is 10 μm .

Localization of Ca^{2+} channels is normal in $Ca_V\beta_2^{-/-}$.

As could be expected from the findings of a reduced number of Ca^{2+} channels, immunohistochemical staining for the $Ca_V\alpha_{1D}$ subunit of the $Ca_V1.3$ Ca^{2+} channel showed strongly decreased signals. While colocalization of $Ca_V\alpha_{1D}$ -immunopositive spots with CtBP2-positive spots (designating synaptic ribbons; (Khimich et al., 2005) was clearly visible in wild-type animals

(Fig. 11A), only very weak immunofluorescence for $\text{Ca}_V\alpha_{1D}$ was visible at the ribbon synapse in $\text{Ca}_V\beta_2^{-/-}$ IHCs (Fig. 11B). Unfortunately, the $\text{Ca}_V\alpha_{1D}$ antibody shows a considerable amount of unspecific staining, as is also visible in the results obtained by another study (Brandt et al., 2005), where unspecific staining was also found in the $\text{Ca}_V\alpha_{1D}^{-/-}$ mouse with the same protocol used here. We therefore favor the interpretation that immunopositive spots outside the ribbon synapse area represent unspecific staining rather than mislocalized channels. Because of this uncertainty and since we could not completely exclude possible contamination by bleed-through it was not straightforward to judge whether localization of Ca^{2+} channels at the synapse was still intact.

Since immunostaining did not allow us to definitively verify the localization of $\text{Ca}_V1.3$ channels at the $\text{Ca}_V\beta_2^{-/-}$ IHC synapse, we examined local Ca^{2+} influx in IHCs on a confocal setup using the Ca^{2+} indicator Fluo-5N. As has been shown before (Frank et al., 2009), Ca^{2+} influx at wild-type synapses can be seen as fluorescent hotspots revealing a local increase of Ca^{2+} upon depolarization of the cell (Fig. 11C). To test whether Ca^{2+} influx as small as that observed in $\text{Ca}_V\beta_2^{-/-}$ IHCs could still be detected by this method, we blocked ~75 % of the Ca^{2+} current in wild-type IHCs by adding 10 μM of the dihydropyridine L-type channel blocker isradipine to the extracellular solution. We could still find hotspots in these cells, with reduced intensities but unchanged spatiotemporal properties (Fig. 11D, F, G, H). The data gathered from $\text{Ca}_V\beta_2^{-/-}$ cells were similar, with a ~50 % reduction in fluorescence compared to untreated wild-type cells but unchanged activation time constant and width (Fig. 11E, F, G, H).

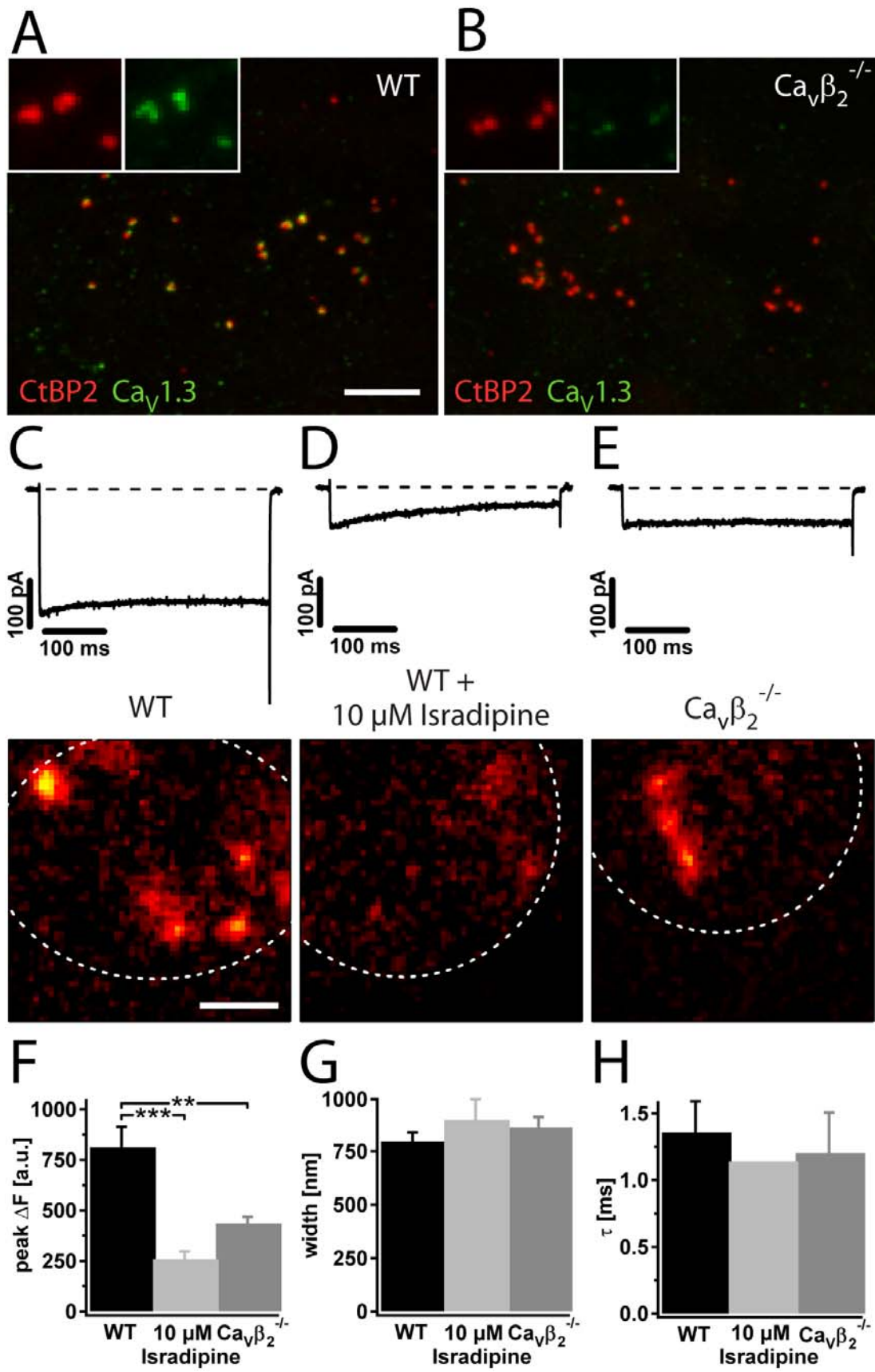


Figure 11: Ca^{2+} channel localization in $\text{Ca}_v\beta_2^{-/-}$ and WT IHCs.

A and B, representative projections of confocal sections from wild-type (A) and $\text{Ca}_v\beta_2^{-/-}$ (B) IHCs immunolabeled for synaptic ribbons (anti-CtBP2, red) and the $\text{Ca}_v\alpha_{1D}$ subunit of the $\text{Ca}_v1.3$ channel (anti- $\text{Ca}_v1.3$, green). In wild-type, there is a clear overlap (yellow) indicating co-localization of Ca^{2+} channel clusters and ribbons. Scale bar is 5 μm . Insets show separated color channels at a higher magnification (field of view: $3.27 \times 3.27 \mu\text{m}$).

C – E, Representative Ca^{2+} current traces from a wild-type IHC (in response to 390 ms step depolarizations to -14 mV) in the absence (C) and from another wild-type IHC in the presence (D) of 10 μM of the L-type Ca^{2+} channel blocker Isradipine, as well as a $\text{Ca}_v\beta_2^{-/-}$ IHC (E). Below, confocal scans of the corresponding cells during depolarization (dashed lines indicate the outlines of the cells) filled with 400 μM of the fluorescent Ca^{2+} indicator Fluo-5N and 2 mM of the Ca^{2+} chelator EGTA through a patch pipette. The images are averages of 6 consecutive recordings. Hotspots of Ca^{2+} entry can be recognized in all three cells.

F, Average peak fluorescence of Ca^{2+} microdomains derived from Gaussian fits (eq. 1) to line profiles of individual hotspots. The difference between wild-type ($n = 24$ hotspots from 6 IHCs) and Isradipine-blocked wild-type ($n = 11$ hotspots from 4 IHCs) is significant at $p < 0.001$, that between wild-type and $\text{Ca}_v\beta_2^{-/-}$ ($n = 23$ hotspots from 7 IHCs) is significant at $p < 0.01$.

G, Average full width at half maximum (see eq. 2) obtained from the same Gaussian fits as in F.

H, Average (fast) activation time constants of fluorescence increase derived from high temporal resolution point scans of individual Ca^{2+} microdomains ($n = 17$ hotspots from 8 wild-type IHCs; $n = 2$ hotspots from 2 Isradipine-treated wild-type IHCs and $n = 9$ hotspots from 5 $\text{Ca}_v\beta_2^{-/-}$ IHCs).

The localization of the Ca^{2+} -hotspots to the ribbon synapse was confirmed in experiments where the ribbons were labeled with a fluorescently labeled RIBEYE-binding peptide introduced via the patch-pipette as described by Zenisek et al., 2004 and Frank et al., 2009. Depolarization-induced Ca^{2+} -hotspots clearly colocalized with fluorescently labeled ribbons (Fig. 12) with only few labeled ribbons showing no local Ca^{2+} increase upon depolarization (28 hotspots at 30 labeled ribbons in wild-type and 11 hotspots at 13 labeled ribbons in $\text{Ca}_v\beta_2^{-/-}$ IHCs).

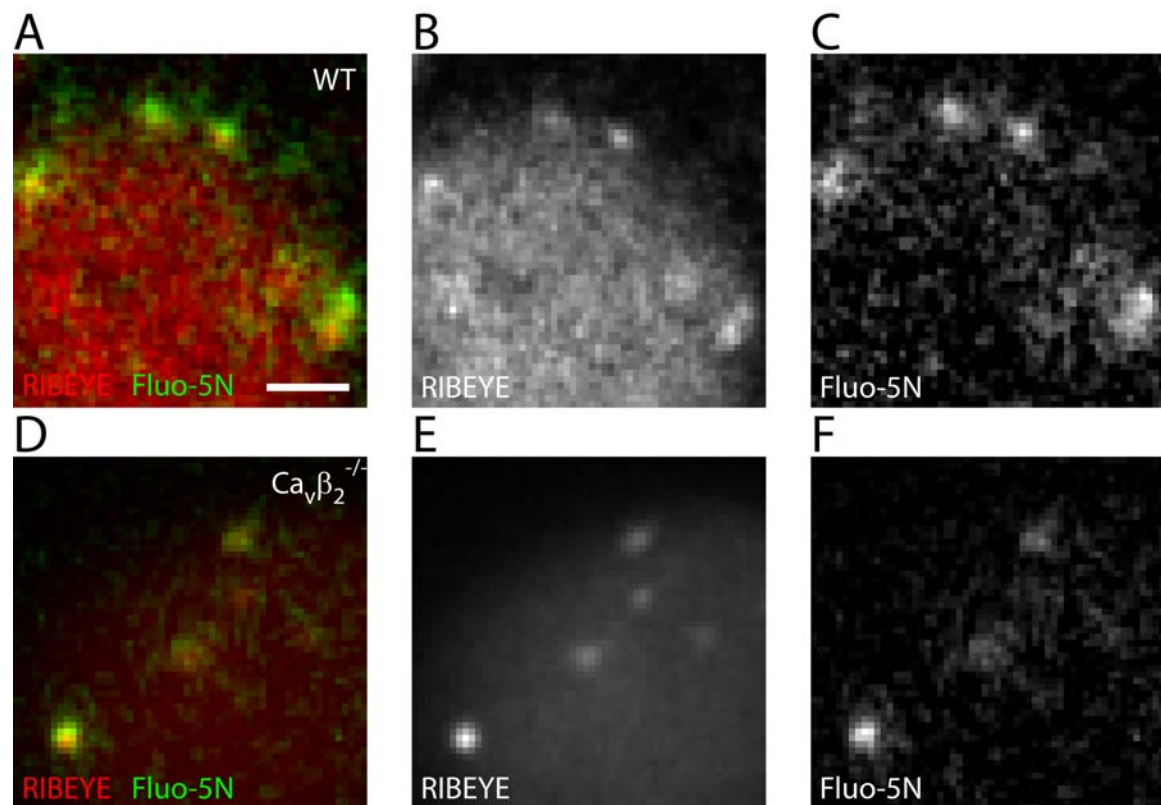


Figure 12: Colocalization of ribbons and Ca^{2+} hotspots in $\text{Ca}_v\beta_2^{-/-}$ and wild-type IHCs.

A and D, Exemplary Ca^{2+} microdomains evoked by 390 ms step depolarizations to -14 mV (averages of 6 consecutive recordings) in wild-type (A) and $\text{Ca}_v\beta_2^{-/-}$ (D) IHCs. The cells were patched with 400 μM of the fluorescent Ca^{2+} indicator Fluo-5N, 40 μM of fluorescently labeled CtBP2/RIBEYE-staining peptide (Zenisek et al., 2004) and 2 mM of the Ca^{2+} chelator EGTA in the patch pipette. In red is

Figure 12 (continued)

displayed the signal from the peptide interacting with the RIBEYE protein, a component of the synaptic ribbon. In green is displayed the change in fluorescence of the Fluo-5N Ca^{2+} indicator during depolarization of the cell. Scale bar is 2 μm .

B and C, Separated channels showing the ribbon label (B) and the Ca^{2+} microdomain (C) from the wild-type cell.

E and F, Separated channels showing the ribbon label (E) and the Ca^{2+} microdomain (F) from the $\text{Ca}_v\beta_2^{-/-}$ cell.

Exocytosis is greatly reduced in $\text{Ca}_v\beta_2^{-/-}$ IHCs

To assess whether exocytosis was working normally in $\text{Ca}_v\beta_2^{-/-}$ IHCs, we examined membrane capacitance increments (ΔC_m) evoked by depolarizing the cell for different durations. We found that exocytosis was greatly reduced in $\text{Ca}_v\beta_2^{-/-}$ IHCs (Fig. 13C), such that measurements were difficult due to the low signal-to-noise ratio when using 2 mM extracellular Ca^{2+} . To get better readings, we increased the Ca^{2+} -concentration to 10 mM, thus also increasing exocytosis (Fig. 13D). We found that exocytosis was reduced by two thirds compared to wild-type, which is comparable to the reduction in Ca^{2+} current. More specifically, on average exocytosis in 10 mM Ca^{2+} caused by 20 ms depolarizations, which primarily recruit vesicles from the RRP, was reduced by 68% while the Ca^{2+} influx was reduced by 67%. Similarly, 100 ms depolarizations, evoking sustained exocytosis after depletion of the RRP, resulted in a 62% reduction of exocytosis while Ca^{2+} influx was reduced by 68%.

Keeping the reported interaction between $\text{Ca}_v\beta$ subunits and RIM in mind, we examined the nanodomain localization of Ca^{2+} channels in $\text{Ca}_v\beta_2^{-/-}$ mice. To this end, we performed ruptured-patch experiments in which we monitored depolarization-evoked exocytosis with 5 mM of the Ca^{2+} buffer EGTA in the

patch-pipette. This restricts the diffusion of free Ca^{2+} ions to a smaller volume around the mouth of the open channel and thereby allows access of Ca^{2+} ions only to proteins situated in very close proximity ($< \sim 40$ nm distance) to the Ca^{2+} channel. If the Ca^{2+} sensor for exocytosis was no longer located as close to the channel in $\text{Ca}_v\beta_2^{-/-}$ IHCs, one would expect a stronger decrease of ΔC_m responses in these cells as compared to wild-type. However, we found that exocytosis was reduced by similar amounts relative to perforated-patch recordings in wild-type and $\text{Ca}_v\beta_2^{-/-}$ IHCs (Fig. 13E, F), suggesting that coupling of Ca^{2+} channels at release sites was unimpaired in the knockout mice.

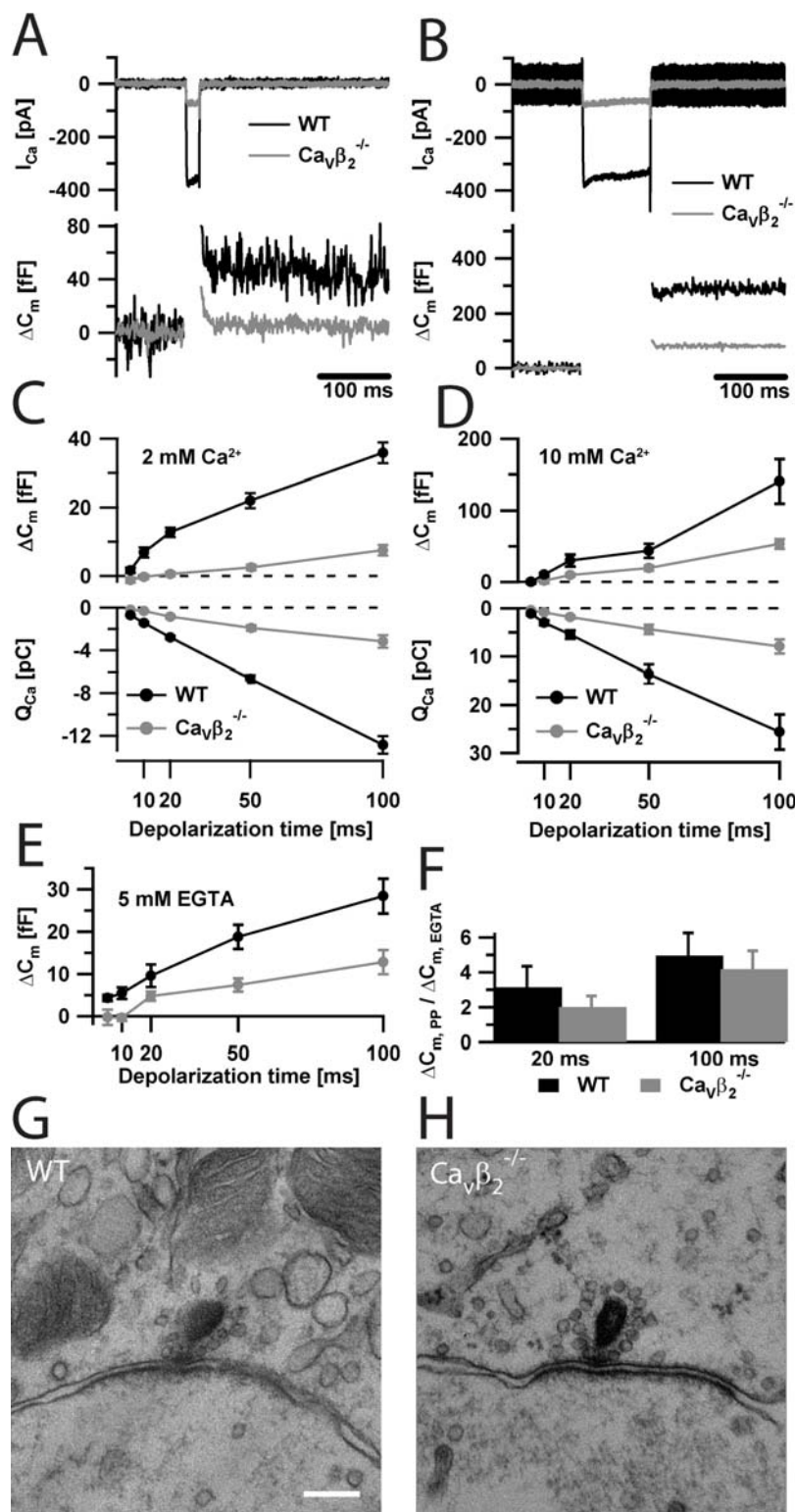


Figure 13: Exocytosis and synapse ultra-structure in $Ca_v\beta_2^{-/-}$ and wild-type IHCs.

A and B, Representative Ca^{2+} currents (I_{Ca} , top) and membrane capacitance changes (ΔC_m , bottom) elicited by step depolarizations to -14 mV for 20 ms (A) and 100 ms (B) in wild-type (black) and $Ca_v\beta_2^{-/-}$ IHCs. The extracellular solutions contained 10 mM $[Ca^{2+}]_e$ and the recordings were done in the perforated patch configuration.

C, Average ΔC_m and Q_{Ca} for step depolarizations to -14 mV of varying durations in wild-type (black, n = 11) and $Ca_v\beta_2^{-/-}$ (grey, n = 13) IHCs in 2 mM $[Ca^{2+}]_e$ obtained in the perforated patch configuration.

Figure 13 (continued)

D, Average ΔC_m and Q_{Ca} as in C, recorded in 10 mM $[Ca^{2+}]_e$ from wild-type (black, $n = 7$) and $Ca_v\beta_2^{-/-}$ (grey, $n = 8$) IHCs.

E, Average ΔC_m for various depolarization durations in wild-type (black, $n = 9$) and $Ca_v\beta_2^{-/-}$ (grey, $n = 7$) IHCs, recorded in 10 mM $[Ca^{2+}]_e$ in ruptured patch whole-cell configuration with 5 mM EGTA in the pipette solution.

F, Ratio of exocytosis between perforated patch ($\Delta C_{m, PP}$, endogenous Ca^{2+} buffer) and ruptured patch ($\Delta C_{m, EGTA}$, 5 mM EGTA) configuration for wild-type and $Ca_v\beta_2^{-/-}$ IHCs for 20 and 100 ms long depolarizations. The errors were propagated from the SEM of the mean responses in perforated patch and ruptured patch experiments according to eq. 11.

H and I, Electron micrographs of synaptic ribbons in wild-type (H) and $Ca_v\beta_2^{-/-}$ (I) IHCs. Scale bar is 200 nm.

Single unit recordings in $Ca_v\beta_2^{-/-}$ show residual sound encoding.

To examine the implications of the reduced neurotransmitter release from $Ca_v\beta_2^{-/-}$ IHCs on the auditory system in more detail, Anna Gehrt, under supervision of Nicola Strenzke, performed extracellular recordings of auditory nerve activity with microelectrodes targeted to the cochlear nucleus and the auditory nerve (Taberner and Liberman, 2005; Strenzke et al., 2009). We found that sound-driven activity of single fibers was scarce and only appeared at very high sound intensities (> 100 dB SPL). We focused our analysis on units that, based on the position of the microelectrode and the unit's discharge pattern, were most likely auditory nerve fibers, ignoring other types of sound-responsive cells. Frequency tuning of single units in $Ca_v\beta_2^{-/-}$ mice was found to be much broader than in wild-type, which is consistent with the lack of DPOAE in these mice.

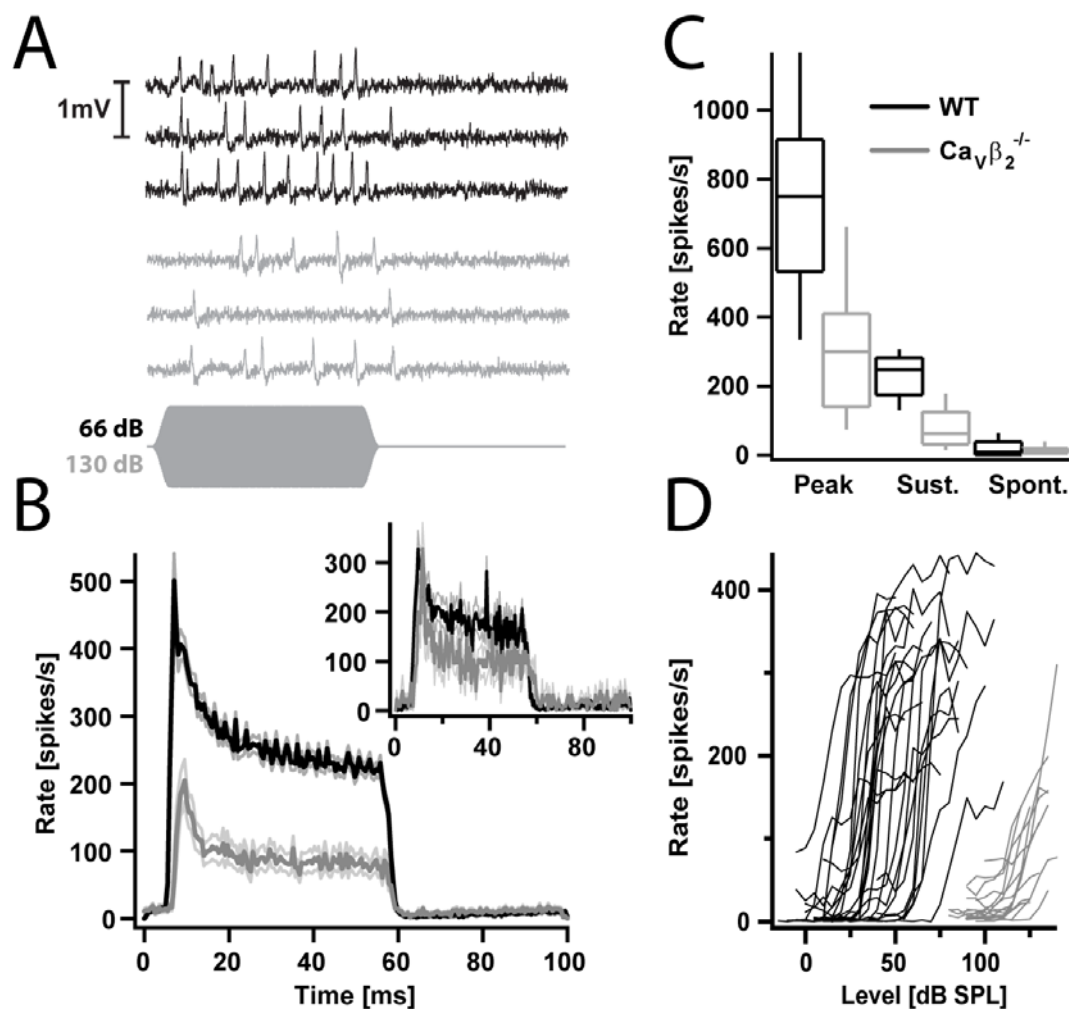


Figure 14: Single unit recordings auf auditory neurons in $Ca_v\beta_2^{-/-}$ and wild-type mice.

A, Representative original recording traces of wild-type (black) and $Ca_v\beta_2^{-/-}$ (grey) mouse auditory nerve fibers to three repetitions of a 50 ms tone burst (depicted below). Mean stimulus intensity for standard PSTHs was 66 dB for wild-type recordings (30 dB above threshold) and 130 dB for $Ca_v\beta_2^{-/-}$ (maximal speaker output). Recordings were performed by Anna Gehrt.

B, Averaged PSTH \pm SEM from wild-type (black, n = 55) and $Ca_v\beta_2^{-/-}$ (grey, n = 21) primary-like units. Inset shows a subset of recordings where all units were stimulated at 10 dB above threshold (wild-type black, n = 26, $Ca_v\beta_2^{-/-}$ grey, n = 10). Recordings were performed by Anna Gehrt.

Figure 14 (continued)

C, Bar plot of peak, sustained (average rate at 40-50 ms after stimulus onset) and spontaneous rates of the primary-like units analyzed in B. Data was analyzed by Anna Gehrt and Nicola Strenzke.

D, Rate-level-function, showing the spike rates, averaged over the duration of the stimulus, of individual wild-type (black, n = 26) and $Ca_v\beta_2^{-/-}$ (grey, n = 10) primary-like units stimulated at increasing sound pressure levels. Data was analyzed by Anna Gehrt and Nicola Strenzke.

Comparison of the acquired PSTHs (Fig. 14B, C) revealed that peak and adapted spike rates were reduced by 60% and 70%, respectively, in $Ca_v\beta_2^{-/-}$ mice. Spike rate adaptation was slightly faster in $Ca_v\beta_2^{-/-}$ mice, with an average time constant of 4.6 ± 0.9 ms from n = 21 $Ca_v\beta_2^{-/-}$ units versus 7.8 ± 0.9 ms from n = 30 wild-type units. The difference was significant at $p < 0.05$. Spontaneous spiking activity was reduced to a lesser degree (Fig. 14C). When comparing a subset of $Ca_v\beta_2^{-/-}$ and wild-type PSTHs that were recorded 10 dB above threshold, we found a lower difference in peak and sustained spike rates of only 40% (Fig. 14B, inset) . Altogether, while hearing thresholds in $Ca_v\beta_2^{-/-}$ mice are greatly increased, residual sound encoding still was present.

IHC development is impaired in $Ca_v\beta_2^{-/-}$ mice.

To determine if the reduced Ca^{2+} currents resulted in impaired development of IHCs, as has been reported for $Ca_v\alpha_{1D}^{-/-}$ mice (Brandt et al., 2003; Nemzou N. et al., 2006), we examined the expression of K^+ channels, which is specifically regulated during maturation of IHCs.

Immunostaining of wild-type IHCs for BK channels shows characteristic channel clusters at the neck of the IHC (Fig. 15A; see also Pyott et al., 2004; Hafidi et al., 2005; Nemzou N. et al., 2006). $Ca_v\beta_2^{-/-}$ IHCs lacked these

clusters (Fig. 15B, C). Closer examination with higher excitation and detection sensitivity however revealed a faint diffuse staining of the IHC plasma membrane (Fig. 15C), which could not be observed in wild-type cells.

In line with this observation, the fast component of unblocked K⁺ currents ($I_{K, f}$, representing current carried by BK channels, see Kros and Crawford, 1990) recorded in $Ca_v\beta_2^{-/-}$ IHCs was greatly diminished, but not completely absent (as is the case in $Ca_v\alpha_{1D}^{-/-}$ mice, see Brandt et al., 2003; Fig. 15E). Interestingly, in addition to the ~75% reduction in current at the end of 3 ms long depolarizing pulses, the recordings from $Ca_v\beta_2^{-/-}$ IHCs also revealed a large shift of activation towards more depolarized potentials (Fig. 15F). The average potential of half-maximal activation ($V_{1/2}$), measured from tail currents after 3 ms depolarizing pulses, was, -22.85 ± 4.27 mV in wild-type, while that of $Ca_v\beta_2^{-/-}$ cells was 10.80 ± 4.04 mV. The slope of activation was also changed, from 8.7 ± 0.1 mV in wild-type to 1.5 ± 0.7 mV in $Ca_v\beta_2^{-/-}$, indicating a shallower voltage-dependence (Fig. 15F). Both differences are significant at $p < 0.001$. The kinetics of activation were comparable at the respective $V_{1/2}$ (Fig. 15G), but seemed to reach a plateau in $Ca_v\beta_2^{-/-}$ at larger time constants than in wild-type at the most depolarized potentials.

The difference of the average K⁺ currents at the end of 3 ms depolarizing pulses (9 ± 2.57 nA when depolarizing to ~ -4 mV; Fig. 15E) was similar to that at the end of 100 ms depolarizing pulses (8 ± 1.9 nA), suggesting that the slow K⁺ currents were mostly normal in $Ca_v\beta_2^{-/-}$ IHCs.

Furthermore, some but not all adult $Ca_v\beta_2^{-/-}$ IHCs showed immunolabeling for small conductance Ca²⁺ activated potassium channels (SK2) which colocalized with synaptophysin labeling (Fig. 15I), indicating the continued presence of efferent synapses contacting the IHC itself. This is another sign of impaired development, since direct efferent contacts on IHCs with adjacent SK2 channels are a sign of immature cells and are typically lost around p10. The identity of SK2 channels was further confirmed by the presence of slowly activating outward currents present in some $Ca_v\beta_2^{-/-}$ IHCs during long depolarizations, which could readily be blocked by addition of 100 nM apamin to the extracellular solution (Fig. 15L). This kind of current was never encountered in adult wild-type IHCs. Electron micrographs of $Ca_v\beta_2^{-/-}$ IHCs

also showed direct efferent contacts at the IHC membrane in some cells (Fig. 15K), which were not found in wild-type cells (Fig. 15J).

Other signs of delayed development, however, were not visible. For example we did not find spontaneous Ca^{2+} -driven action potentials (Fig. 15M), which are present in immature wild-type IHCs and can still be found in IHCs of mature (post-p14) *Pax8*^{-/-} mice, which also show developmental impairments in the IHCs. Also, in wild-type as well as *Ca_vβ₂*^{-/-} IHCs, we observed an inward current which deactivated during hyperpolarization (Fig. 15N) and was most likely carried by KCNQ channels, a K^+ channel that is activated at low potentials and sets the resting potential of IHCs (Marcotti et al., 2003; Oliver et al., 2003; Kharkovets et al., 2006). The current was identical in both mouse lines (-136 ± 31 pA in wild-type vs. -145 ± 72 pA in *Ca_vβ₂*^{-/-} at -124 mV, Fig. 15O).

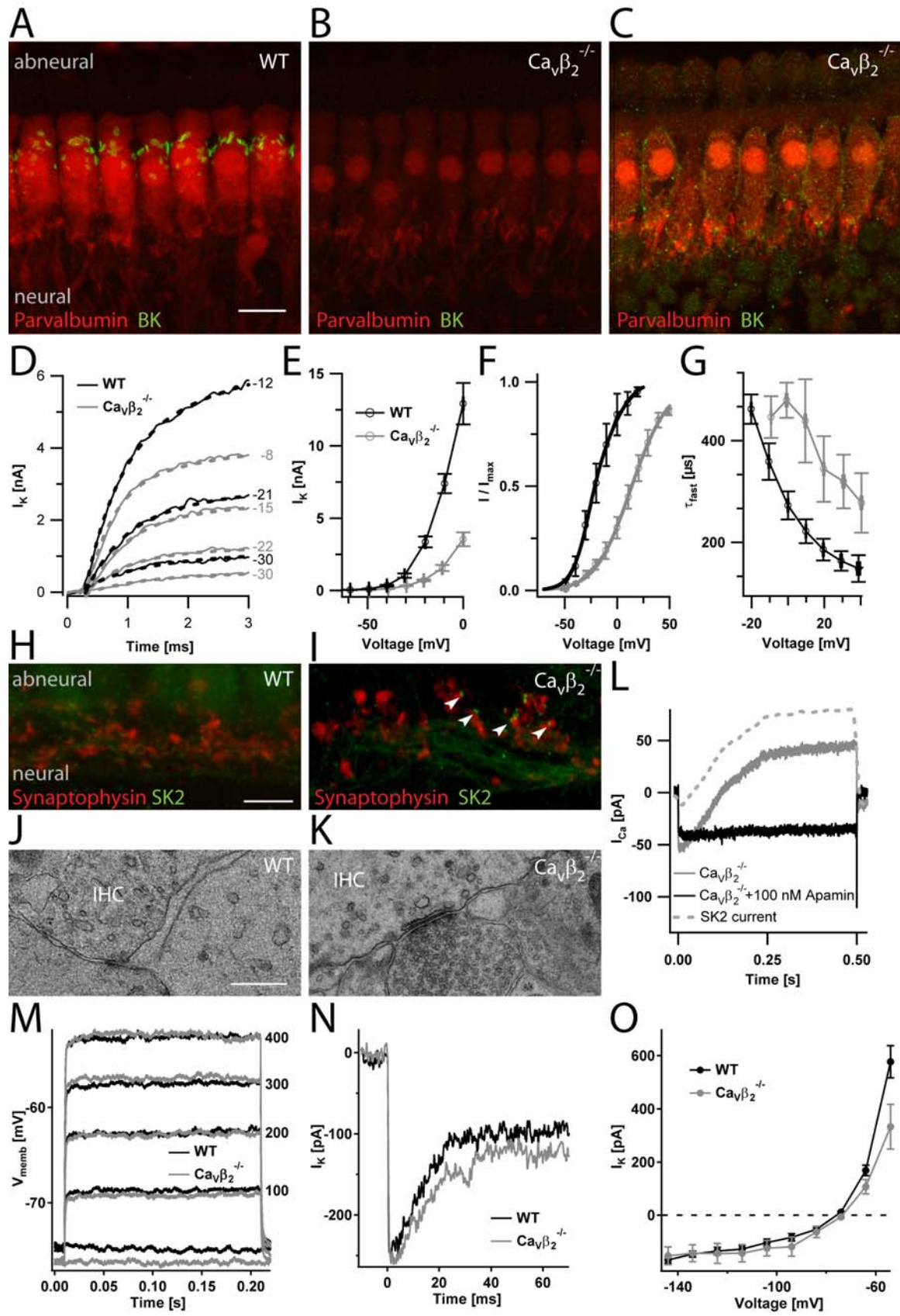


Figure 15 (overleaf): Developmental defects in the $Ca_v\beta_2^{-/-}$ organ of Corti.

A and B, Projections of confocal sections from the apical turns of representative wild-type (A) and $Ca_v\beta_2^{-/-}$ (B) organs of Corti immunostained for parvalbumin (red) and BK channels (green). Tissue was processed identically and images were acquired under identical conditions. Clusters of BK channels are found at the necks of wild-type IHCs but not in $Ca_v\beta_2^{-/-}$ IHCs. Scale bar is 10 μm .

C, Single confocal section from data in B imaged at optimized settings (higher laser power and gain) reveals faint BK-immunofluorescence along the entire IHC membrane, which was not observed in mature or immature wild-type animals.

D, The first 3 ms of K^+ currents recorded in response to 100 ms depolarizations to the potentials indicated (in mV) from a representative wild-type (black) and $Ca_v\beta_2^{-/-}$ (grey) IHC. The dashed lines indicate double-exponential fits which revealed the activation time constants shown in G.

E, IV relationships of K^+ currents from wild-type (black, $n = 20$) and $Ca_v\beta_2^{-/-}$ (grey, $n = 5$) IHCs obtained from averaging the current during the last 0.5 ms of 3 ms long step depolarizations to various potentials. The effectively reached depolarizations were corrected for R_s -induced voltage errors according to eq. 5.

F, Average fractional activation curves acquired from measuring the tail currents between 0.2 and 0.3 ms after the end of 3 ms depolarizing step pulses to various potentials (same data set as in E). Markers present average data, continuous lines are averaged fits according to eq. 7. The differences in slope (8.7 ± 0.1 mV in wild-type vs. 15.2 ± 0.7 mV in $Ca_v\beta_2^{-/-}$) and those in $V_{1/2}$ (-22.9 ± 4.3 mV in wild-type vs. 10.8 ± 4.0 mV in $Ca_v\beta_2^{-/-}$) are significant at $p < 0.001$.

G, Average fast activation time constant of the K^+ currents obtained by fitting a double exponential function to the first 20 ms of 100 ms long step depolarization pulses to the potentials indicated, as illustrated in D.

Figure 15 (continued)

H and I, Maximum projections of immunostainings for synaptophysin (red) and SK2 channels (green) imaged in the basal regions of IHCs from a wild-type (G, 21 days old) and a $Ca_v\beta_2^{-/-}$ (H, 23 days old) mouse. The green haze in the background arises from pillar cells, which often show unspecific immunoreactivity. Note, however, the presence of SK2-positive spots in $Ca_v\beta_2^{-/-}$ (arrowheads) which can be seen in some, but not all $Ca_v\beta_2^{-/-}$ IHCs and which is absent from mature wild-type IHCs. Scale bar is 5 μ m.

J and K, Representative electron micrographs of the basal IHC plasma membrane from wild-type (J) and $Ca_v\beta_2^{-/-}$ (K) mice. The IHC label indicates the cytoplasm of the hair cell. Note the vesicle-filled terminal of an efferent fiber contacting the $Ca_v\beta_2^{-/-}$ IHC (K). Efferent synapses on IHCs were frequently observed in mature $Ca_v\beta_2^{-/-}$ mice (n = 2 cochleae), but never in mature wild-type mice (J, n = 2 cochleae). Scale bar is 500 nm.

L, Apamin-sensitive current in a representative recording from a $Ca_v\beta_2^{-/-}$ IHC in response to a 500 ms long step depolarization to -14 mV (Cs^+ -based pipette solution, extracellular solution containing 5 mM $[Ca^{2+}]_e$): Current before (grey) and after (black) addition of 100 nM apamin to the extracellular solution as well as the difference current (dotted line). The small inward component observed in the difference current reflects Ca^{2+} current rundown during the wash-in of apamin.

M, Representative current-clamp recordings (K^+ -based pipette and extracellular solution) from mature wild-type (black) and $Ca_v\beta_2^{-/-}$ (grey) IHCs in response to step-like injections of the indicated currents (in pA). No Ca^{2+} -action potentials were observed in wild-type (n = 23) or $Ca_v\beta_2^{-/-}$ (n = 8) IHCs.

N, Representative inactivating KCNQ-like inward currents recorded in wild-type (black) and $Ca_v\beta_2^{-/-}$ (grey) IHCs in response to hyperpolarizations to -120 mV.

Figure 15 (continued)

O, IV relationship measured between 1 and 2 ms after the start of a 100 ms hyperpolarizing pulse from wild-type (black, n = 17) and $Ca_v\beta_2^{-/-}$ (grey, n = 7) IHCs, showing hyperpolarization-induced KCNQ-like inward currents.

Regulation of CDI by CaBP4

A hallmark feature of $Ca_v1.3$ channels is the very pronounced CDI which can be observed when expressing the channel in transfected cells (see Xu and Lipscombe, 2001; Koschak et al., 2001). However, $Ca_v1.3$ -carried Ca^{2+} currents in IHCs show very little CDI (see Figs. 8A, B, 16A, B, also Platzer et al., 2000). CaBPs have been known to suppress CDI (Lee et al., 2002) and CaBP4 had been proposed to be the major regulator in mouse IHCs (Yang et al., 2006) due to its presence in mature IHCs and its role in regulating the related $Ca_v1.4$ channel in photoreceptor nerve terminals (Haeseleer et al., 2004).

To explore the importance of CaBP4 in mouse IHCs, we examined auditory system physiology and the function of IHCs in $CaBP4^{-/-}$ mice (Haeseleer et al., 2004).

CDI is only slightly accelerated in $CaBP4^{-/-}$ mice

We performed perforated-patch recordings of IHCs from acute explants of the apical coil of the organ of Corti as described above in 5 mM extracellular Ca^{2+} and Ba^{2+} to measure CDI in these cells. We found a slightly stronger inactivation of depolarization-evoked Ca^{2+} currents in $CaBP4^{-/-}$ mice as compared to wild-type (Fig. 16A), but no change in Ba^{2+} currents (Fig. 16B). Calculation of CDI as the difference of residual normalized Ba^{2+} and Ca^{2+} currents showed that it was indeed only very slightly increased (Fig. 16C, changed from -0.08 in wild-type to -0.13 in $CaBP4^{-/-}$ IHCs, $p < 0.05$).

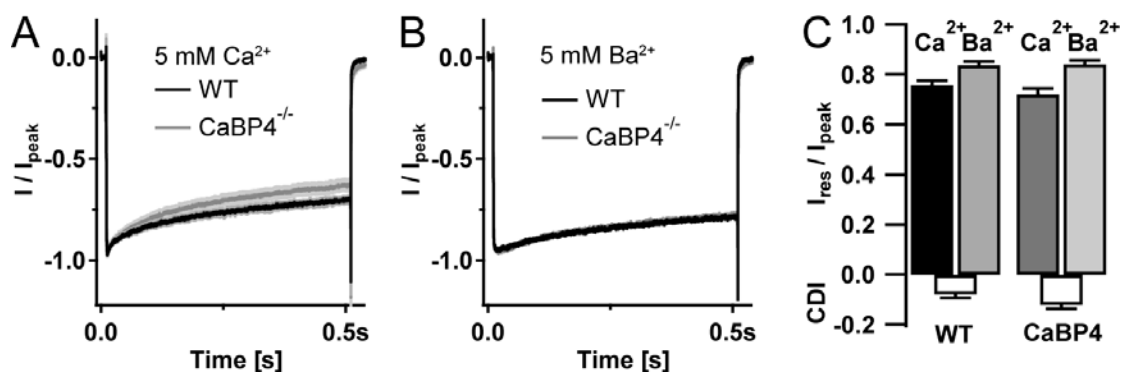


Figure 16: CDI and VDI in $CaBP4^{-/-}$ and wild-type IHCs.

A, Average Ca^{2+} currents evoked by 500 ms depolarizations to -14 mV and normalized to peak current from wild-type (black, n = 12) and $CaBP4^{-/-}$ (grey, n = 14) IHCs in 5 mM $[Ca^{2+}]_e$. Shaded areas indicate the SEM of the average traces.

B, Average normalized currents as in A but recorded in 5 mM $[Ba^{2+}]_e$ from wild-type (black, n = 12) and $CaBP4^{-/-}$ (grey, n = 14) IHCs.

C, I_{res}/I_{peak} for Ca^{2+} and Ba^{2+} currents and CDI measured in wild-type (left) and $CaBP4^{-/-}$ (right) IHCs. I_{res}/I_{peak} was calculated as the residual current after 300 ms divided by the peak current, CDI was calculated as the difference in I_{res}/I_{peak} between Ca^{2+} and Ba^{2+} currents.

Ca^{2+} influx and exocytosis are normal in $CaBP4^{-/-}$ mice

Consequently, perforated-patch recordings carried out in 2 mM extracellular Ca^{2+} showed little difference between wild-type and $CaBP4^{-/-}$ mice. Recordings of membrane capacitance increments reported unchanged exocytosis (Fig. 17A, B) and analysis of the associated Ca^{2+} currents showed no major change in the Ca^{2+} influx (Fig. 17B).

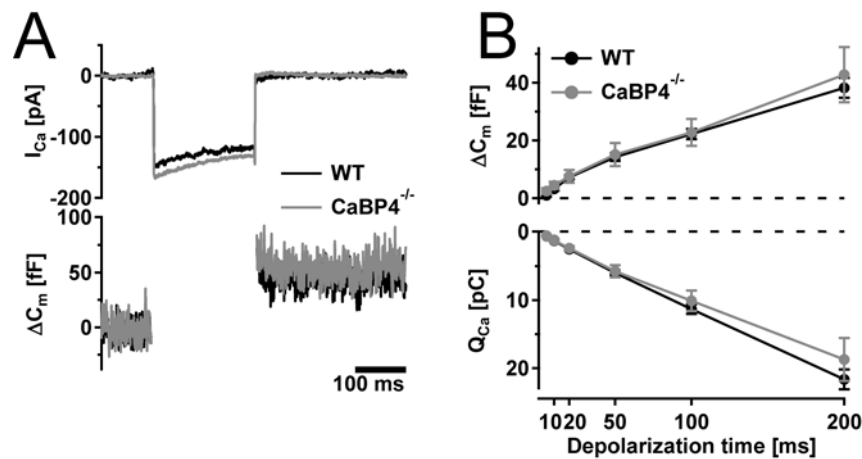


Figure 17: Exocytosis in *CaBP4*^{-/-} and wild-type IHCs.

A, Representative Ca²⁺ currents (I_{Ca} , top) and membrane capacitance changes (ΔC_m , bottom) elicited by step depolarizations to -14 mV for 200 ms in wild-type (black) and *CaBP4*^{-/-} IHCs (grey). The extracellular solutions contained 2 mM [Ca²⁺]_e and the recordings were performed in the perforated patch configuration.

B, Average ΔC_m and Q_{Ca} for step depolarizations to -14 mV of varying durations in wild-type (black, $n = 25$) and *CaBP4*^{-/-} (grey, $n = 7$) IHCs in 2 mM [Ca²⁺]_e obtained in the perforated patch configuration. A large part of the recordings was performed by Alexander Meyer.

Auditory systems function is not impaired in *CaBP4*^{-/-} mice

As expected from the *in vitro* results, when performing ABRs in 4 week old *CaBP4*^{-/-} and wild-type mice as described above, we found no differences in ABR waveforms and hearing thresholds in response to click and toneburst stimuli (Fig. 18A, B).

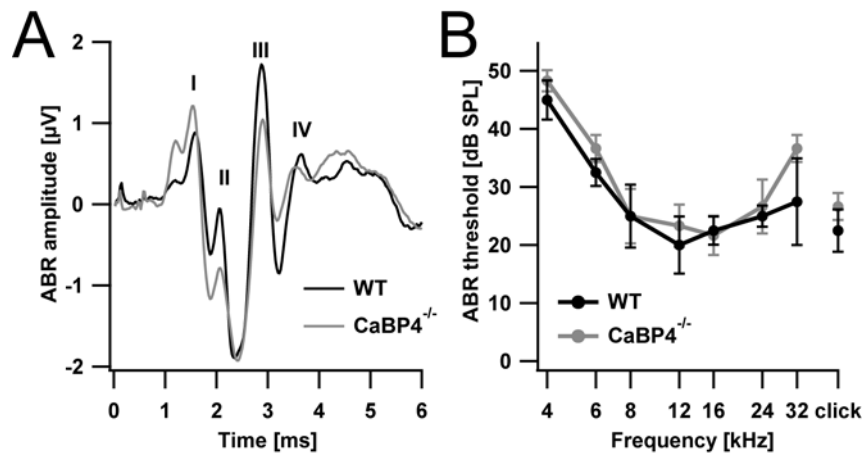


Figure 18: Auditory systems physiology in *CaBP4*^{-/-} and wild-type.

A, Grand average of ABR waves elicited by suprathreshold click stimuli (80 dB peak equivalent) in wild-type (black) and *CaBP4*^{-/-} (light grey) mice. Roman numerals indicate the individual ABR peaks arising from the neurons of the ascending auditory pathway. ABRs were recorded by Christian Rüdiger.

B, Hearing thresholds obtained by ABR recordings from wild-type (black) and *CaBP4*^{-/-} (light grey) obtained by tone burst and click stimulation.

Discussion

VGCCs in IHCs are regulated in a number of ways. Here, two types of molecules interacting with the pore-forming $Ca_v\alpha_1$ subunit have been examined by studying knockout animals generated for the $Ca_v\beta_2$ VGCC subunit and for *CaBP4*. When interpreting the data presented here, we should keep in mind that ablation of individual genes leaves room for compensation by similar ones, limiting conclusions on the role the gene product is playing under normal conditions. On the other hand, the ablation might have secondary effects (like the impairment of IHC development observed here in the $Ca_v\beta_2^{-/-}$ mouse) which make it hard to deduce the acute role of the protein in the fully developed organism. Therefore, more temporally-precise interference with the gene (for example by siRNA) might lead to different effects.

Regulation of IHC Ca^{2+} channels by $Ca_v\beta$ subunits

The results of this study show that $Ca_v\beta_2$ is the major $Ca_v\beta$ isoform in IHCs and is of critical importance for hearing. In IHCs, it regulates Ca^{2+} channel abundance at the plasma membrane, most probably by enhancing trafficking of $Ca_v\alpha_1$ subunits. It is not absolutely required for channel clustering and stimulus-secretion coupling. However, the decreased Ca^{2+} currents in $Ca_v\beta_2^{-/-}$ mice result in a commensurate decrease in exocytosis and consequently auditory nerve fiber spiking. Furthermore, $Ca_v\beta_2$ is required for normal development of IHCs, probably by ensuring neonatal, regenerative Ca^{2+} signaling. Finally, we found a defect in OHC-mediated cochlear amplification in $Ca_v\beta_2^{-/-}$ mice which requires further investigation.

Ca_vβ subunits present in IHCs

Opposite to previous a study stating that Ca_vβ₂ is not expressed in the mouse cochlea (Green et al., 1996), our RT-PCR experiments have shown transcripts for Ca_vβ₂ as well as other Ca_vβ subunits in the organ of Corti and in IHCs. In fact, judged from the strong phenotype and ubiquitous presence of Ca_vβ₂ mRNA in IHCs, we conclude that Ca_vβ₂ appears to be the predominant Ca_vβ subunit in IHCs. Ca_vβ₁ and Ca_vβ₃ mRNA were detected only infrequently in the single-cell PCR. While this method does not allow for quantification of mRNA transcripts or even protein levels, we favor the interpretation that the sporadic signals for Ca_vβ₁ and Ca_vβ₃ are the result of a low level of expression of these subunits and do not indicate higher expression by a low fraction of the total IHC population. An upregulation of Ca_vβ₁ or Ca_vβ₃ expression in Ca_vβ₂^{-/-} IHCs, as might be concluded from the stronger bands for these subunits in Fig. 6A, could not be verified in the single-cell RT-PCR experiments.

Deafness phenotype of Ca_vβ₂^{-/-} mice.

Our measurements of auditory function demonstrate pronounced deafness of Ca_vβ₂^{-/-} mice in combination with a strong impairment of cochlear sound amplification (as reported by the complete lack of otoacoustic emissions in most animals tested (Fig. 5) and the deficit in frequency tuning observed in single auditory neuron recordings (Fig. 14)). The mechanism underlying this apparent OHC dysfunction remains to be examined. In Ca_vα_{1D}^{-/-} mice, a degeneration of outer hair cells can be observed starting from an age of around 2 weeks in the apical turn (Platzer et al., 2000) and in BK^{-/-} mice from an age of around 8 weeks in the basal turn (Rüttiger et al., 2004). In Ca_vβ₂^{-/-} mice, intact rows of OHCs were found in the apical and basal turns and the cells appeared normal by visual inspection (Fig. 5). However, no mice older than 4 weeks were examined here, so a later degeneration cannot be excluded.

The impairment of active amplification by OHCs cannot fully explain the observed elevation of auditory threshold by 70 dB or more, as this accounts for a maximal gain in hearing sensitivity of around 50 dB (Ryan and Dallos, 1975), leading us to ask the question whether synaptic transmission from IHCs to spiral ganglion neurons remained functional in $Ca_v\beta_2^{-/-}$ mice.

Role of $Ca_v\beta_2$ at the IHC synapse

Our data show a strong reduction of membrane-standing Ca^{2+} channels in $Ca_v\beta_2^{-/-}$ IHCs, but seemingly intact localization of these remaining channels at the ribbon synapse. Except for the decrease in whole-cell current caused by a reduction of membrane-standing Ca^{2+} channels, only CDI was appreciably changed in $Ca_v\beta_2^{-/-}$ IHCs. The remaining examined properties of Ca^{2+} currents – activation kinetics, voltage dependence of activation, single channel conductance and open probability – appeared largely unchanged. The slight shift in voltage dependence of activation observed when using Ca^{2+} but not Ba^{2+} as charge carrier is likely to be caused by incomplete blocking of K^+ currents. Ba^{2+} is known to be a very potent inhibitor of K^+ currents. Thus the difference in activation of Ca^{2+} currents might be explained by the difference in amplitude and voltage dependence of activation of K^+ currents in $Ca_v\beta_2^{-/-}$ and wild-type IHCs.

The finding of a reduced number of Ca^{2+} channels could be explained by the proposed vital role of $Ca_v\beta$ subunits in trafficking of $Ca_v\alpha_1$ subunits towards the plasma membrane (Bichet et al., 2000). While a $Ca_v\beta$ -independent surface expression of $Ca_v\alpha_1$ subunits as proposed by (Ravindran et al., 2008) cannot be excluded, we favor the hypothesis that a low expression level of $Ca_v\beta_1$ and $Ca_v\beta_3$, as suggested by the single-cell PCR data, is sufficient to allow trafficking of a lower number of $Ca_v\alpha_{1D}$ subunits to the membrane. A further reduction in the number of functional Ca^{2+} channels might be caused by a lower trafficking efficiency of $Ca_v\beta_1$ and $Ca_v\beta_3$ compared to the palmitoylated $Ca_v\beta_2$ subunit (Chien et al., 1998). The presence of functional $Ca_v\alpha_{1D}$ - $Ca_v\beta$ complexes could also explain the unchanged gating properties

found for $Ca_v\beta_2^{-/-}$ Ca^{2+} currents, since the voltage-dependence of activation is similar for $Ca_v\alpha_{1D}$ coexpressed with any of the 4 $Ca_v\beta$ subunits (Xu and Lipscombe, 2001), while overexpression of $Ca_v\alpha_1$ subunits alone generally leads to greatly reduced Ca^{2+} currents activating at much more positive potentials (Cantí et al., 2000; Jones et al., 1998; Neely et al., 1993). The role of $Ca_v\beta_2$ as primary $Ca_v\beta$ subunit in IHCs as well as the hypothesis of incomplete compensation by other $Ca_v\beta$ subunits are further supported by the finding that $Ca_v\beta_3^{-/-}$ mice show slightly reduced current amplitudes in IHCs but normal hearing (Kuhn et al., 2009). A presence of $Ca_v\beta_4$ in mouse IHCs cannot be fully excluded, since in the same publication, Kuhn et al. report a minor phenotype also for $Ca_v\beta_4$ mutants expressing a truncated protein missing the alpha binding pocket (Burgess et al., 1997). Still, these mice also show unimpaired hearing and, in agreement with our data, Kuhn et al. did not find $Ca_v\beta_4$ mRNA in IHCs. $Ca_v\beta_2^{-/-}$ mice still carry a gene for $Ca_v\beta_2$ from the transgenic rescue of the lethal effects of the $Ca_v\beta_2$ knockout (expression of $Ca_v\beta_2$ under the α -myosin heavy chain promoter, which is specific for cardiac tissue). However, we consider it unlikely that leaky expression of $Ca_v\beta_2$ in IHCs might be responsible for the residual current and unchanged gating behavior in $Ca_v\beta_2^{-/-}$ IHCs, since no $Ca_v\beta_2$ mRNA was detected in any of the $Ca_v\beta_2^{-/-}$ cells analyzed by single-cell RT-PCR (Fig. 6).

The IHC synapse depends entirely on L-type channels (Robertson and Paki, 2002; Brandt et al., 2003) and we consider compensation of the lack of $Ca_v\alpha_{1D}$ subunits by upregulation of other types of Ca^{2+} channels to be unlikely, since the enhancement of Ca^{2+} currents by BayK8644 was similar in wild-type and $Ca_v\beta_2^{-/-}$ IHCs (Fig. 7C, D), suggesting a similar repertoire of Ca^{2+} channels in both strains. The observed changes in CDI, a reduced fast component of inactivation and an increased slow component, might be explained by two different mechanisms. The lack of the fast component in $Ca_v\beta_2^{-/-}$ IHCs might be due to the reduction in amplitude of the presynaptic Ca^{2+} microdomain caused by the decrease in Ca^{2+} currents leading to a lower Ca^{2+} concentration detected by the channels. Indeed, we observed a

reduction in the fast component of CDI in wild-type IHCs when we reduced Ca^{2+} influx by lowering the extracellular Ca^{2+} concentration. The speed-up in the slow component of CDI seems consistent with the slower inactivation kinetics observed when expressing $\text{Ca}_V\alpha_1$ with $\text{Ca}_V\beta_2$ subunits (Cui et al., 2007), especially those of $\text{Ca}_V\beta_{2a}$ or $\text{Ca}_V\beta_{2e}$ (Takahashi et al., 2003).

We found that the amplitude of Ca^{2+} microdomains at $\text{Ca}_V\beta_2^{-/-}$ synapses was decreased. However, we did not find a significant increase in the number of ribbons that did not show a depolarization-induced Ca^{2+} microdomain, as was observed by labeling the ribbon with a fluorescent peptide. This argues for a general reduction in the number of Ca^{2+} channels across all synapses and against a selective lack of Ca^{2+} channels at particular synapses. Still, a difference in the fractions of the individual $\text{Ca}_V\beta$ subunits at individual synapses, which might be speculated to underlie the variance in Ca^{2+} microdomains within single IHCs observed by Frank et al., 2009, cannot be excluded. We found that the reduction in the fluorescence amplitude of individual hotspots was lower than the reduction of whole-cell currents; however, this might be explained by a tendency of the experimenter to discard those recordings with the weakest Ca^{2+} hotspots because of signal-to-noise considerations or as spots out of focus, thus creating a bias towards brighter hotspots.

If the decrease of Ca^{2+} channels in $\text{Ca}_V\beta_2^{-/-}$ mice is indeed uniform across the entire hair cell surface, we can try to estimate the number of Ca^{2+} channels at one $\text{Ca}_V\beta_2^{-/-}$ IHC synapse following the discussion in Brandt et al., 2005. We assume the fraction of extrasynaptic channels to be ~30%. This leads to ~350 synaptic channels in $\text{Ca}_V\beta_2^{-/-}$ or ~30 channels per synapse, as compared to ~80 in wild-type. Since the maximum open probability of single channels was attained in the presence of BayK8644, we can estimate the maximum open probability in non-augmented conditions from the increase in whole-cell current caused by BayK8644 (Fig. 7C, D) as ~0.35. From this, the maximum number of open Ca^{2+} channels per active zone upon strong depolarization of the IHC can be estimated as ~30 in wild-type and ~10 in $\text{Ca}_V\beta_2^{-/-}$. A Ca^{2+}

channel complement of this size would be expected to still be able to support reliable exocytosis at the synapse.

Synaptic transmission from $Ca_v\beta_2^{-/-}$ IHCs

Binding of $Ca_v\beta$ to the presynaptic protein RIM, as reported by (Kiyonaka et al., 2007) for $Ca_v\beta_{2a}$ and $Ca_v\beta_4$, presented an interesting candidate for the molecular link keeping the vesicles in close proximity to Ca^{2+} channels, thus enabling “nanodomain control” of exocytosis (Brandt et al., 2005; Moser et al., 2006a; Goutman and Glowatzki, 2007). However, our experiments showed no indication that the lack of $Ca_v\beta_2$ might shift the release properties to microdomain control. In the microdomain regime, the decrease in Ca^{2+} current caused by a decrease in the number of channels should result in an even stronger reduction in exocytosis (Augustine et al., 1991) due to the supralinear relationship between Ca^{2+} influx and release at the IHC synapse (Beutner et al., 2001). On the contrary, we observed reduction of both parameters by similar amounts in $Ca_v\beta_2^{-/-}$ IHCs (68% reduction of Ca^{2+} influx and 67% reduction of exocytosis). Localization of Ca^{2+} channels was still intact on the micrometer scale (as is evident from the unchanged spatial properties of Ca^{2+} microdomains) as well as on the nanometer scale (since the decrease in exocytosis caused by introduction of 5 mM EGTA to the intracellular solution was comparable in wild-type and $Ca_v\beta_2^{-/-}$ mice). Therefore, it appears that either other $Ca_v\beta$ subunits compensated for the lack of $Ca_v\beta_2$ or that $Ca_v\beta$ subunits are altogether dispensable for linking Ca^{2+} channels to the presynaptic machinery.

Auditory neuron activity in $Ca_v\beta_2^{-/-}$.

The reduced amount of exocytosis combined with the OHC dysfunction lead us to question whether residual encoding of auditory stimuli still occurs in $Ca_v\beta_2^{-/-}$ mice under *in vivo* conditions. We found greatly reduced spiking activity in auditory neurons, but encoding of auditory stimuli still occurred. Due

to the lack of active amplification in the cochlea, requiring higher sound levels for stimulation of knockout animals, and due to potential other influences of developmental impairment seen in the organ of Corti, it is difficult to relate the observed decrease in spike rate to the reduced exocytosis and number of Ca^{2+} channels in IHCs. Nevertheless, it appears that the remaining Ca^{2+} channels and exocytosis still allow residual sound encoding, even though at reduced sensitivity. Moreover, comparison of the kinetics of RRP exocytosis and postsynaptic spike rate adaptation suggests that RRP consumption causing rapid peripheral auditory adaptation (Furukawa and Matsuura, 1978; Moser and Beutner, 2000; Spassova et al., 2004; Goutman and Glowatzki, 2007). This offers further support for the impression that Ca^{2+} influx-exocytosis coupling was not disturbed for the remaining RRP in $\text{Ca}_v\beta_2^{-/-}$ animals.

Developmental defects in $\text{Ca}_v\beta_2^{-/-}$ IHCs.

The developmental defects reported here once more emphasize the requirement of intact Ca^{2+} signaling for normal development and maintenance of sensory cells (Ball et al., 2002; Brandt et al., 2003; Jalkanen et al., 2006; Nemzou N. et al., 2006; Wycisk et al., 2006). An additional influence on development might be regulation of gene expression by the $\text{Ca}_v\beta$ subunits themselves. $\text{Ca}_v\beta_{4c}$ has been shown to have a secondary role as a transcription regulator (Hibino et al., 2003). However, it is not known whether other $\text{Ca}_v\beta$ subunits fulfill a comparable role and we do not have any indication that a similar effect might be at work here.

Interestingly, the $\text{Ca}_v\beta_2^{-/-}$ IHCs show a phenotype intermediate between mature and immature wild-type IHCs (or $\text{Ca}_v\alpha_{1D}^{-/-}$ IHCs), with some features appearing mature, while some immature characteristics still remain (Fig. 19).

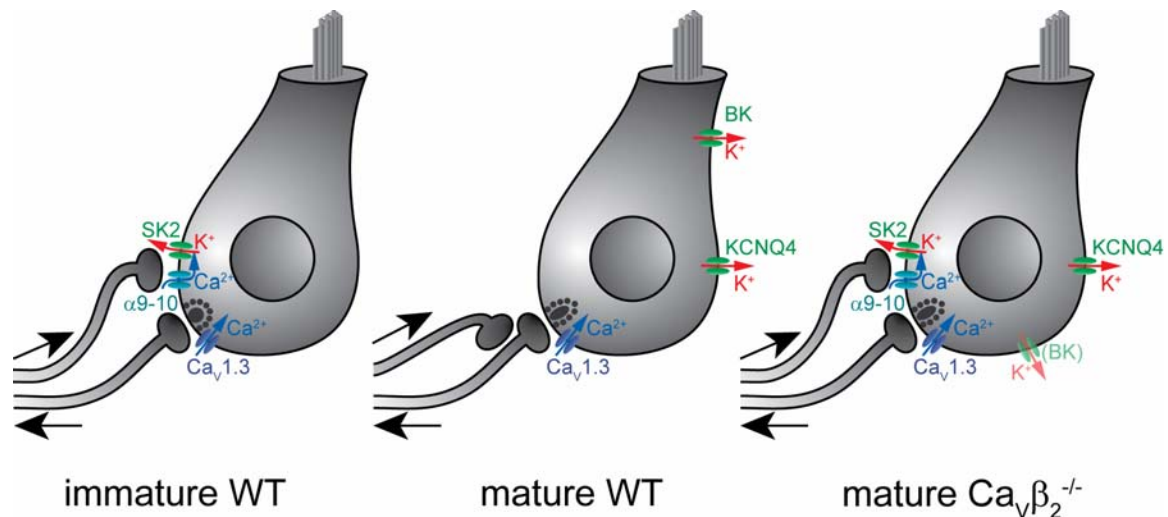


Figure 19: Developmental changes in wild-type and $Ca_v \beta_2^{-/-}$ IHCs. During development (between p7 and p14), IHCs cease expression of SK2 channels. Efferent synapses move away from the soma of the IHC to form axodendritic synapses with afferent neurons and IHCs start expressing BK and KCNQ4 channels. The shape of the synaptic ribbon changes from round to ellipsoid. $Ca_v \beta_2^{-/-}$ IHCs show some of the features of mature cells (expression of KCNQ4 channels, mature ribbon, normal number of synapses), but still retain other immature attributes (persistence of efferent innervation and associated expression of SK2 channels in some, but not all cells). BK channels are expressed but not at wild-type levels, and their localization to the hair cell's 'neck' is disrupted.

The most striking change in the K^+ channel complement of $Ca_v \beta_2^{-/-}$ IHCs is the impaired localization and altered gating of BK channels. Notably, the decreased slope of BK activation curves in $Ca_v \beta_2^{-/-}$ is similar to values observed in inside-out-patches of IHC membranes carrying BK channels, where Ca^{2+} concentrations are constant (18 mM; Oliver et al., 2003). While IHC BK channels are mostly independent of voltage-dependent Ca^{2+} influx (Marcotti et al., 2004; Thurm et al., 2005), a similar shift of activation towards more depolarized potentials can be observed at low Ca^{2+} concentrations on the intracellular side (Oliver et al., 2003) or when introducing high concentrations of Ca^{2+} buffers into the cell (Marcotti et al., 2004). In the latter case, however, no change in slope was observed, but the higher efficiency of

BAPTA (in comparison to EGTA) to suppress BK currents led the authors to the conclusion that the distance between BK channels and intracellular Ca^{2+} stores was less than 40 nm. Therefore, one might speculate that the mislocalization of BK channels in $\text{Ca}_v\beta_2^{-/-}$ IHCs might be at least partially responsible for the shift in activation potential.

CaBPs in mouse IHCs

As shown by the recordings of Ca^{2+} and Ba^{2+} currents, exocytosis and auditory brainstem activity in $\text{CaBP4}^{-/-}$ animals, CaBP4 has little to no effect on hearing and makes only a minor contribution to the unusually low CDI in mouse IHC. This finding agrees with the minor effects of CaBP4 coexpression with $\text{Ca}_v1.3$ channels on CDI in HEK cells (Cui et al., 2007). Yang et al., 2006 previously reported a much higher efficiency of CaBP4 in suppressing CDI of $\text{Ca}_v1.3$ channels in the same cells. However, this might be due to the use of an inducible expression system which can result in overexpression and consequential masking of functional differences between CaBPs which would otherwise be visible at non-saturating expression levels.

Immunostaining shows that CaBP4 is present in IHCs alongside CaBP1, 2 and 5 (Cui et al., 2007). The co-expression of CaBP1 and $\text{Ca}_v\alpha_{1D}$ in HEK cells results in currents that mimic the inactivation properties of IHC Ca^{2+} currents quite well. Furthermore, CaBP1 has been found to localize to the synapses of IHCs in older mice (aged 2 months; Cui et al., 2007). In conclusion, we believe that CaBP4 has little impact on Ca^{2+} channel regulation in IHCs. Instead, CaBP1 appears to be a likely candidate for mediating the strong inhibition of CDI found in IHCs.

Conclusions

Regulation of Ca^{2+} channels can be achieved in a variety of ways. Here, we examined two potential mechanisms, via the Ca^{2+} channel $\text{Ca}_v\beta$ subunit and the CaBPs. We managed to shed new light on the types of $\text{Ca}_v\beta$ subunits expressed in mouse IHCs, showing that $\text{Ca}_v\beta_2$ is important for Ca^{2+} channel

function, regulating inactivation of the channel. In IHCs, it also regulates the number of Ca^{2+} channels, probably by enhancing trafficking of $\text{Ca}_V\alpha_{1D}$ to the membrane, and thereby secretion and development. The developmental impairment in $\text{Ca}_V\beta_2^{-/-}$ IHCs was shown to include a defect in BK channel expression, where expression levels are lowered and clustering of the channels is abolished. We also have shown that CaBP4 has little or no role in IHCs, proposing that in fact CaBP1 is the major CaBP acting in IHCs.

References

Ahern C, Powers P, Biddlecome G, Roethe L, Vallejo P, Mortenson L, Strube C, Campbell K, Coronado R, Gregg R (2001) Modulation of L-type Ca²⁺ current but not activation of Ca²⁺ release by the gamma1 subunit of the dihydropyridine receptor of skeletal muscle. *BMC Physiology* 1:8

Arias JM, Murbartián J, Vitko I, Lee J, Perez-Reyes E (2005) Transfer of [beta] subunit regulation from high to low voltage-gated Ca²⁺ channels. *FEBS Letters* 579:3907-3912

Ashmore J (2008) Cochlear Outer Hair Cell Motility. *Physiol. Rev.* 88:173-210

Assad JA, Shepherd GMG, Corey DP (1991) Tip-link integrity and mechanical transduction in vertebrate hair cells. *Neuron* 7:985-994

Augustine GJ, Adler EM, Charltonc MP (1991) The Calcium Signal for Transmitter Secretion from Presynaptic Nerve Terminals. *Annals of the New York Academy of Sciences* 635:365-381

Ball SL, Powers PA, Shin H, Morgans CW, Peachey NS, Gregg RG (2002) Role of the {beta}2 Subunit of Voltage-Dependent Calcium Channels in the Retinal Outer Plexiform Layer. *Invest. Ophthalmol. Vis. Sci.* 43:1595-1603

Barclay J, Balaguero N, Mione M, Ackerman SL, Letts VA, Brodbeck J, Canti C, Meir A, Page KM, Kusumi K, Perez-Reyes E, Lander ES, Frankel WN, Gardiner RM, Dolphin AC, Rees M (2001) Ducky Mouse Phenotype of Epilepsy and Ataxia Is Associated with Mutations in the Cacna2d2 Gene and Decreased Calcium Channel Current in Cerebellar Purkinje Cells. *J. Neurosci.* 21:6095-6104

Beguín P, Nagashima K, Gonoï T, Shibasaki T, Takahashi K, Kashima Y, Ozaki N, Geering K, Iwanaga T, Seino S (2001) Regulation of Ca²⁺ channel expression at the cell surface by the small G-protein kir/Gem. *Nature* 411:701-706

Beurg M, Fettiplace R, Nam J, Ricci AJ (2009) Localization of inner hair cell mechanotransducer channels using high-speed calcium imaging. *Nat Neurosci* 12:553-558

Beutner D, Moser T (2001) The Presynaptic Function of Mouse Cochlear Inner Hair Cells during Development of Hearing. *J. Neurosci.* 21:4593-4599

Beutner D, Voets T, Neher E, Moser T (2001) Calcium Dependence of Exocytosis and Endocytosis at the Cochlear Inner Hair Cell Afferent Synapse. *Neuron* 29:681-690

- Bichet D, Cornet V, Geib S, Carlier E, Volsen S, Hoshi T, Mori Y, De Waard M (2000) The I-II Loop of the Ca²⁺ Channel α 1 Subunit Contains an Endoplasmic Reticulum Retention Signal Antagonized by the β Subunit. *Neuron* 25:177-190
- Black JL (2003) The voltage-gated calcium channel gamma subunits: a review of the literature. *J. Bioenerg. Biomembr* 35:649-660
- Borsotto M, Barhanin J, Fosset M, Lazdunski M (1985) The 1,4-dihydropyridine receptor associated with the skeletal muscle voltage-dependent Ca²⁺ channel. Purification and subunit composition. *J. Biol. Chem* 260:14255-14263
- Brandt A, Khimich D, Moser T (2005) Few CaV1.3 channels regulate the exocytosis of a synaptic vesicle at the hair cell ribbon synapse. *J. Neurosci* 25:11577-11585
- Brandt A, Striessnig J, Moser T (2003) CaV1.3 channels are essential for development and presynaptic activity of cochlear inner hair cells. *J. Neurosci* 23:10832-10840
- Brehm P, Eckert R (1978) Calcium entry leads to inactivation of calcium channel in Paramecium. *Science* 202:1203-1206
- Bunt AH (1971) Enzymatic digestion of synaptic ribbons in amphibian retinal photoreceptors. *Brain Res* 25:571-577
- Burgess DL, Jones JM, Meisler MH, Noebels JL (1997) Mutation of the Ca²⁺ Channel [beta] Subunit Gene Cchb4 Is Associated with Ataxia and Seizures in the Lethargic (lh) Mouse. *Cell* 88:385-392
- Cantí C, Bogdanov Y, Dolphin AC (2000) Interaction between G proteins and accessory β subunits in the regulation of α 1B calcium channels in *Xenopus* oocytes. *J Physiol.* 527:419-432
- Cantí C, Nieto-Rostro M, Foucault I, Hebllich F, Wratten J, Richards MW, Hendrich J, Douglas L, Page KM, Davies A, Dolphin AC (2005) The metal-ion-dependent adhesion site in the Von Willebrand factor-A domain of α 2 δ subunits is key to trafficking voltage-gated Ca²⁺ channels. *Proceedings of the National Academy of Sciences of the United States of America* 102:11230-11235
- Carbone E, Lux HD (1984) A low voltage-activated, fully inactivating Ca channel in vertebrate sensory neurones. *Nature* 310:501-502
- Catterall WA, Perez-Reyes E, Snutch TP, Striessnig J (2005) International Union of Pharmacology. XLVIII. Nomenclature and structure-function relationships of voltage-gated calcium channels. *Pharmacol. Rev* 57:411-425
- Cens T, Rousset M, Leyris J, Fesquet P, Charnet P (2006) Voltage- and

calcium-dependent inactivation in high voltage-gated Ca²⁺ channels. *Progress in Biophysics and Molecular Biology* 90:104-117

Chan DK, Hudspeth AJ (2005) Ca²⁺ current-driven nonlinear amplification by the mammalian cochlea in vitro. *Nat Neurosci* 8:149-155

Chien AJ, Gao T, Perez-Reyes E, Hosey MM (1998) Membrane Targeting of L-type Calcium Channels. *Journal of Biological Chemistry* 273:23590-23597

Corey DP, Hudspeth AJ (1979) Ionic basis of the receptor potential in a vertebrate hair cell. *Nature* 281:675-677

Cui G, Meyer AC, Calin-Jageman I, Neef J, Haeseleer F, Moser T, Lee A (2007) Ca²⁺-binding proteins tune Ca²⁺-feedback to Cav1.3 channels in mouse auditory hair cells. *J. Physiol. (Lond.)* 585:791-803

Dallos P, Popper AN, Fay RR (1996) *The cochlea*. Springer New York:

Dallos P, Fakler B (2002) Prestin, a new type of motor protein. *Nat Rev Mol Cell Biol* 3:104-111

DeMaria CD, Soong TW, Alseikhan BA, Alvania RS, Yue DT (2001) Calmodulin bifurcates the local Ca²⁺ signal that modulates P/Q-type Ca²⁺ channels. *Nature* 411:484-489

Dick O, Dieck ST, Altmann WD, Ammermüller J, Weiler R, Garner CC, Gundelfinger ED, Br JH, stätter (2003) The Presynaptic Active Zone Protein Bassoon Is Essential for Photoreceptor Ribbon Synapse Formation in the Retina. *Neuron* 37:775-786

Dick O, Hack I, Altmann WD, Garner CC, Gundelfinger ED, Brandstätter JH (2001) Localization of the presynaptic cytomatrix protein Piccolo at ribbon and conventional synapses in the rat retina: Comparison with Bassoon. *The Journal of Comparative Neurology* 439:224-234

Dou H, Vazquez AE, Namkung Y, Chu H, Cardell EL, Nie L, Parson S, Shin H, Yamoah EN (2004) Null Mutation of a 1D Ca²⁺ Channel Gene Results in Deafness but No Vestibular Defect in Mice. *JARO - Journal of the Association for Research in Otolaryngology* 5:215-226

Erickson MG, Alseikhan BA, Peterson BZ, Yue DT (2001) Preassociation of Calmodulin with Voltage-Gated Ca²⁺ Channels Revealed by FRET in Single Living Cells. *Neuron* 31:973-985

Ertel EA, Campbell KP, Harpold MM, Hofmann F, Mori Y, Perez-Reyes E, Schwartz A, Snutch TP, Tanabe T, Birnbaumer L, Tsien RW, Catterall WA (2000) Nomenclature of voltage-gated calcium channels. *Neuron* 25:533-535

Felix R, Gurnett CA, De Waard M, Campbell KP (1997) Dissection of Functional Domains of the Voltage-Dependent Ca²⁺ Channel alpha 2delta

Subunit. *J. Neurosci.* 17:6884-6891

Ferreira G, Yi J, Ríos E, Shirokov R (1997) Ion-dependent inactivation of barium current through L-type calcium channels. *J. Gen. Physiol* 109:449-461

Fettiplace R, Fuchs PA (1999) Mechanisms of hair cell tuning. *Annu. Rev. Physiol* 61:809-834

Fettiplace R, Hackney CM (2006) The sensory and motor roles of auditory hair cells. *Nat Rev Neurosci* 7:19-29

Flockerzi V, Oeken H, Hofmann F, Pelzer D, Cavalié A, Trautwein W (1986) Purified dihydropyridine-binding site from skeletal muscle t-tubules is a functional calcium channel. *Nature* 323:66-68

Frank T, Khimich D, Neef A, Moser T (2009) Mechanisms contributing to synaptic Ca²⁺ signals and their heterogeneity in hair cells. *Proceedings of the National Academy of Sciences* 106:4483-4488

Freise D, Held B, Wissenbach U, Pfeifer A, Trost C, Himmerkus N, Schweig U, Freichel M, Biel M, Hofmann F, Hoth M, Flockerzi V (2000) Absence of the γ Subunit of the Skeletal Muscle Dihydropyridine Receptor Increases L-type Ca²⁺ Currents and Alters Channel Inactivation Properties. *Journal of Biological Chemistry* 275:14476-14481

Fuchs PA, Glowatzki E, Moser T (2003) The afferent synapse of cochlear hair cells. *Current Opinion in Neurobiology* 13:452-458

Furukawa T, Matsuura S (1978) Adaptive rundown of excitatory post-synaptic potentials at synapses between hair cells and eight nerve fibres in the goldfish. *J. Physiol. (Lond.)* 276:193-209

Glauner KS, Mannuzzu LM, Gandhi CS, Isacoff EY (1999) Spectroscopic mapping of voltage sensor movement in the Shaker potassium channel. *Nature* 402:813-817

Glowatzki E, Fuchs PA (2000) Cholinergic Synaptic Inhibition of Inner Hair Cells in the Neonatal Mammalian Cochlea. *Science* 288:2366-2368

Glowatzki E, Fuchs PA (2002) Transmitter release at the hair cell ribbon synapse. *Nat Neurosci* 5:147-154

Gonzalez-Gutierrez G, Miranda-Laferte E, Neely A, Hidalgo P (2007) The Src Homology 3 Domain of the β -Subunit of Voltage-gated Calcium Channels Promotes Endocytosis via Dynamin Interaction. *Journal of Biological Chemistry* 282:2156-2162

Goutman JD, Glowatzki E (2007) Time course and calcium dependence of transmitter release at a single ribbon synapse. *Proceedings of the National Academy of Sciences* 104:16341-16346

Green GE, Khan KM, Beisel KW, Drescher MJ, Hatfield JS (1996) Calcium Channel Subunits in the Mouse Cochlea. *Journal of Neurochemistry* 67:37-45

Green PJ, Warre R, Hayes PD, McNaughton NCL, Medhurst AD, Pangalos M, Duckworth DM, Randall AD (2001) Kinetic modification of the alpha1I subunit-mediated T-type Ca²⁺ channel by a human neuronal Ca²⁺ channel gamma subunit. *J Physiology* 533:467-478

Haeseleer F, Imanishi Y, Maeda T, Possin DE, Maeda A, Lee A, Rieke F, Palczewski K (2004) Essential role of Ca²⁺-binding protein 4, a Cav1.4 channel regulator, in photoreceptor synaptic function. *Nat Neurosci* 7:1079-1087

Hafidi A, Beurg M, Dulon D (2005) Localization and developmental expression of BK channels in mammalian cochlear hair cells. *Neuroscience* 130:475-484

Hanlon MR, Berrow NS, Dolphin AC, Wallace BA (1999) Modelling of a voltage-dependent Ca²⁺ channel beta subunit as a basis for understanding its functional properties. *FEBS Lett* 445:366-370

Hansen JP, Chen R, Larsen JK, Chu P, Janes DM, Weis KE, Best PM (2004) Calcium channel gamma6 subunits are unique modulators of low voltage-activated (Cav3.1) calcium current. *J. Mol. Cell. Cardiol* 37:1147-1158

Hibino H, Pironkova R, Onwumere O, Rousset M, Charnet P, Hudspeth AJ, Lesage F (2003) Direct interaction with a nuclear protein and regulation of gene silencing by a variant of the Ca²⁺-channel β 4 subunit. *Proceedings of the National Academy of Sciences of the United States of America* 100:307-312

Hofmann F, Lacinova L, Klugbauer N (1999) Voltage-dependent calcium channels: from structure to function. *Reviews of physiology, biochemistry and pharmacology* 139:33-87

Howard J, Hudspeth AJ (1988) Compliance of the hair bundle associated with gating of mechano-electrical transduction channels in the Bullfrog's saccular hair cell. *Neuron* 1:189-199

Hudspeth A (2008) Making an Effort to Listen: Mechanical Amplification in the Ear. *Neuron* 59:530-545

Jackman SL, Choi S, Thoreson WB, Rabl K, Bartoletti TM, Kramer RH (2009) Role of the synaptic ribbon in transmitting the cone light response. *Nat Neurosci* 12:303-310

Jalkanen R, Mantjarvi M, Tobias R, Isosomppi J, Sankila E, Alitalo T, Bech-Hansen NT (2006) X linked cone-rod dystrophy, CORDX3, is caused by a mutation in the CACNA1F gene. *J Med Genet* 43:699-704

Jaramillo F, Hudspeth AJ (1991) Localization of the hair cell's transduction channels at the hair bundle's top by iontophoretic application of a channel blocker. *Neuron* 7:409-420

Jay SD, Ellis SB, McCue AF, Williams ME, Vedvick TS, Harpold MM, Campbell KP (1990) Primary structure of the gamma subunit of the DHP-sensitive calcium channel from skeletal muscle. *Science* 248:490-492

Jones LP, Wei S, Yue DT (1998) Mechanism of Auxiliary Subunit Modulation of Neuronal alpha 1E Calcium Channels. *J. Gen. Physiol.* 112:125-143

Kennedy HJ, Crawford AC, Fettiplace R (2005) Force generation by mammalian hair bundles supports a role in cochlear amplification. *Nature* 433:880-883

Kharkovets T, Dedek K, Maier H, Schweizer M, Khimich D, Nouvian R, Vardanyan V, Leuwer R, Moser T, Jentsch TJ (2006) Mice with altered KCNQ4 K⁺ channels implicate sensory outer hair cells in human progressive deafness. *EMBO J* 25:642-652

Khimich D, Nouvian R, Pujol R, Tom Dieck S, Egner A, Gundelfinger ED, Moser T (2005) Hair cell synaptic ribbons are essential for synchronous auditory signalling. *Nature* 434:889-894

Kiyonaka S, Wakamori M, Miki T, Urie Y, Nonaka M, Bito H, Beedle AM, Mori E, Hara Y, De Waard M, Kanagawa M, Itakura M, Takahashi M, Campbell KP, Mori Y (2007) RIM1 confers sustained activity and neurotransmitter vesicle anchoring to presynaptic Ca²⁺ channels. *Nat Neurosci* 10:691-701

Knirsch M (2007) Ca²⁺-Kanäle in cochleären Haarsinneszellen von Maus und Ratte: Entwicklungsgang der Ca²⁺-Ströme und molekulare Zusammensetzung.

Koschak A, Reimer D, Huber I, Grabner M, Glossmann H, Engel J, Striessnig J (2001) α 1D (Cav1.3) Subunits Can Form L-type Ca²⁺ Channels Activating at Negative Voltages. *Journal of Biological Chemistry* 276:22100-22106

Kros CJ, Crawford AC (1990) Potassium currents in inner hair cells isolated from the guinea-pig cochlea. *J. Physiol. (Lond.)* 421:263-291

Kuhn S, Knirsch M, Rüttiger L, Kasperek S, Winter H, Freichel M, Flockerzi V, Knipper M, Engel J (2009) Ba²⁺ currents in inner and outer hair cells of mice lacking the voltage-dependent Ca²⁺ channel subunits beta3 or beta4. *Channels (Austin)* 3:366-376

Lambert RC, Maulet Y, Mouton J, Beattie R, Volsen S, De Waard M, Feltz A (1997) T-Type Ca²⁺ Current Properties Are Not Modified by Ca²⁺ Channel beta Subunit Depletion in Nodosus Ganglion Neurons. *J. Neurosci.* 17:6621-6628

- Lee A, Scheuer T, Catterall WA (2000) Ca²⁺/Calmodulin-Dependent Facilitation and Inactivation of P/Q-Type Ca²⁺ Channels. *J. Neurosci.* 20:6830-6838
- Lee A, Westenbroek RE, Haeseleer F, Palczewski K, Scheuer T, Catterall WA (2002) Differential modulation of Cav2.1 channels by calmodulin and Ca²⁺-binding protein 1. *Nat Neurosci* 5:210-217
- Lenzi D, Gersdorff HV (2001) Structure suggests function: the case for synaptic ribbons as exocytotic nanomachines. *BioEssays* 23:831-840
- Leuranguer V, Bourinet E, Lory P, Nargeot J (1998) Antisense depletion of beta-subunits fails to affect T-type calcium channels properties in a neuroblastoma cell line. *Neuropharmacology* 37:701-708
- Liang H, DeMaria CD, Erickson MG, Mori MX, Alseikhan BA, Yue DT (2003) Unified Mechanisms of Ca²⁺ Regulation across the Ca²⁺ Channel Family. *Neuron* 39:951-960
- Liberman MC, Gao J, He DZZ, Wu X, Jia S, Zuo J (2002) Prestin is required for electromotility of the outer hair cell and for the cochlear amplifier. *Nature* 419:300-304
- Lindau M, Neher E (1988) Patch-clamp techniques for time-resolved capacitance measurements in single cells. *Pflugers Arch* 411:137-146
- Liu H, De Waard M, Scott VES, Gurnett CA, Lennon VA, Campbell KP (1996) Identification of Three Subunits of the High Affinity ω -Conotoxin MVIIC-sensitive Ca²⁺ Channel. *Journal of Biological Chemistry* 271:13804-13810
- Llinás R, Sugimori M, Lin JW, Cherksey B (1989) Blocking and isolation of a calcium channel from neurons in mammals and cephalopods utilizing a toxin fraction (FTX) from funnel-web spider poison. *Proc. Natl. Acad. Sci. U.S.A* 86:1689-1693
- Logothetis DE, Movahedi S, Satler C, Lindpaintner K, Nadal-Ginard B (1992) Incremental reductions of positive charge within the S4 region of a voltage-gated K⁺ channel result in corresponding decreases in gating charge. *Neuron* 8:531-540
- Lohi H, Kujala M, Kerkelä E, Saarialho-Kere U, Kestilä M, Kere J (2000) Mapping of Five New Putative Anion Transporter Genes in Human and Characterization of SLC26A6, A Candidate Gene for Pancreatic Anion Exchanger. *Genomics* 70:102-112
- Lumpkin EA, Hudspeth AJ (1995) Detection of Ca²⁺ entry through mechanosensitive channels localizes the site of mechanoelectrical transduction in hair cells. *Proc. Natl. Acad. Sci. U.S.A* 92:10297-10301

- Marcotti W, Johnson SL, Holley MC, Kros CJ (2003) Developmental changes in the expression of potassium currents of embryonic, neonatal and mature mouse inner hair cells. *The Journal of Physiology* 548:383-400
- Marcotti W, Johnson SL, Kros CJ (2004) Effects of intracellular stores and extracellular Ca²⁺ on Ca²⁺-activated K⁺ currents in mature mouse inner hair cells. *The Journal of Physiology* 557:613-633
- Meir A, Dolphin A (2002) Kinetics and Gβγ modulation of Cav2.2 channels with different auxiliary β subunits. *Pflügers Archiv European Journal of Physiology* 444:263-275
- Mikaelian D, Ruben RJ (1965) Development of Hearing in the Normal Cba-J Mouse: Correlation of Physiological Observations with Behavioral Responses and with Cochlear Anatomy. *SOTO* 59:451-461
- Moser T, Beutner D (2000) Kinetics of exocytosis and endocytosis at the cochlear inner hair cell afferent synapse of the mouse. *Proceedings of the National Academy of Sciences of the United States of America* 97:883-888
- Moser T, Brandt A, Lysakowski A (2006a) Hair cell ribbon synapses. *Cell and Tissue Research* 326:347-359
- Moser T, Neef A, Khimich D (2006b) Mechanisms underlying the temporal precision of sound coding at the inner hair cell ribbon synapse. *The Journal of Physiology* 576:55-62
- Müller U (2008) Cadherins and mechanotransduction by hair cells. *Curr. Opin. Cell Biol* 20:557-566
- Neely A, Wei X, Olcese R, Birnbaumer L, Stefani E (1993) Potentiation by the beta subunit of the ratio of the ionic current to the charge movement in the cardiac calcium channel. *Science* 262:575-578
- Nemzou N. R, Bulankina A, Khimich D, Giese A, Moser T (2006) Synaptic organization in cochlear inner hair cells deficient for the CaV1.3 ([α]1D) subunit of L-type Ca²⁺ channels. *Neuroscience* 141:1849-1860
- Niidome T, Kim M, Friedrich T, Mori Y (1992) Molecular cloning and characterization of a novel calcium channel from rabbit brain. *FEBS Letters* 308:7-13
- Nilius B, Hess P, Lansman JB, Tsien RW (1985) A novel type of cardiac calcium channel in ventricular cells. *Nature* 316:443-446
- Nouvian R, Beutner D, Parsons T, Moser T (2006) Structure and Function of the Hair Cell Ribbon Synapse. *Journal of Membrane Biology* 209:153-165
- Nowycky MC, Fox AP, Tsien RW (1985) Three types of neuronal calcium channel with different calcium agonist sensitivity. *Nature* 316:440-443

- Oliver D, He DZZ, Klocker N, Ludwig J, Schulte U, Waldegger S, Ruppertsberg JP, Dallos P, Fakler B (2001) Intracellular Anions as the Voltage Sensor of Prestin, the Outer Hair Cell Motor Protein. *Science* 292:2340-2343
- Oliver D, Klöcker N, Schuck J, Baukowitz T, Ruppertsberg JP, Fakler B (2000) Gating of Ca²⁺-Activated K⁺ Channels Controls Fast Inhibitory Synaptic Transmission at Auditory Outer Hair Cells. *Neuron* 26:595-601
- Oliver D, Knipper M, Derst C, Fakler B (2003) Resting Potential and Submembrane Calcium Concentration of Inner Hair Cells in the Isolated Mouse Cochlea Are Set by KCNQ-Type Potassium Channels. *J. Neurosci.* 23:2141-2149
- Oliver D, Taberner AM, Thurm H, Sausbier M, Arntz C, Ruth P, Fakler B, Liberman MC (2006) The Role of BKCa Channels in Electrical Signal Encoding in the Mammalian Auditory Periphery. *J. Neurosci.* 26:6181-6189
- Osten P, Stern-Bach Y (2006) Learning from stargazin: the mouse, the phenotype and the unexpected. *Curr. Opin. Neurobiol* 16:275-280
- Parsons T, Sterling P (2003) Synaptic Ribbon: : Conveyor Belt or Safety Belt? *Neuron* 37:379-382
- Peterson BZ, DeMaria CD, Yue DT (1999) Calmodulin Is the Ca²⁺ Sensor for Ca²⁺-Dependent Inactivation of L-Type Calcium Channels. *Neuron* 22:549-558
- Pickles J, Comis S, Osborne M (1984) Cross-links between stereocilia in the guinea pig organ of Corti, and their possible relation to sensory transduction. *Hearing Research* 15:103-112
- Pitt GS, Zühlke RD, Hudmon A, Schulman H, Reuter H, Tsien RW (2001) Molecular Basis of Calmodulin Tethering and Ca²⁺-dependent Inactivation of L-type Ca²⁺ Channels. *Journal of Biological Chemistry* 276:30794-30802
- Platzer J, Engel J, Schrott-Fischer A, Stephan K, Bova S, Chen H, Zheng H, Striessnig J (2000) Congenital Deafness and Sinoatrial Node Dysfunction in Mice Lacking Class D L-Type Ca²⁺ Channels. *Cell* 102:89-97
- Plazas PV, Katz E, Gomez-Casati ME, Bouzat C, Elgoyhen AB (2005) Stoichiometry of the $\alpha 9\alpha 10$ Nicotinic Cholinergic Receptor. *J. Neurosci.* 25:10905-10912
- Pragnell M, De Waard M, Mori Y, Tanabe T, Snutch TP, Campbell KP (1994) Calcium channel β -subunit binds to a conserved motif in the I-II cytoplasmic linker of the $\alpha 1$ -subunit. *Nature* 368:67-70
- Purves D, Augustine GJ, Fitzpatrick D, Hall WC, LaMantia AS, McNamara JO,

- Williams SM (2004) Neuroscience Third Edition. Sinauer Associates, Inc.
- Pyott SJ, Glowatzki E, Trimmer JS, Aldrich RW (2004) Extrasynaptic Localization of Inactivating Calcium-Activated Potassium Channels in Mouse Inner Hair Cells. *J. Neurosci.* 24:9469-9474
- Qin N, Olcese R, Bransby M, Lin T, Birnbaumer L (1999) Ca²⁺-induced inhibition of the cardiac Ca²⁺ channel depends on calmodulin. *Proceedings of the National Academy of Sciences of the United States of America* 96:2435-2438
- Raphael Y, Altschuler RA (2003) Structure and innervation of the cochlea. *Brain Res. Bull* 60:397-422
- Ravindran A, Lao QZ, Harry JB, Abrahami P, Kobrinsky E, Soldatov NM (2008) Calmodulin-dependent gating of Ca(v)1.2 calcium channels in the absence of Ca(v)beta subunits. *Proc. Natl. Acad. Sci. U.S.A* 105:8154-8159
- Roberts WM, Jacobs RA, Hudspeth AJ (1990) Colocalization of ion channels involved in frequency selectivity and synaptic transmission at presynaptic active zones of hair cells. *J. Neurosci* 10:3664-3684
- Robertson D, Paki B (2002) Role of L-Type Ca²⁺ Channels in Transmitter Release From Mammalian Inner Hair Cells. II. Single-Neuron Activity. *J Neurophysiol* 87:2734-2740
- Roux I, Safieddine S, Nouvian R, Grati M, Simmler M, Bahloul A, Perfettini I, Gall ML, Rostaing P, Hamard G, Triller A, Avan P, Moser T, Petit C (2006) Otoferlin, Defective in a Human Deafness Form, Is Essential for Exocytosis at the Auditory Ribbon Synapse. *Cell* 127:277-289
- Rüttiger L, Sausbier M, Zimmermann U, Winter H, Braig C, Engel J, Knirsch M, Arntz C, Langer P, Hirt B, Müller M, Köpschall I, Pfister M, Münkner S, Rohbock K, Pfaff I, Rüscher A, Ruth P, Knipper M (2004) Deletion of the Ca²⁺-activated potassium (BK) α -subunit but not the BK β 1-subunit leads to progressive hearing loss. *Proceedings of the National Academy of Sciences of the United States of America* 101:12922-12927
- Ryan A, Dallos P (1975) Effect of absence of cochlear outer hair cells on behavioural auditory threshold. *Nature* 253:44-46
- Sakmann B, Neher E (2009) Single-channel recording. Springer Verlag.
- Schmitz F, Königstorfer A, Südhof TC (2000) RIBEYE, a Component of Synaptic Ribbons : : A Protein's Journey through Evolution Provides Insight into Synaptic Ribbon Function. *Neuron* 28:857-872
- Sharp AH, Campbell KP (1989) Characterization of the 1,4-dihydropyridine receptor using subunit-specific polyclonal antibodies. Evidence for a 32,000-Da subunit. *J. Biol. Chem* 264:2816-2825

- Shen Y, Yu D, Hiel H, Liao P, Yue DT, Fuchs PA, Soong TW (2006) Alternative Splicing of the CaV1.3 Channel IQ Domain, a Molecular Switch for Ca²⁺-Dependent Inactivation within Auditory Hair Cells. *J. Neurosci.* 26:10690-10699
- Siemens J, Lillo C, Dumont RA, Reynolds A, Williams DS, Gillespie PG, Müller U (2004) Cadherin 23 is a component of the tip link in hair-cell stereocilia. *Nature* 428:950-955
- Simmons D, Mansdorf N, Kim J (1996) Olivocochlear innervation of inner and outer hair cells during postnatal maturation: Evidence for a waiting period. *The Journal of Comparative Neurology* 370:551-562
- Simmons DD (2002) Development of the inner ear efferent system across vertebrate species. *Journal of Neurobiology* 53:228-250
- Sollner C, Rauch G, Siemens J, Geisler R, Schuster SC, Tübingen 2000 Screen Consortium T, Müller U, Nicolson T (2004) Mutations in cadherin 23 affect tip links in zebrafish sensory hair cells. *Nature* 428:955-959
- Spassova MA, Avissar M, Furman AC, Crumling MA, Saunders JC, Parsons TD (2004) Evidence that rapid vesicle replenishment of the synaptic ribbon mediates recovery from short-term adaptation at the hair cell afferent synapse. *J. Assoc. Res. Otolaryngol* 5:376-390
- Sterling P, Matthews G (2005) Structure and function of ribbon synapses. *Trends in Neurosciences* 28:20-29
- Strenzke N, Chanda S, Kopp-Scheinpflug C, Khimich D, Reim K, Bulankina AV, Neef A, Wolf F, Brose N, Xu-Friedman MA, Moser T (2009) Complexin-I Is Required for High-Fidelity Transmission at the Endbulb of Held Auditory Synapse. *J. Neurosci.* 29:7991-8004
- Taberner AM, Liberman MC (2005) Response Properties of Single Auditory Nerve Fibers in the Mouse. *J Neurophysiol* 93:557-569
- Takahashi M, Seagar MJ, Jones JF, Reber BF, Catterall WA (1987) Subunit structure of dihydropyridine-sensitive calcium channels from skeletal muscle. *Proceedings of the National Academy of Sciences* 84:5478-5482
- Takahashi SX, Mittman S, Colecraft HM (2003) Distinctive Modulatory Effects of Five Human Auxiliary [beta]2 Subunit Splice Variants on L-Type Calcium Channel Gating. *Biophysical Journal* 84:3007-3021
- Tanabe T, Takeshima H, Mikami A, Flockerzi V, Takahashi H, Kangawa K, Kojima M, Matsuo H, Hirose T, Numa S (1987) Primary structure of the receptor for calcium channel blockers from skeletal muscle. *Nature* 328:313-318

- Thurm H, Fakler B, Oliver D (2005) Ca²⁺-independent activation of BKCa channels at negative potentials in mammalian inner hair cells. *The Journal of Physiology* 569:137-151
- Tritsch NX, Yi E, Gale JE, Glowatzki E, Bergles DE (2007) The origin of spontaneous activity in the developing auditory system. *Nature* 450:50-55
- Tsien RW, Lipscombe D, Madison D, Bley K, Fox A (1995) Reflections on Ca(2+)-channel diversity, 1988-1994. *Trends Neurosci* 18:52-54
- Van Petegem F, Clark KA, Chatelain FC, Minor DL (2004) Structure of a complex between a voltage-gated calcium channel [beta]-subunit and an [alpha]-subunit domain. *Nature* 429:671-675
- Van Petegem F, Duderstadt KE, Clark KA, Wang M, Minor Jr. DL (2008) Alanine-Scanning Mutagenesis Defines a Conserved Energetic Hotspot in the CaV α 1 AID-CaV β Interaction Site that Is Critical for Channel Modulation. *Structure* 16:280-294
- Wang Y, Okamoto M, Schmitz F, Hofmann K, Sudhof TC (1997) Rim is a putative Rab3 effector in regulating synaptic-vesicle fusion. *Nature* 388:593-598
- Williams ME, Marubio LM, Deal CR, Hans M, Brust PF, Philipson LH, Miller RJ, Johnson EC, Harpold MM, Ellis SB (1994) Structure and functional characterization of neuronal alpha 1E calcium channel subtypes. *J. Biol. Chem* 269:22347-22357
- Witcher DR, De Waard M, Sakamoto J, Franzini-Armstrong C, Pragnell M, Kahl SD, Campbell KP (1993) Subunit identification and reconstitution of the N-type Ca²⁺ channel complex purified from brain. *Science* 261:486-489
- Wyatt CN, Page KM, Berrow NS, Brice NL, Dolphin AC (1998) The effect of overexpression of auxiliary Ca²⁺ channel subunits on native Ca²⁺ channel currents in undifferentiated mammalian NG108-15 cells. *J. Physiol. (Lond.)* 510 (Pt 2):347-360
- Wycisk KA, Zeitz C, Feil S, Wittmer M, Forster U, Neidhardt J, Wissinger B, Zrenner E, Wilke R, Kohl S, Berger W (2006) Mutation in the Auxiliary Calcium-Channel Subunit CACNA2D4 Causes Autosomal Recessive Cone Dystrophy. *The American Journal of Human Genetics* 79:973-977
- Xu W, Lipscombe D (2001) Neuronal CaV1.3{alpha}1 L-Type Channels Activate at Relatively Hyperpolarized Membrane Potentials and Are Incompletely Inhibited by Dihydropyridines. *J. Neurosci.* 21:5944-5951
- Yang PS, Alseikhan BA, Hiel H, Grant L, Mori MX, Yang W, Fuchs PA, Yue DT (2006) Switching of Ca²⁺-Dependent Inactivation of CaV1.3 Channels by Calcium Binding Proteins of Auditory Hair Cells. *J. Neurosci.* 26:10677-10689

- Zanazzi G, Matthews G (2009) The Molecular Architecture of Ribbon Presynaptic Terminals. *Molecular Neurobiology* 39:130-148
- Zenisek D, Davila V, Wan L, Almers W (2003) Imaging Calcium Entry Sites and Ribbon Structures in Two Presynaptic Cells. *J. Neurosci.* 23:2538-2548
- Zenisek D, Horst NK, Merrifield C, Sterling P, Matthews G (2004) Visualizing Synaptic Ribbons in the Living Cell. *J. Neurosci.* 24:9752-9759
- Zheng J, Shen W, He DZZ, Long KB, Madison LD, Dallos P (2000) Prestin is the motor protein of cochlear outer hair cells. *Nature* 405:149-155
- Zhou H, Kim S, Kirk EA, Tippens AL, Sun H, Haeseleer F, Lee A (2004) Ca²⁺-Binding Protein-1 Facilitates and Forms a Postsynaptic Complex with Cav1.2 (L-Type) Ca²⁺ Channels. *J. Neurosci.* 24:4698-4708
- Zühlke RD, Pitt GS, Deisseroth K, Tsien RW, Reuter H (1999) Calmodulin supports both inactivation and facilitation of L-type calcium channels. *Nature* 399:159-162

Abbreviations

ABR	Auditory brainstem recording
AID	α -interaction domain
BK channel	Large conductance voltage and Ca^{2+} activated K^+ channels
CaBP	Ca^{2+} binding protein
CDI	Ca^{2+} dependent inactivation
CF	Characteristic frequency
C_m	Membrane capacitance
ΔC_m	Membrane capacitance increment
DPOAE	Distortion-product otoacoustic emission
FWHM	Full width at half maximum
GSDB	Goat serum diluted buffer
HEPES-HBSS	HEPES-buffered Hanks' balanced salts solution
HVA	High-voltage activated
I_{Ba}	Ba^{2+} current
I_{Ca}	Ca^{2+} current
IV	Current-voltage relationship
IHC	Inner hair cell
LVA	low-voltage activated
MET	Mechano-electrical transducer
OHC	Outer hair cell
PBS	Phosphate-buffered saline
PSTH	Poststimulus time histogram
RMS	Root mean square
RRP	Readily releasable pool
R_s	Series resistance
RT-PCR	Reverse transcription polymerase chain reaction
SGN	Spiral ganglion neuron
SK2	Small conductance Ca^{2+} activated potassium channels
SPL	Sound pressure level
TEA-Cl	Tetraethylammonium chloride

Abbreviations

VDI	Voltage-dependant inactivation
VGCC	Voltage-gated Ca ²⁺ channel
WT	Wild-type

Acknowledgements

I am deeply indebted to the following people, without whom I would not have been able to complete this work. I would like to thank:

Tobias Moser for giving me the chance to work on this thesis in his lab and for continuous support and help.

Holger Taschenberger and Fred Wolf as members of the thesis committee for help and advice.

Anna Bulankina for performing the PCR experiments.

Anna Gehrt for performing and analyzing the single unit recordings.

Nicola Strenzke for setting up the single unit recordings, coanalyzing the single unit data, and preparing the sample from Fig. 5G.

Dietmar Riedel for acquiring the electron micrographs.

Alexander Meyer for acquiring a large part of the *CaBP4^{-/-}* capacitance data.

Christian Rüdiger for recording of ABRs and DPOAEs.

Andreas Neef for introducing me into the lab's standard techniques and for constant advice and help with any kind of question.

Tina Pangršič for even more help, being fun to work with and unknown amounts of chocolate.

Régis Nouvian for still more help, expert DJing and being the first to succumb to "setup II syndrome".

Thomas Frank for yet more help, DJing and building setup III.

Mark Rutherford for help and advice on the writing of the thesis.

Margitta Köppler for expert technical assistance and being the „lab mum“.

Sonja Blume, Nina-Kathrin Dankenbrink-Werder and Gudrun Heim for expert technical assistance.

The entire InnerEarLab for providing a great place to work and being friendly and helpful in science as well as life.

Gary Matthews for providing us with the fluorescently labeled CtBP2/RIBEYE binding peptide.

Acknowledgements

Ronald G. Gregg for providing us with the $Ca_v\beta_2^{-/-}$ mice.

M. McCall and P. Smith for the initial observation that $Ca_v\beta_2^{-/-}$ mice were deaf.

Francoise Haeseleer for providing us with the $CaBP4^{-/-}$ mouse.

Guiying Cui and Amy Lee for their collaboration in the CaBP4 project.

And most importantly my family and most of all my wife Ute for constant support, understanding and help.

Curriculum Vitae

Personal data

Jakob Neef

Zur Scharfmühle 4
37083 Göttingen
Tel.: 0551-2710603
Mobile: 0176-24535431
e-mail: jneef@gmx.de

Born 12.04.1979 in Göttingen
Family status: married, 2 children



Pre-university

- | | |
|-----------|--|
| 1991-1998 | <u>Secondary school</u> , completed with „ <u>Abitur</u> “, grade 1.9 – “ <u>Leistungskurse</u> ” (intensified courses) in physics and English |
| 1998-1999 | <u>Civilian service</u> at the Selbsthilfe Körperbehinderter, Göttingen |

University

- | | |
|-----------|---|
| 1999-2000 | <u>Studies of physics</u> at the university of Göttingen |
| 2000-2006 | <u>Studies of biology</u> at the university of Würzburg, including |
| 2003 | <u>Vordiplom</u> |
| 2003-2004 | <u>Student assistant</u> in the Virtual Brain Project at the Department of Genetics |
| 2005 | <u>Oral examinations for the Diploma</u> in the major subject <u>neurobiology (grade: 1.3)</u> and the minor subjects <u>bioinformatics (grade: 1.0)</u> and <u>genetics (grade: 1.7)</u> |
| 2005-2006 | <u>Diploma thesis</u> at the Department of Behavioral Physiology and Sociobiology in the group of Prof. Dr. Wolfgang Rössler |
| 2006-2010 | <u>PhD thesis</u> in the lab of Prof. Dr. T. Moser, Dept. Of Otolaryngology, University Clinics Göttingen |

Diploma thesis

„A Calcium Imaging Study of the Representation of Odour Identity and Intensity in the Antennal Lobe of *Camponotus floridanus*“

at the Department of Behavioral Physiology and Sociobiology in the group of Prof.
Dr. Wolfgang Rössler
Supervisor: Dr. Christoph Kleineidam

Publications

Cui G, Meyer AC, Calin-Jageman I, Neef J, Haeseleer F, Moser T, Lee A (2007) Ca²⁺-binding proteins tune Ca²⁺-feedback to Cav1.3 channels in mouse auditory hair cells. J. Physiol. (Lond.) 585:791-803

Zube C, Kleineidam CJ, Kirschner S, Neef J, Rössler W (2008) Organization of the olfactory pathway and odor processing in the antennal lobe of the ant *Camponotus floridanus*. Journal of Comparative Neurology 506:425

Neef J, Gehrt A, Bulankina AV, Meyer AC, Riedel D, Gregg RG, Strenzke N, Moser T (2009) The Ca²⁺ channel subunit beta2 regulates Ca²⁺ channel abundance and function in inner hair cells and is required for hearing. J. Neurosci 29:10730-10740